Effects of temperature on remotely sense
AC .H3 no.R84 15490
Roush, Ted L.
SOEST Library

EFFECTS OF TEMPERATURE ON REMOTELY SENSED MAFIC MINERAL ABSORPTION FEATURES

A THESIS SUBMITTED TO THE GRADUATE DIVISION OF THE UNIVERSITY OF HAWAII IN PARTIAL FULFILLMENT OF THE REQUIREMENTS FOR THE DEGREE OF

MASTER OF SCIENCE IN

GEOLOGY AND GEOPHYSICS

MAY 1984

By

Ted L. Roush

Thesis Committee:
Robert B. Singer, Chairman
Roger N. Clark
Michael J. Gaffey
Shiv K. Sharma

RETURN TO
HAWAII INSTITUTE OF GEOPHYSICS
LIBRARY ROOM

We certify that we have read this thesis and that in our opinion it is satisfactory in scope and quality as a thesis for the degree of Master of Science in Geology and Geophysics.

Thesis Committee

Robert B Anger

Chairman

S K Sharma

Michael Ray

Roger N. Clark

ACKNOWLEDGMENTS

I would like to thank Dr. Robert B. Singer for helping me become interested in this thesis topic and for his continuing encouragement throughout my research efforts. To Drs. Roger N. Clark and Michael J. Gaffey, who helped me learn the theory of reflectance spectroscopy, my heartfelt thanks. My thanks to Dr. Shiv K. Sharma who provided a basis for my understanding of vibrational spectroscopy and a calibration for determining my ability to communicate concepts to people outside my area of expertise.

It has been my pleasure and advantage to work with Dr. R. Hamilton Brown who not only designed and built the environment chamber used in this study but showed his patience and willingness to help with the thermal modelling.

The faculty, administration, and engineering staff of the Planetary Geosciences Division provide a fertile environment in which to work and it is my fellow graduate students who provide a necessary nutrient for a budding concept to come to blossom. My deepest thanks to all.

To my parents I give my deepest appreciation for their concern and encouragement throughout my academic career.

To Dr. Gerald Miller, who instilled a quest for knowledge, Thanks, I miss you.

ABSTRACT

Presented are the results of a laboratory study concerning the effects of temperature on characteristic mafic mineral reflectance spectra. This study presents the first reflectance spectra obtained at sample temperatures well below room temperature and at elevated temperatures with thermal contamination removed. Thus for the first time, characteristic absorption band intensities, widths, and positions are presented as a systematic function of sample temperature. The 1μm absorption band minimum remains unchanged over the temperature range of this study for all samples. However, the spectra of the pyroxenes show that the 2μm absorption band is temperature dependent. The orthopyroxene 2μm band minimum shifts to longer wavelengths, lower energies, while the clinopyroxene 2μm band minimum shifts to shorter wavelengths, higher energies, as temperature increases. The spectra of a basaltic-like assemblage show two distinct absorptions located near 2μm, due to the presence of both ortho- and clinopyroxene in the sample, at low temperatures and one asymmetric band near and above room temperature.

A Gaussian analysis is applied to the 1μm absorption feature in three common rock-forming minerals, orthopyroxene, clinopyroxene, and olivine, in an attempt to characterize the spectral features as a function of temperature. The results of this analysis show consistent trends of all Gaussian parameters (band centers, widths and intensities) as a function of temperature. The trends of these parameters are discussed in terms of potential physical mechanisms which can result in distinct absorptions within the wavelength region studied. In most cases there is no direct relationship between the Gaussian trends and any specific physical mechanism.

Orbital and physical parameters cited in the literature are used to theoretically model asteroid-like surfaces. Individual laboratory spectra are used to calculate a resultant spectrum for a given temperature distribution. The resulting calculated spectra show that there is little spectral difference between aphelion and perihelion spectral signatures for low eccentricity, main-belt, asteroid-like bodies. However, for higher eccentricity, earth-crossers spectral variations due to orbital position can affect resultant interpretations of pyroxene composition.

TABLE OF CONTENTS

LIST OF TABLES

LIST OF FIGURES

CHAPTER I: INTRODUCTION AND BACKGROUND

INTRODUCTION

Spectral reflectance measurements obtained from spacecraft and earth-based telescopic observations will remain the dominant means of collecting mineralogical information concerning surfaces of objects throughout the solar system for many years to come. Our ability to interpret this data, in terms of the identity and abundance of minerals present on a surface, is important for addressing more general questions concerning the origin and evolution of the solar system. A wide range of carefully planned laboratory studies conducted in recent years has resulted in our increased understanding of the interaction of light with a particulate surface to the point of investigating the importance of second order effects.

It is important to consider that planetary surface temperature varies from the frigid regions of the outer solar system to the inferno of Mercury's surface, and yet, only a limited number of studies have addressed the effect temperature variation would have on characteristic spectral signatures and consequently mineralogical and petrological interpretations. Presented here is a laboratory experiment designed to directly address temperature effects on reflectace spectra of mafic minerals over a range relevant for many parts of the solar system (≈80K to ≈450K) and as such should be a significant addition to current interpretative capabilities.

An environment chamber was used which allowed spectral reflectance data to be obtained while both samples and standard were at the same temperature and under vacuum. As a result, this paper will present the first reflectance spectra of mafic minerals obtained well below room temperature and at elevated temperatures with thermal emission eliminated. A Gaussian analysis is applied to Fe^{2+} absorption features in

an attempt to characterize their variation as a function of temperature. The results of this analysis are related to potential physical processes which can result in absorption within the wavelength region studied. The trends observed for these measurements are discussed in relation to remote sensing of planetary bodies whose surfaces are not at ambient temperature, and an example is presented relating the results of the study to remote sensing of asteroid surfaces.

BACKGROUND

The understanding and interpretation of spectral reflectance data is based on classical transmission spectroscopy and it is important to be reminded of how the two techniques are related. Classical transmission spectroscopy is based on the Beer–Lambert Law:

$$I = I_o e^{-kd}, \qquad \text{(eqn 1)}$$

(Wendlandt and Hecht, 1966; Kortum, 1969) where I is the intensity of light measured, I_o is the intensity of the incident light, k is the absorption coefficient characteristic of the material being measured, and d is the thickness of the material the light is passing through.

Transmission spectroscopic techniques applied to minerals have been interpreted by Burns (1970) in terms of crystal field theory. Elements of the first transition series and especially their petrologically significant cations, Fe^{2+} and Ti^{3+}, have an outer unfilled d-shell in their electron distribution. The electron distribution of the five possible d-shell orbitals are shown in Figure 1a. When such a cation is located in a crystal site (shown schematically in Figure 1a), certain orbitals experience strong electronic repulsions and greater energy is required for an electron to reside in such an orbital. The

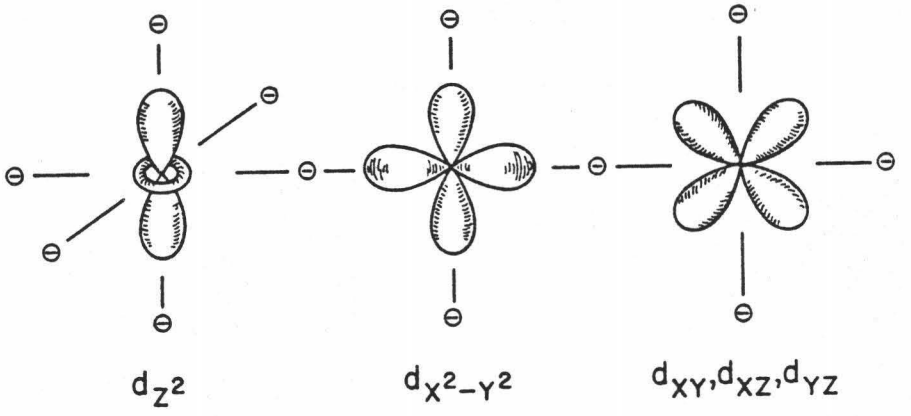

Figure 1a. Distribution of electron probability for d-orbitals within an octahedral crystal lattice site (after Gaffey and McCord, 1979).

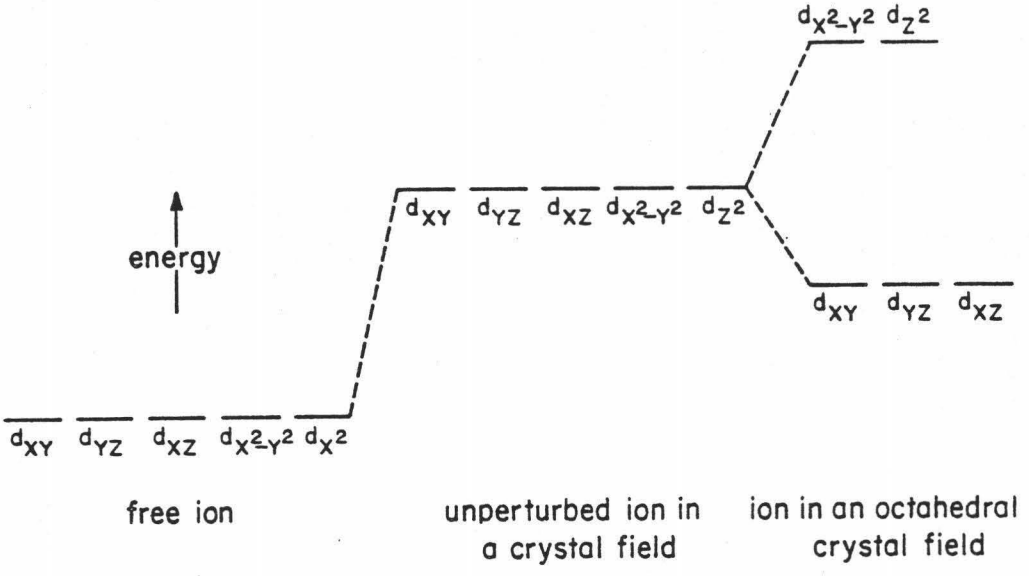

Figure 1b. Relative energy levels of the d-orbitals of a transition metal cation as a free ion, an unperturbed ion in a crystal field, and the crystal field splitting in an octahedral site (reproduced from Burns, 1970)

orbitals undergoing the least electronic repulsion become the ground state orbitals in which the electrons tend to reside (Figure 1b). The energy difference between the ground state and any excited state is termed the crystal field splitting energy (CFSE) and is a direct function of a particular cation and the crystal site in which it is located. A photon whose energy corresponds to the splitting energy of a cation located within a crystal site can be absorbed. These electronic transitions of the first transition element series, result in absorptions in the visible and near-infrared region of the electromagnetic spectrum (Burns, 1970), and are due to ions located within specific crystallographic sites so that from the spectra direct information is obtained concerning the chemistry and crystal structure of the material. White and Keester (1966) have outlined the mineralogical parameters which can influence the spectrum arising from a given transition ion in order of importance as follows: 1)the coordination number and valence state are, by far, the most important factors as they determine the main features of the spectra; 2)the nature of the ligand; 3)the distortion of the transition metal ion site; and 4)the metal-oxygen distances.

Reflection spectroscopy is the technique of measuring light reflected from a surface and comparing it to the light incident on it. The reflectance of a surface can be expressed as:

$$r = r_1 + e^{-k\bar{l}}, \qquad \text{(eqn 2)}$$

where r is the measured reflectance, r_1 represents the light which has not undergone absorption and as such represents the single and multiple Fresnel reflection (light which has never actually entered the

material), the exponential term represents the light which has entered the particle and has scattered out of the surface, k is the absorption coefficient of the material, and $\bar{l}$ is the mean optical path length of light in the material (MOPL, Clark and Roush, 1984). Equation 2 is a simplification of a more complex situation and is used only to show the relationship between reflectance and transmission spectroscopy which is contained in the second term on the right side of equation 2 (for a more rigorous discussion of reflectance spectroscopy the reader is referred to Clark and Roush, 1984 and references contained within). Hence, absorptions identified in transmission measurements are also present in reflectance. The applicability of reflectance spectroscopy is the ability to detect chemical and mineralogical information about a surface without having to be in contact with it and as such, has been used to investigate the surface composition for most bodies throughout the solar system. In fact, a wide variety of room temperature, laboratory-based spectral measurements exist for transition metal-bearing silicates (Adams, 1974, 1975; Burns et al., 1972; Hunt and Salisbury, 1970; Hunt et al., 1972, 1974; Nash and Conel, 1974; Singer, 1981, 1980) and form the basis for interpretation of earth-based telescopic spectral reflectace data (Adams and McCord, 1970; Charette et al., 1972; McCord et al., 1977; Gaffey and McCord, 1979; Singer, 1980; and references within all).

There are parameters which affect reflectance spectra (eg. viewing geometry, grain size, etc.) which are unrelated to chemical composition and crystallography. Burns (1970) briefly discusses the influence varying temperature would have on absorption spectra as being two-fold. For a given crystallographic site the width of an absorption feature is related to the amplitude of atomic vibrations about the center position

of the site (Burns, 1970). Assuming parallel, or near parallel energy levels, one would expect that increased thermal vibrations would result in a broadening of an absorption feature while decreased thermal vibration would result in a narrowing of the same feature. Also, the intensity of of the crystal field, and thus the CFSE, is a function of the metal-oxygen distance. Therefore, any expansion or contraction of a crystallographic site due to temperature variations would result in increasing or decreasing the CFSE and be expressed in reflectace spectra as a shifting of the absorption band minimum to longer or shorter wavelengths, respectively. Differential thermal expansion could act to drastically alter the symmetry of a crystallographic site thus changing the relative intensities of crystal field bands. For example, consider an exactly centrosymmetric crystal site at a given temperature, in this case any crystal field transitions are forbidden by the Laporte selection rule. At a different temperature, due to differential expansion the site would become non-centrosymmetric and the Laporte selection rule is relaxed allowing crystal field transitions to occur. Thus, although surface temperature is independent of chemical composition it can affect crystallographic site symmetry and metal-oxygen distances, thus spectra obtained by transmission and reflectance techniques can be affected.

Low temperature transmission spectral studies for enstatite (Runciman et al., 1973a), olivine (Runciman et al., 1973b, 1974), and a variety of minerals (Smith, 1977) have been reported. All of these papers deal with assignment of absorption features in the minerals to specific electronic transitions. None of these studies include reflectance measurements and the authors' do not address shifts in band centers. Runciman et al., (1974), show the three polarized components

of the ≈1μm olivine absorption band at both 19K and 297K (Figure 2). Seen clearly in each orientation is the narrowing of the absorption feature with decreased temperature. Subtle, but most outstanding in the β spectrum, is the shift of the peak of the absorption band to shorter wavelengths (higher energies) at the lower temperature.

The most comprehensive study to date involving increased temperature effects on crystal field spectra and implications for remote sensing is presented by Sung et al., (1977). The authors present a series of polarized and unpolarized absorption spectra, as well as, diffuse reflectance spectra of olivine, clinopyroxene, and orthopyroxene from room temperature to ≈675K. Their results confirm the broadening of absorption bands and shifting of band minima discussed above. However, as they point out, the higher temperature spectra are dominated by thermal emmision of the sample at wavelengths greater than about 1.4μm, thus eliminating information for the "2μm" pyroxene absorption band. The study presented here has successfully made specific measurements designed to remove the thermal component from the reflectance spectra, thus allowing spectral changes of the 2μm region to be examined for the first time at elevated temperatures.

Several high temperature X-ray crystallographic studies of olivine (Smyth and Hazen, 1973; Brown and Prewitt, 1973; Smyth, 1975), orthopyroxene (Smyth, 1973; Sueno et al., 1976), and clinopyroxene (Cameron et al., 1973; Brown et al., 1972; Smyth, 1974) confirm the distortion of crystallographic sites as a function of increasing temperature. The data exhibit two general trends: (1)coordination polyhedra show differential thermal expansions; silicate tetrahedra remain essentially constant, while metal octahedra show positive, somewhat linear expansion and (2)individual metal-oxygen distances in various sites have

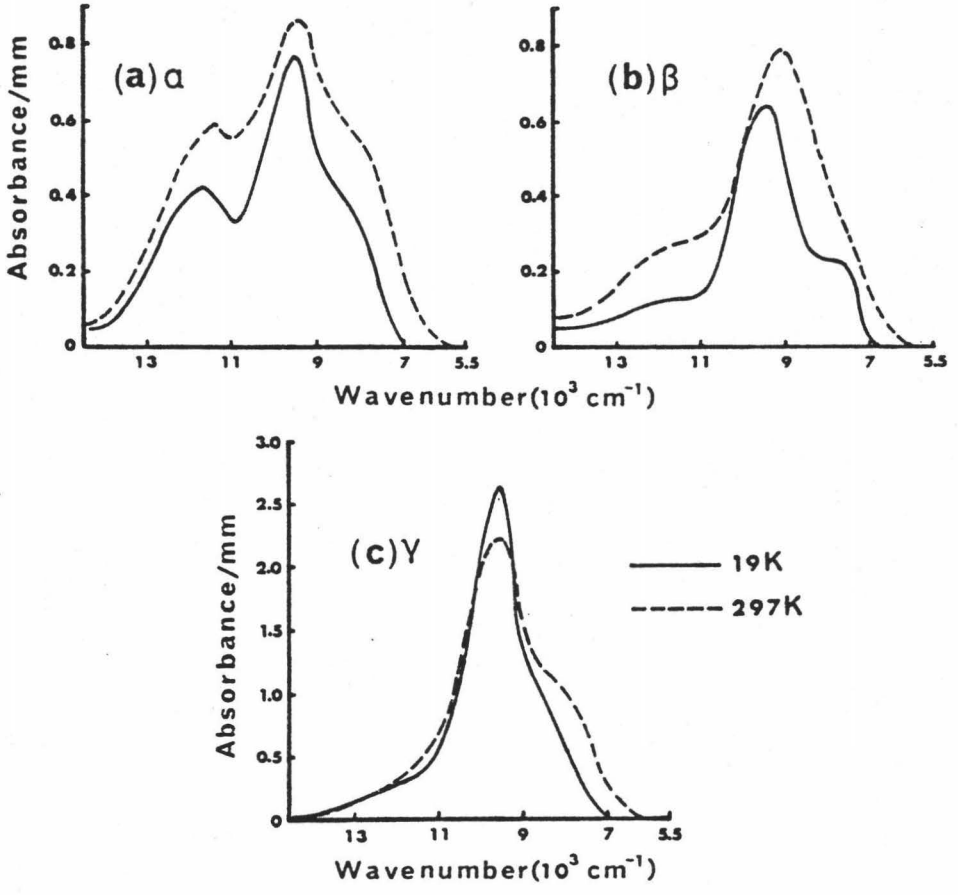

Figure 2. Polarized absorption spectra of olivine at 19K (solid line) and 297K (from Runciman et al., 1974).

individual variations, thus affecting relative site symmetry and coordination. There are few low temperature (liquid nitrogen) X-ray studies of mafic minerals but a couple do exist for olivine (Hazen 1976, 1977), both of which exhibit the same general trends of the high temperature studies. High temperature X-ray studies on oriented single crystals are recently reviewed by Hazen and Finger (1983).

Thus, there is great potential for the reflectance spectra of mafic minerals to be effected by varying temperature. The remainder of this thesis will present the results of a laboratory study designed to directly address this question. Chapter 2 will describe the laboratory methods, devices, and samples used in this study to obtain the reflectance spectra presented in Chapter 3. Chapter 4 will present various quantitative analysis techniques used to characterize variation in the measured reflectance of the samples as a function of temperature. Application of the laboratory measurements to planetary surfaces is presented in Chapter 5 for the specific case of asteroid-like surfaces. Finally, Chapter 6 attempts to summarize the results of both the laboratory measurements and subsequent analysis.

REFERENCES

Adams, J.B. (1974), Visible and Near-Infrared Diffuse Reflectance Spectra of Pyroxenes as Applied to Remote sensing of Solid Objects in the Solar System., JGR, 79, 4829-4863.

Adams, J.B. (1975), Uniqueness of Visible and Near-Infrared Reflectance Spectra of Pyroxenes and Other Rock-Forming Minerals. In Infrared and Raman Spectroscopy of Lunar and Terrestrial Minerals (C. Karr, Ed.), p91-116, Academic Press, New York,NY.

Adams, J.B. and McCord, T.B. (1970), Remote Sensing of Lunar Surface Mineralogy: Implications from Visible and Near-Infrared Reflectivity of Apollo 11 Samples., Proc. Apollo 11 Lunar Sci. Conf., 1937-1945.

Brown, G.E. and Prewitt, C.T., (1973), High Temperature Crystal Chemistry of Hortonolite., Am. Mineral., 58, 577-587.

Brown, G.E., Papike, J.J., and Sueno, S., (1972), A Comparison of the Structures of Low and High Pigeonite., JGR, 77, 5778-5789.

Burns, R.G., (1970), Mineralogical Applications of Crystal Field Theory, Cambridge Univ. Press, London., 224p.

Burns, R.G., Huggins, F.E.. and Abu-Eid, R.M., (1972), Polarized Absorption Spectra of Single Crystals of Lunar Pyroxenes and Olivines., The Moon, 4, 93-102.

Cameron, M.P., Sueno, S., Prewitt, C.T., and Papike, J.J., (1974), High Temperature Crystal Chemistry of Acmite, Diopside, Hedenbergite, Jadite, Spodumene, and Ureyite., Am. Mineral., 58, 594-618.

Charette, M.P., McCord, T.B., Pieters, C., and Adams, J.B., (1974), Applications of Remote Spectral Measurements to Lunar Geology Classification and Determination of Titanium Content of Lunar Soils., JGR, 79, 1605-1613.

Clark, R.N. and Roush, T.L., (1984), Reflectance Spectroscopy: Quantitative Analysis Techniques for Remote Sensing Applications, In press.

Gaffey, M.J. and McCord, T.B., (1979), Mineralogical and Petrological Characterizations of Asteroid Surface Material., In Asteroids (T. Gehrels, Ed.)., Univ. Arizona Press, Tucson, Arizona.

Hazen, R.M., (1976), Effects of temperature and pressure on the crystal structure of forsterite, Am. Mineral., 61, 1280-1293.

Hazen, R.M., (1977), Effects of temperature and pressure on the crystal structure of ferromagnesian olivine, Am. Mineral., 62, 286-295.

Hazen, R.M. and Finger, L.W., (1983) Comparative Crystal Chemistry, John Wiley and Sons, New York, NY, 231p.

Hunt, G.R. and Salisbury, J.W., (1970), Visible and Near-Infrared Spectra of Minerals and Rocks: I. Silicate Minerals., Mod. Geol., 1, 283-300.

Hunt, G.R., Salisbury, J.W., and Lenhoff, C.J., (1972), Visible and Near-Infrared Spectra of Minerals and Rocks: VI. Additional Silicates., Mod. Geol., 4, 85-106.

Hunt, G.R., Salisbury, J.W., and Lenhoff, C.J. (1974), Visible and Near-Infrared Spectra of Minerals and Rocks: IX. Basic and Ultrabasic Igneous Rocks., Mod. Geol., 5, 15-22.

Kortum, g., (1969) Reflectance Spectroscopy, Springer-Verlang, New York, NY, 366p.

McCord, T.B., Adams, J.B., and Huguenin, R.L., (1977), Reflection Spectroscopy: A Technique for Remotely Sensed Mineralogy and Composition., NASA Special Papers on Orbital Science.

Nash, D.B. and Conel, J.E., (1974) Spectral Reflectance Systems for Mixtures of Powdered Hypersthene, Labradorite, and Illmenite., JGR, 79, 1615-1621.

Runciman, W.A., Sengupta, D., and Gourley, J.T., (1973b), The Polarized Spectra of Iron in Silicates II. Olivine., Am. Mineral., 58, 451-456.

Runciman, W.A., Sengupta, D., and Gourley, J.T., (1974), The Polarized Spectra of Iron in Silicates II. Olivine: A Reply., Am. Mineral., 59, 630-631.

Runciman, W.A., Sengupta, D., and Marshall, M., (1973a), The Polarized Spectra of Iron in Silicates. I. Enstatite., Am. Mineral., 58, 444-450.

Singer, R.B., (1980), The Dark Materials on Mars: II. New Mineralogic Interpretations from Reflectance Spectroscopy and Petrologic Implications., Lunar Planet. Sci. Conf. XI Abstr., 1048-1050.

Singer, R.B., (1981), Near-Infrared Spectral Reflectance of Mineral Mixtures: Systematic Combinations of Pyroxenes, Olivine, and Iron Oxides., JGR, 86, 7967-7982.

Smith, G., (1977), Low-Temperature Optical Studies of Metal-Metal Charge-Transfer Transitions in Various Minerals., Can. Mineral., 15, 500-507.

Smyth, J.R., (1973), An Orthopyroxene Structure Up to 850°C., Am. Mineral., 58, 636-648.

Smyth, J.R., (1974), The High Temperature Crystal Chemistry of Clinohypersthene., Am. Mineral., 59, 1069-1082.

Smyth, J.R., (1975), High Temperature Crystal Chemistry of Fayalite., Am. Mineral., 60, 1092-1097.

Smyth, J.R. and Hazen, R.M., (1973), The Crystal Structures of Foresterite and Hortonolite at Several Temperatures Up to 900°C., Am. Mineral., 58, 588-593.

Sueno, S., Cameron, M., and Prewitt, C.T., (1976), Orthoferrosilite: High Temperature Crystal Chemistry., Am. Mineral., 61, 38-53.

Sung, C., Singer, R.B., Parkin, K.M., and Burns, R.G., (1977), Temperature Dependence of Fe^{2+} Crystal Field Spectra: Implications to mineralogical Mapping of Planetary Surfaces., Proc. Lunar Sci. Conf. VIII., 1063-1079.

Wendlandt, W.W. and Hecht, H.G., (1966) Reflectance Spectroscopy, Interscience, New York, NY, 298p.

White, W.B. and Keester, K.L., (1966), Optical Absorption Spectra of Iron in the Rock-Forming Silicates., Am. Mineral., 51, 774-791.

CHAPTER II: METHODOLOGY

METHODOLOGY

Instrumentation

Spectra were obtained using the University of Hawaii Planetary Geosciences Division spectrogoniometer. This device is highly versatile and can be used for bidirectional reflectance measurements of virtually any material. The specific details of this instrument are describe by Singer (1981). It should be noted that this device uses state-of-the-art astronomical instrumentation for wavelength discrimination, light detection, and data handling. This provides a very high signal-to-noise and a direct means of comparison with earth-based telescopic observations. Spectral coverage extends from 0.4 to 2.6μm with a spectral resolution ($\Delta\lambda/\lambda$) of approximately 1.5%. Because of the single-beam nature of this instrument it was easy to make direct measurements of thermal emission from the sample at each temperature. This thermal component was then subtracted out during data processing, resulting in true reflectance values. The procedure used, for each wavelength channel, is:

$$\text{Sample Reflectance} = \left[\frac{S_{\text{samp.ill.}} - S_{\text{samp.dk.}}}{S_{\text{std.ill.}} - S_{\text{std.dk.}}}\right](\text{NBS Halon}), \quad \text{(eqn 1)}$$

where: $S_{\text{samp.ill.}}$ is the signal measured from the illuminated sample, $S_{\text{samp.dk.}}$ is the signal measured from the sample with the light source blocked (thermal emission and scattered light), $S_{\text{std.ill.}}$ is the signal measured from the illuminated reflectance standard, $S_{\text{std.dk.}}$ is the signal measured from the reflectance standard with the light source blocked (thermal emission and scattered light), and NBS Halon is the National Bureau of Standards determined reflectance for Halon.

For this study an environment chamber designed by R. Hamilton Brown for low temperature spectral measurements was modified, by addition of a small sample oven, for use at elevated temperatures as well. The chamber consists of a liquid nitrogen reservoir with an inner evacuable chamber which has two sapphire windows situated such that only a phase angle of about 12° is possible. For these measurements the angle of incidence (i) and emission (e) were equal (e=i=6°). All measurements were taken with the sample and reflectance standard in vacuum to preclude any chance of frost growth at low temperatures or oxidation at high temperatures and no sample alteration was observed. The time required for the sample to reach and stabilize at a given temperature was typically one hour. Sample temperature is maintained during observations to within ±1K by servo-electronics controlling the power to the sample oven. The servo-electronics are directly linked to a flat platinum resistance element buried ≈3mm in the particulate sample, and temperatures are displayed using a commercial digital temperature read-out. A schematic cross section of the environment chamber is presented in Figure 3.

Reflectance Standard

Halon powder, a fluorocarbon manufactured by Allied Chemical Corp., was used as a diffuse reflectance standard. Documentation of the absolute reflectance properties of Halon and preparation techniques were obtained from Weidner and Hsia (1981). Because of the potential mineralogical significance of subtle features in the 2μm region, laboratory spectra presented here were corrected for the slightly imperfect reflectance of Halon. The final results are believed to be within one to two percent of absolute level of bidirectional reflectance, depending on the signal-to-noise ratio of the detector.

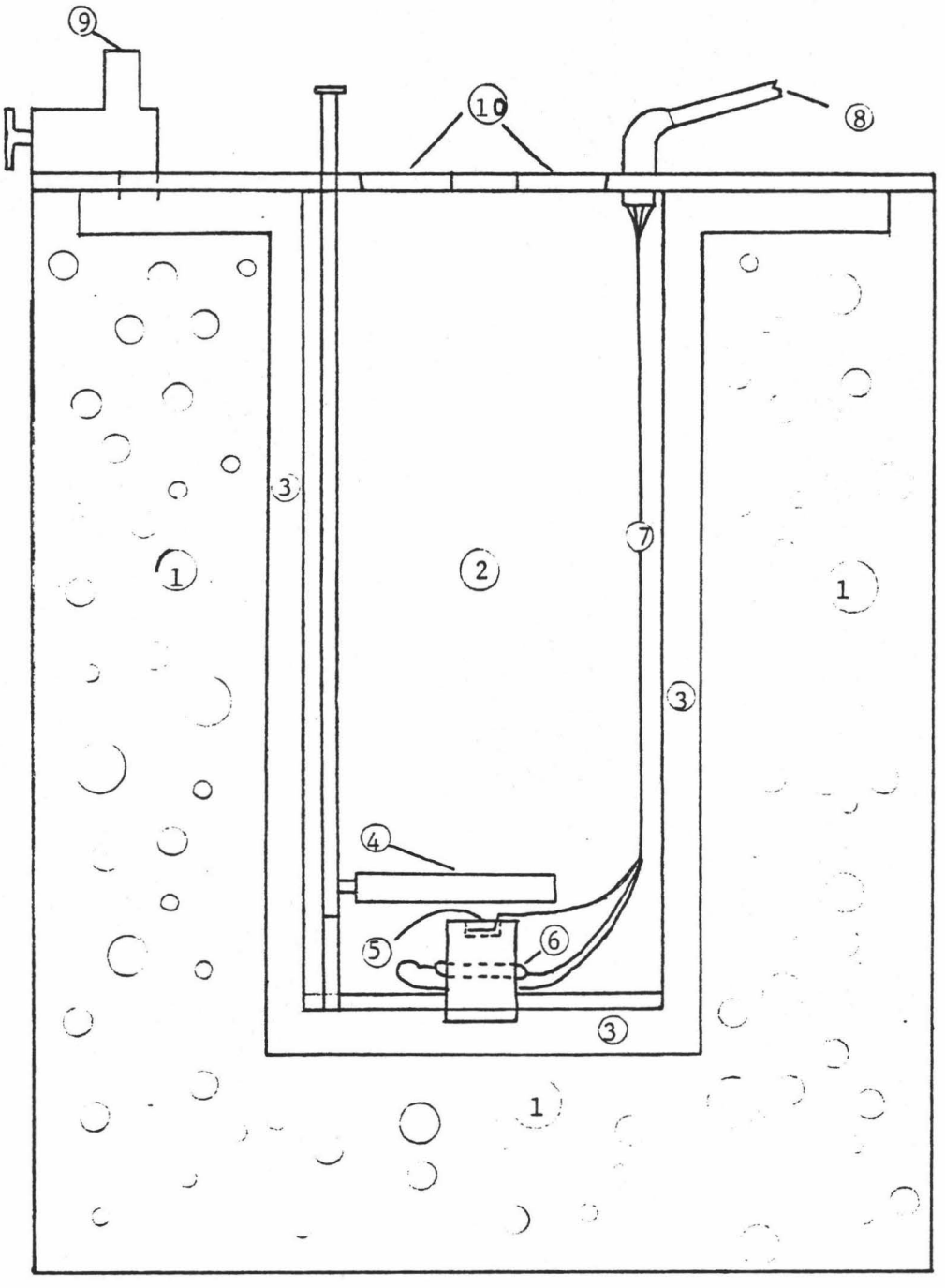

Figure 3. Schematic diagram of environment chamber. 1)Outer can with polyurethane foam insulation, 2)Inner evacuable can, 3)Liquid nitrogen reservoir, 4)Reflection standard holder, 5)Sample holder with temperature probe, 6)Heating element, 7)Electrical connections, 8)Electrical connections leading to temperature indicator and heater power supply, 9)Vacuum pump valve, 10)Sapphire windows.

Sample Preparation

Individual samples were chosen to represent characteristic spectral properties of mineral classes prominent of mafic to ultramafic assemblages. All samples are prepared by crushing with a hardened steel mortar and pestle, followed by grinding in an alumina mortar and pestle. A 45-90μm grain size fraction was seperated by wet sieving with methanol and used for all subsequent measurements with the exception of the plagioclase which has a grain size of 45-108μm.

Data Analysis

Each spectrum presented here consists of a number of individual observations of the sample which were averaged to improve signal-to-noise and then divided by an average of reflectance standard observations taken nearly contemporaneously. All data processing was carried out in digital form using an interactive computer program (Clark, 1980) and formal errors were calculated for each operation. Where data are presented with error bars they represent ± 1 standard deviation of the mean.

Sample Descriptions

Olivines(OLV01 and OLV03)

OLV01

This sample has been characterized in detail by Singer (1981) and is a Forsterite (Chrysolite variety, Fo_{89}) from South Point, Hawaii. A chemical analysis is presented in Table 1.

OLV03

This sample was provided on request by the National Museum of Natural History (NMNH) of the Smithsonian Institution and is a Fayalite(Fo_0) from Rockport, Massachusetts, NMNH catalog number R3517. A detailed chemical analysis is presented in Burns and Huggins (1972)

and is included in Table 1. Optical examination of the sample, using a binocular dissecting microscope, revealed that the sample contained an abundant opaque contaminant, probably magnetite. An attempt to remove this opaque component magnetically after the grinding procedure, appears to have been unsuccessful as evidenced by the overall low reflectance of the sample in the near-infrared (see Figure 5).

Orthopyroxenes(PYX02 and PYX08)

PYX02

This sample has been characterized in detail by Singer (1981) and is an Enstatite (bronzite variety, En_{86}) from Bamble, Norway. A chemical analysis is included in Table 1. It appears the tremolite contaminant discussed by Singer (1981) has been successfully removed as evidenced by the lack of the absorption feature located at $\approx 2.3\mu m$

PYX08

This sample, the enstatite component of a websterite (enstatite variety, En_{88}), from Webster, North Carolina (provided by Trude King) and was discussed by King et al., (1981). A chemical analysis is included in Table 1. Since this sample is quite similar in composition to the previous sample it is not surprising that it exhibits the same manner of spectral behavior.

Clinopyroxene(PYX07)

This sample has been characterized in detail by Singer (1981) and is a Diopsidic-Augite ($Wo_{42}En_{51}Fs_7$). Its chemical analysis can be found in Table 1.

Plagioclase(PLAG01)

This sample is a plagioclase feldspar (labradorite variety) from Lake County, Oregon (provided by Trude King) and is discussed by King et al., (1981). Due to limited quantity, a grain size seperate of 45-

108μm was used for spectral measurements of this sample. Data was collected for this sample at 81K and a room temperature spectra of a different grain size (<45μm), and different viewing geometry (i=e=15°), was provided by Trude King.

Basaltic Assemblage(PYX09)

This sample was provided by John Adams and was labelled as pigeonite however, after the 45-90μm grain size fraction was seperated from the bulk sample and spectral data collected it became apparent this sample was not a pure pigeonite. Subsequent examination using a petrographic microscope has identified plagioclase, olivine, clinopyroxene, orthopyroxene, and a true pigeonite showing the characteristic exsolution lamellae.

Table 1. Chemical Analysis of Samples Used

	OLV01†	OLV03[2]	PYX02†	PYX08[3]	PLAG01	PYX07†	PYX09
SiO_2	38.90	29.70	55.30	57.28	NA	50.10	NA
TiO_2	0.03	0.00	0.05	0.01	NA	0.66	NA
Al_2O_3	0.46	0.00	0.12	1.08	NA	2.71	NA
Fe_2O_3	‡	n.d.	‡	‡	NA	1.11	NA
FeO	10.70	68.60	9.38	7.91	NA	4.00	NA
MnO	0.22	2.00	0.15	0.21	NA	0.24	NA
MgO	47.20	0.10	32.80	33.96	NA	17.60	NA
CaO	0.41	0.01	0.45	0.23	NA	20.00	NA
Na_2O	0.00	NA	0.00	0.08	NA	0.19	NA
K_2O	0.02	NA	0.02	0.01	NA	0.01	NA
P_2O_5	0.02	NA	0.01	NA	NA	0.01	NA
LOI	0.77	NA	2.00	NA	NA	0.69	NA
Total	98.73	100.41	100.28	100.77	NA	97.33	NA

† from Singer (1981)

2 from Burns and Huggins (1972)

3 average of 6 microprobe analysis provided by Trude King

Lost on ignition (indicative of volatiles)

n.d. not determined

NA not available

‡ as FeO

REFERENCES

Burns, R.G. and Huggins, F.E., (1972), Cation Determinative Curves for Mg-Fe-Mn Olivines from Vibrational Spectra, Am. Mineral., 57, 967-985.

Clark, R.N., (1980), A Large Scale Interactive One Dimensional Array Processing System., Publ. Astron. Soc. Pac., 92, 221-224.

King, T.V.V., Pieters, C.M., and Sandlin, D.L., (1981), Particulate Mineral Mixtures: The Relation of Albedo and Apparent Absorption Band Strength., Lunar Planet. Sci. Conf. XII Abstr., 547-549.

Singer, R.B., (1981), Near-Infrared Spectral Reflectance of Mineral Mixtures: Systematic Combinations of Pyroxenes, Olivine, and Iron Oxides., JGR, 86, 7967-7982.

Weidner, V.R. and Hsia, J.J., (1981), Reflection properties of pressed polytetrafluoroehtylene powder., J. Opt. Soc. Am., 71, 856-861.

CHAPTER III: PRESENTATION OF MEASUREMENTS

MEASUREMENTS

OLIVINES

OLV01

At all temperatures, the spectra of this sample display the crystal field absorptions, due to Fe^{2+}, at slightly longer than 1μm (≈1.05μm) which is typical and diagnostic of olivine (Adams, 1974), which has no broad absorptions located at longer wavelengths such as the pyroxenes discussed below. The major effect of increasing temperature is to broaden this absorption feature, mainly on the low energy, longer wavelength, side, as seen in Figure 4. Also, the weak absorption located at ≈.63μm, is well pronounced at low temperatures but becomes a mere inflection at the higher temperatures.

OLV03

The same general trends described above also hold true for this olivine (see Figure 5) except that the apparent reflectance minima are located at shorter wavelengths (≈1.03μm), which is in conflict with previous measurements of Fe-rich olivines (Burns, 1970; Hunt and Salisbury, 1970; Adams, 1975). However, as noted in the previous chapter, there is some question concerning the purity of this sample.

ORTHOPYROXENES

PYX02

The spectra of this sample exhibit absorptions slightly short of 1- and 2μm, Figure 6, which are typically associated with low calcium orthopyroxenes (Adams, 1974, 1975). The shorter wavelength feature apparent reflectance minimum remains fairly constant while the longer wavelength apparent reflectance minimum shifts to longer

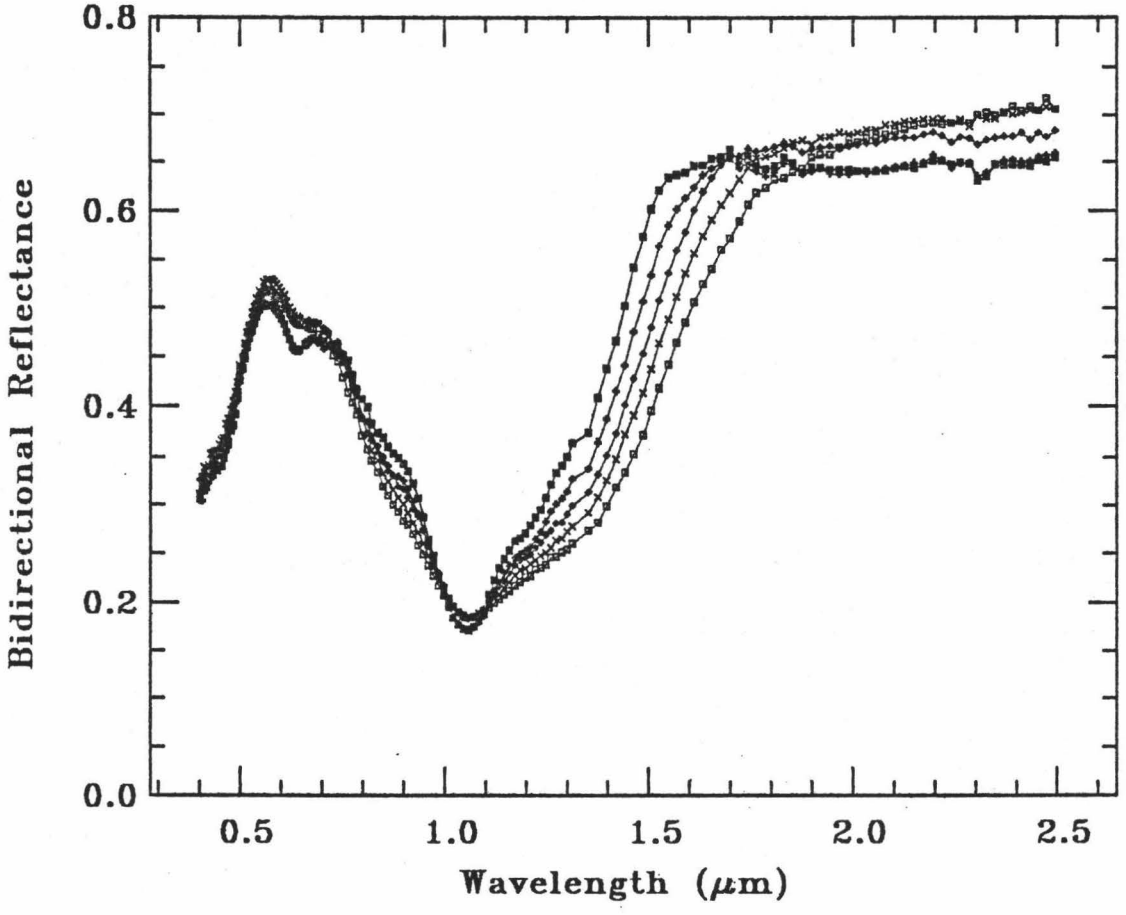

Figure 4. Overlay of forsteritic olivine spectra at all temperatures. Filled squares are measurements at ≈80K. Pluses are measurements at 173K. Diamonds are measurements at 273K. Crosses are measurements at 373K. Open squares are measurements at 448K.

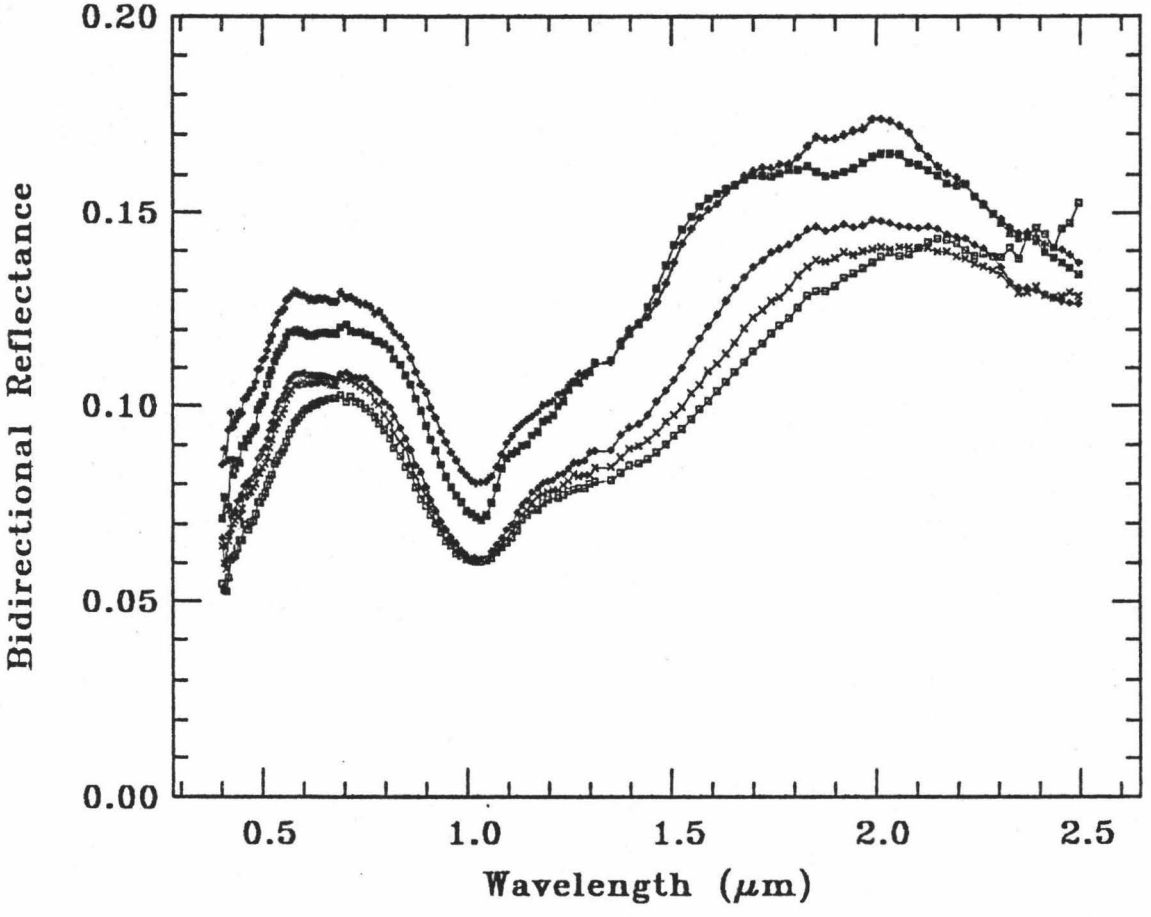

Figure 5. Overlay of fayalitic olivine spectra at all temperatures. Filled squares are measurements at ≈80K. Pluses are measurements at 173K. Diamonds are measurements at 273K. Crosses are measurements at 373K. Open squares are measurements at 448K.

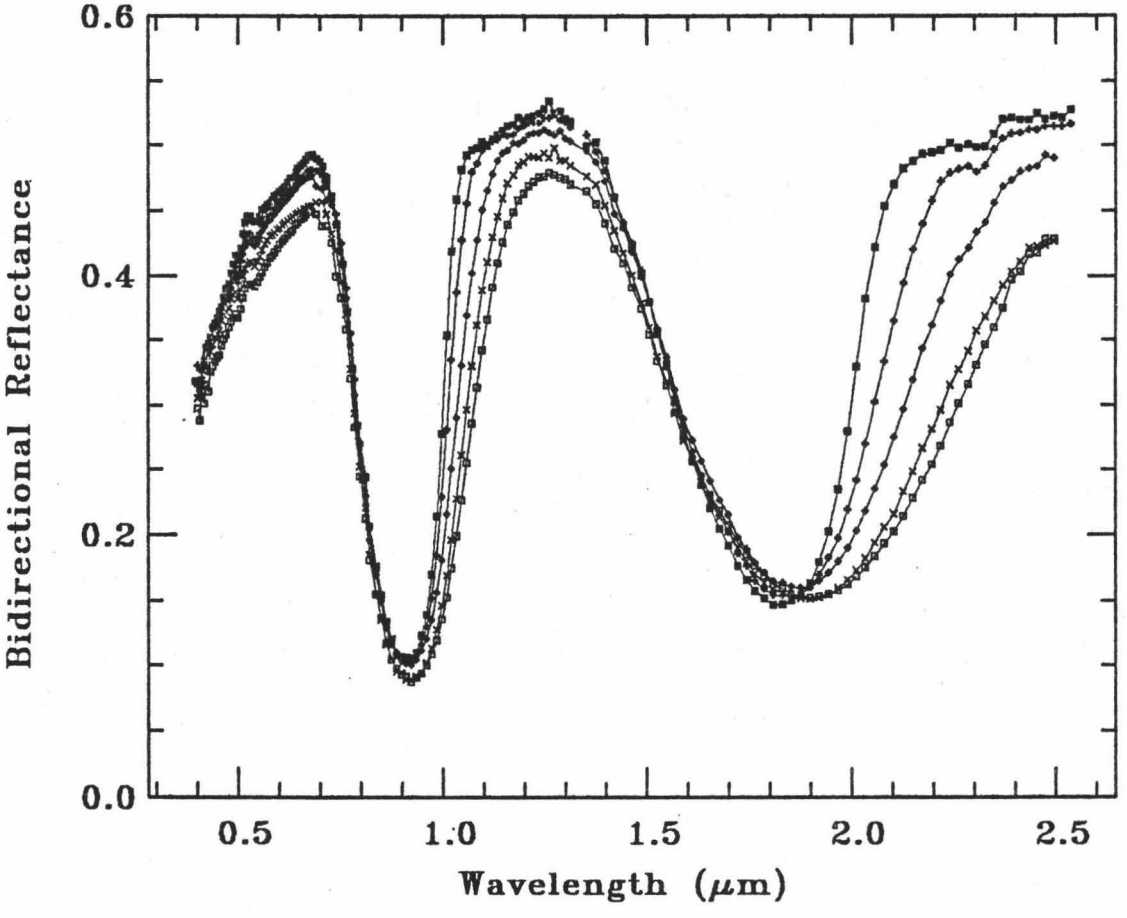

Figure 6. Overlay of PYX02 spectra at all temperatures. Filled squares are measurements at ≈80K. Pluses are measurements at 173K. Diamonds are measurements at 273K. Crosses are measurements at 373K. Open squares are measurements at 448K.

wavelengths as temperature increases, Figure 6. Both features broaden, mainly on the lower energy (longer wavelength) side as temperature increases. Also, the region from ≈.4 to .7μm decreases in slope as temperature increases.

PYX08

Since this sample is quite similar in composition to the previous sample, it is not surprising that it exhibits the same manner of spectral behavior as PYX02 (Figure 7).

CLINOPYROXENES

PYX07

The spectra of this sample exhibit the characteristic absorption bands, at slightly longer than 1- and 2μm, of the more Ca-rich clinopyroxenes (Adams, 1974, 1975), see Figure 8. As with the orthopyroxenes, the ≈1μm apparent reflectance minimum remains fairly constant as a function of temperature. However, in contrast to the orthopyroxenes, the ≈2μm apparent reflectance minimum shifts to shorter wavelengths, higher energies, as temperature increases.

PLAGIOCLASE

PLAG01

The spectra of this sample at liquid nitrogen and room temperature show little differences (Figure 9). The grain size differences between the two samples can result in differing band widths and overall reflectance levels. The finer grain size spectrum would have higher reflectance values and greater band widths.

BASALTIC ASSEMBLAGE

PYX09

Figure 10 shows the results of spectral measurements on this sample. At the lower temperatures, the orthopyroxene and clinopyroxene apparent reflectance minima, ≈1.9μm and 2.3μm respectivly, are seperately resolved, thus allowing immediate identification of these two minerals in the sample. Near room temperature (273K), and above, the seperate minima appear as one asymmetric band.

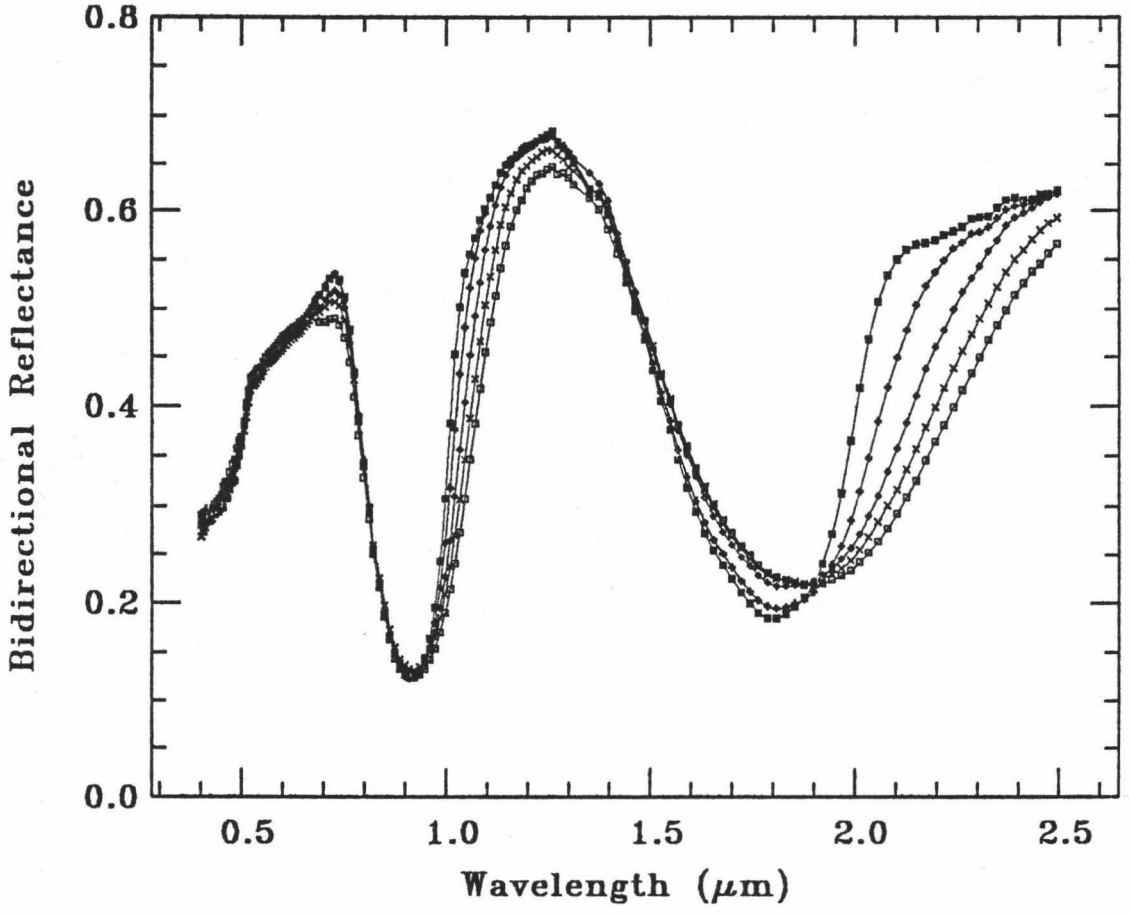

Figure 7. Overlay of PYX08 at all temperatures. Filled squares are measurements at ≈80K. Pluses are measurements at 173K. Diamonds are measurements at 273K. Crosses are measurements at 373K. Open squares are measurements at 448K.

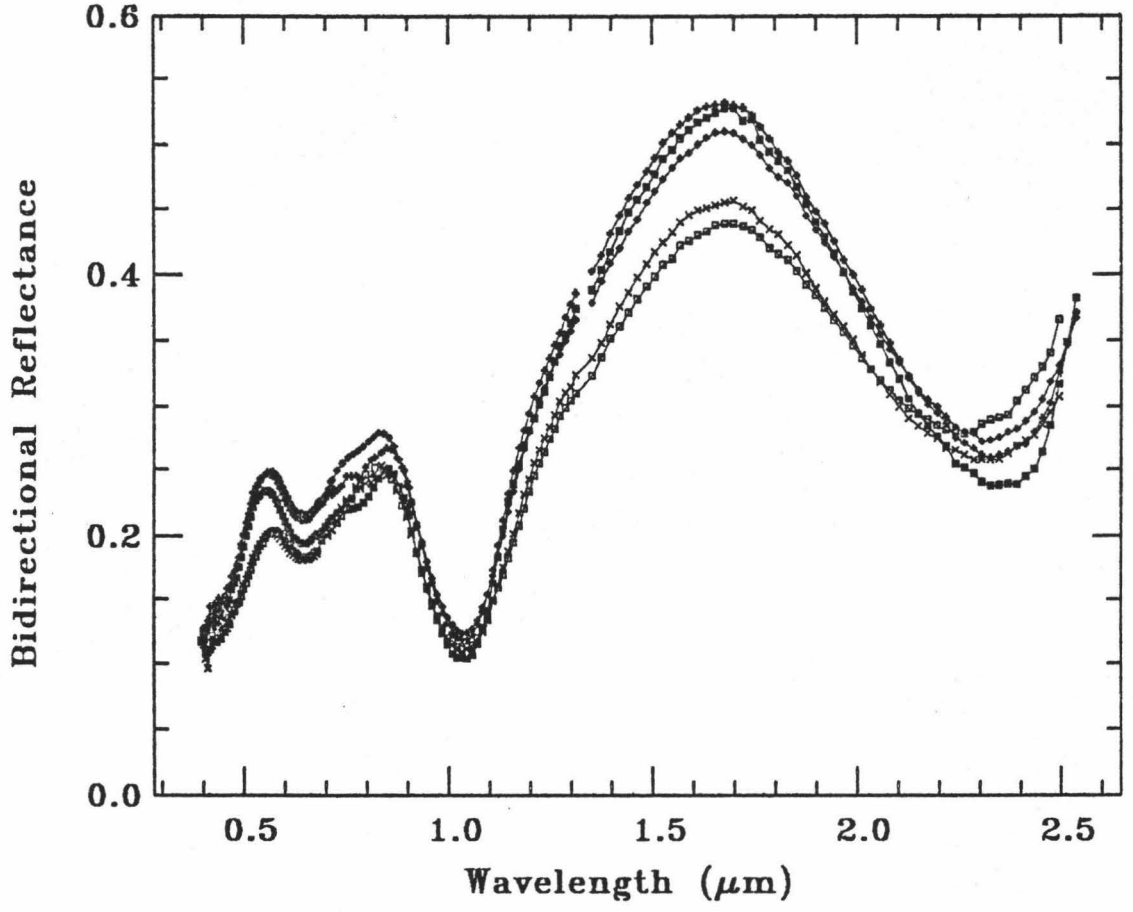

Figure 8. Overlay of PYX07 at all temperatures. Filled squares are measurements at ≈80K. Pluses are measurements at 173K. Diamonds are measurements at 273K. Crosses are measurements at 373K. Open squares are measurements at 448K.

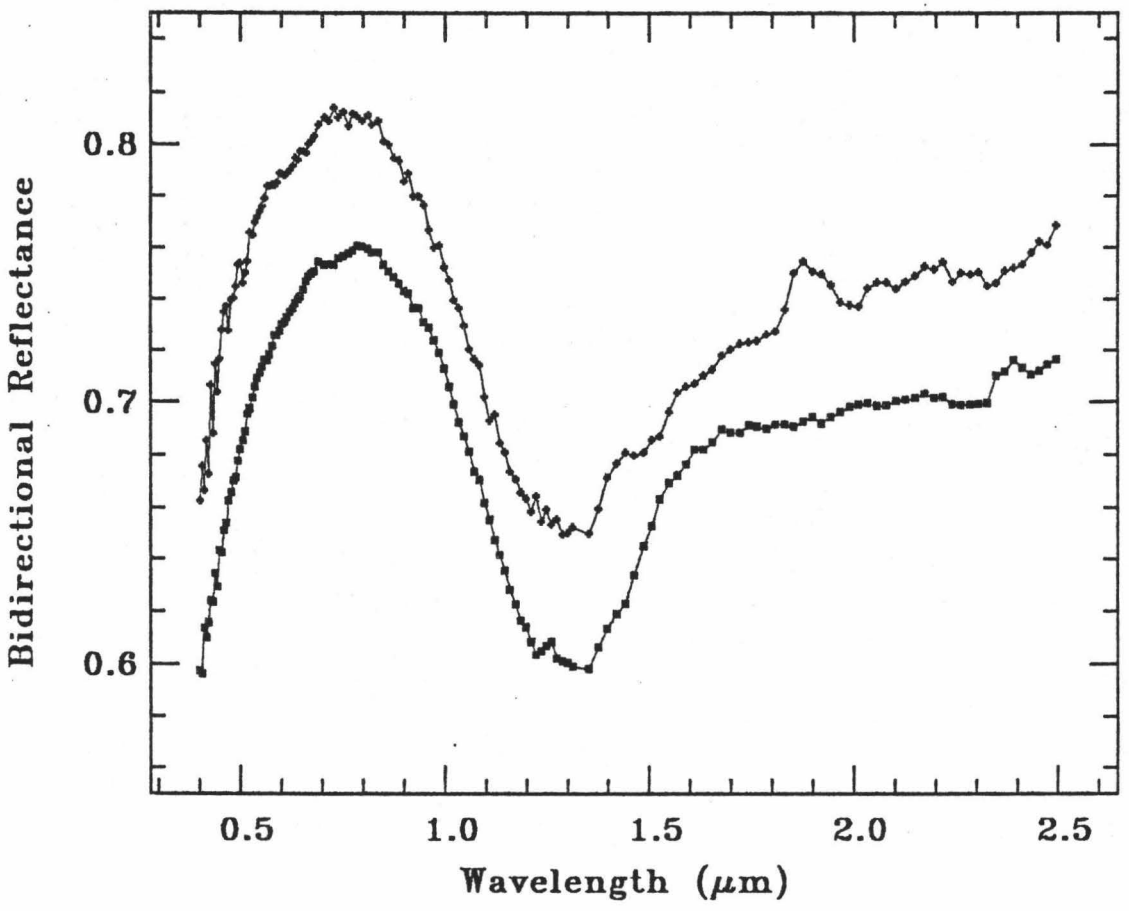

Figure 9. Overlay of plagioclase data at liquid nitrogen ≈80K (squares) and room temperature (pluses). Differences in overall reflectance levels are due to differing grain sizes.

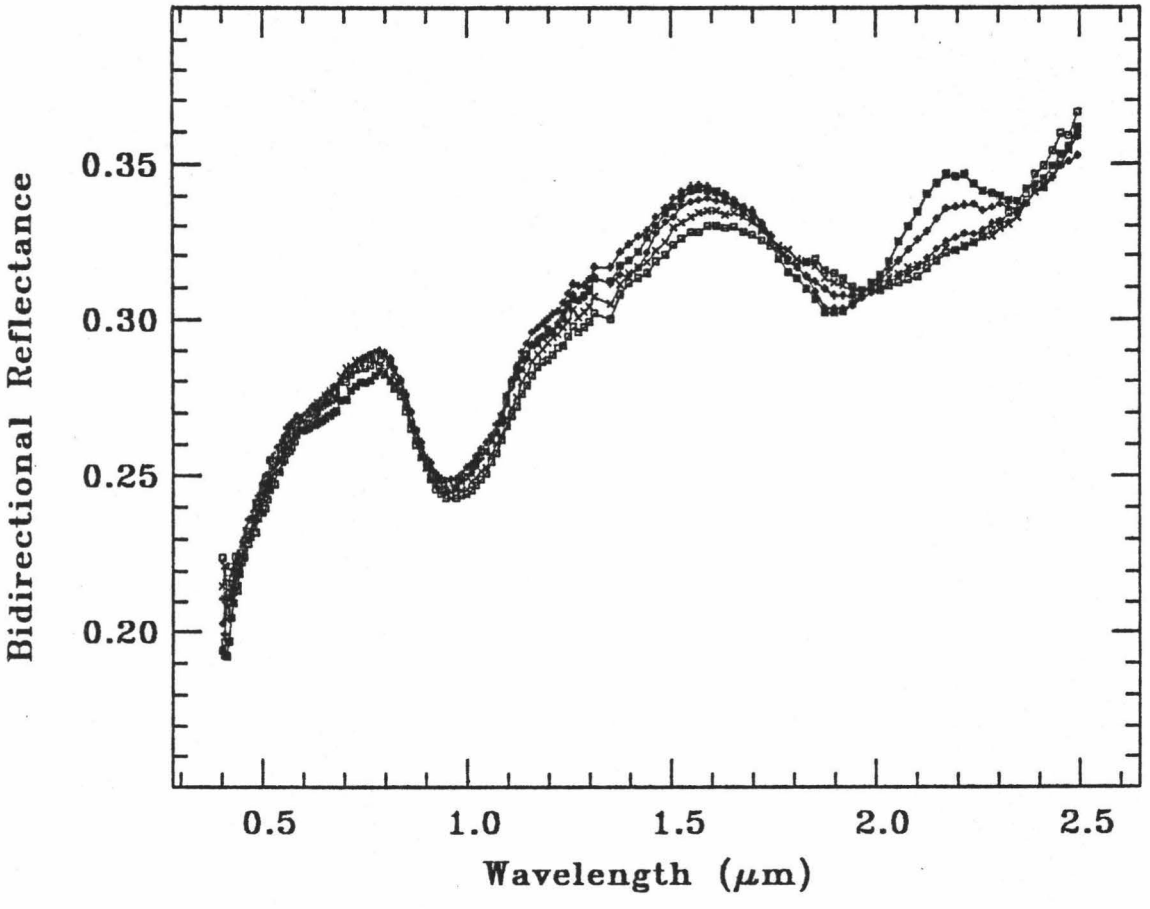

Figure 10. Overlay of basaltic assemblage at all temperatures. Filled squares are measurements at ≈80K. Pluses are measurements at 173K. Diamonds are measurements at 273K. Crosses are measurements at 273K. Open squares are measurements at 448K.

REFERENCES

Adams, J.B. (1974), Visible and Near-Infrared Diffuse Reflectance Spectra of Pyroxenes as Applied to Remote sensing of Solid Objects in the Solar System., JGR, 79, 4829-4863.

Adams, J.B. (1975), Uniqueness of Visible and Near-Infrared Reflectance Spectra of Pyroxenes and Other Rock-Forming Minerals. In Infrared and Raman Spectroscopy of Lunar and Terrestrial Minerals (C. Karr, Ed.), p91-116, Academic Press, New York,NY.

Burns, R.G., (1970), Mineralogical Applications of Crystal Field Theory, Cambridge Univ. Press, London., 224p.

Hunt, G.R. and Salisbury, J.W., (1970), Visible and Near-Infrared Spectra of Minerals and Rocks: I. Silicate Minerals., Mod. Geol., 1, 283-300.

CHAPTER IV: ANALYSIS OF MEASUREMENTS

ANALYSIS

In order to analyze the variation of characteristic spectral signatures as a function of temperature it is necessary to remove absorptions caused by other processes such as preferential scattering of light away from the detector or absorptions due to some contaminant or component not of interest. A continuum estimating the absorptions from other processes can be defined by using a suitable function such as a straight line segment, a polynomial, a Gaussian, et cetra. Once it is removed from the measured reflectance residual absorptions due to the process or mineral of interest are isolated. Examples of continua use are presented in Clark (1981, 1983), McCord et al. (1981), and Singer (1981) and a theoretical discussion concerning continua is given by Clark and Roush (1984).

This study will focus on absorptions due to octahedrally coordinated Fe^{2+} ions, located within various crystallographic sites. Reflectance spectra of olivines exhibit a compound absorption feature located around 1μm which is composed of absorptions due to Fe^{2+} located in both the olivine M(1) and M(2) crystallographic sites (Burns, 1974). Reflectance spectra of the pyroxenes exhibit two seperate absorptions located near 1- and 2μm which are both due to Fe^{2+} located in the pyroxene M(2) crystallographic site (Burns, 1970). Thus, for this study characterizations of the reflectance spectra will be limited to the 1μm region for olivine and the 1- and 2μm regions of the pyroxenes. For analysis, a subset of the spectrum is extracted which is bounded by points of maximum reflectance and are believed to lie outside the wavelength region of the absorption of interest. A straight line continuum is estimated by using the two end points of this data subset and is removed by dividing the reflectance values by the continuum values

at each wavelength. The clinopyroxene (PYX07) 2μm absorption band is difficult to characterize since the long wavelength side of the band can not be measured by our instrumentation. In this case, straight line continua were estimated using the reflectance maximum between the 1- and 2μm absorption bands and the last data point (usually a sloping line) and compared with a continuum estimated by setting the last data point equal to the reflectance maximum between the 1- and 2μm absorption bands (a horizontal line). After continuum removal, the values of results obtained by these two methods were compared and they were the same. A more complex polynomial was not used because it was felt that direct comparisons between various minerals, and the same mineral at various temperatures, would be facilitated by the consistent use of straight line continua. After continuum removal, the true band minimum (TBM), defined as the wavelength at which the reflectance relative to the continuum is a minimum, is determined. The TBM for all minerals are plotted as a function of temperature for the 1- and 2μm regions in Figures 11 and 12 respectively. Since the variation in TBM seen in Figure 11 corresponds to a single wavelength channel difference of the detector, well within the error of data collection, the TBM remain constant over the temperature range of this study. However, as seen in Figure 12 the 2μm TBM of pyroxenes vary as a function of temperature. The orthopyroxenes (PYX02 and PYX08) 2μm TBM shift to <u>longer</u> wavelengths while the clinopyroxene (PYX07) 2μm TBM shifts to <u>shorter</u> wavelengths as temperature increases. The spectra of the basaltic assemblage (PYX09) show two distinct bands at low temperatures which become one asymmetric band at higher temperatures.

Hazen <u>et al</u>., (1978) discuss the information gained about the crystal structure by the separation of the 1- and 2μm bands in pyroxenes.

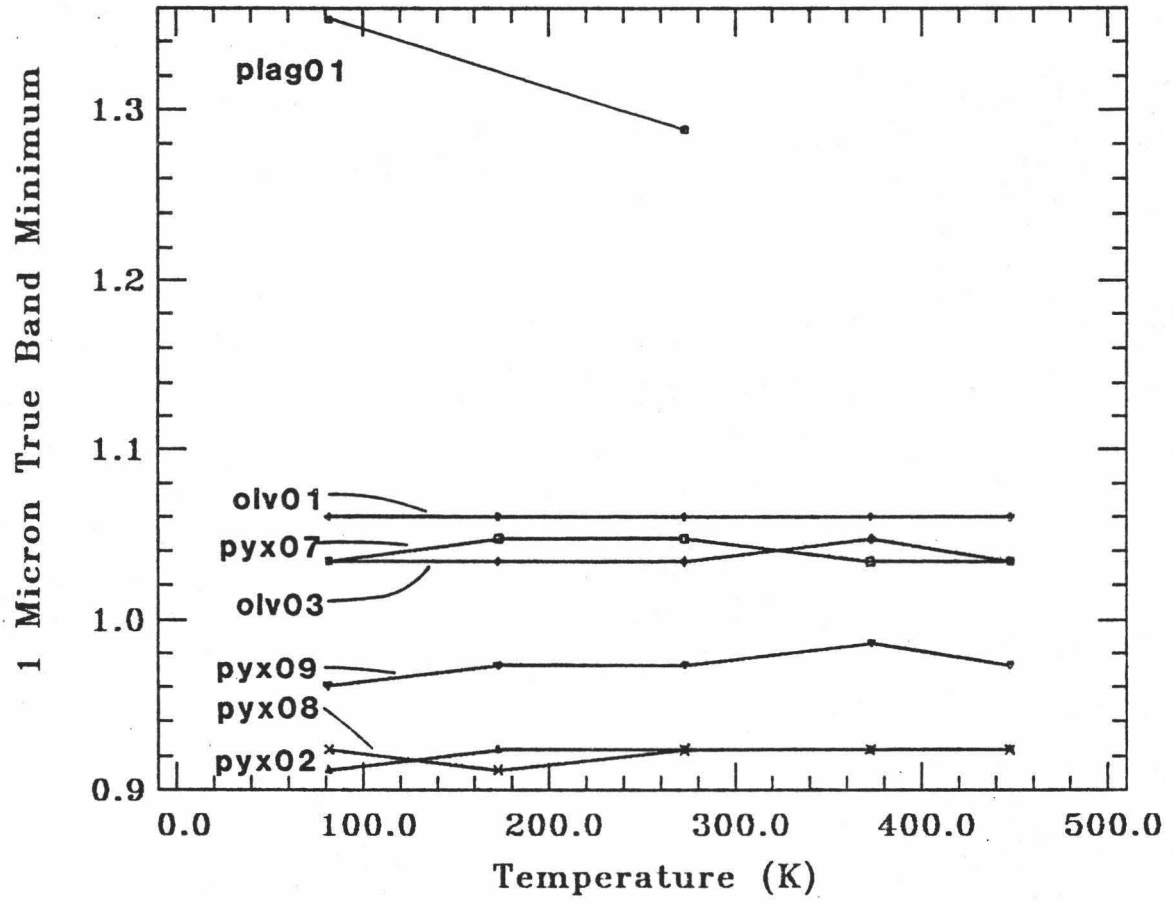

Figure 11. Effects of temperature on the 1μm true band minimum for all minerals of this study.

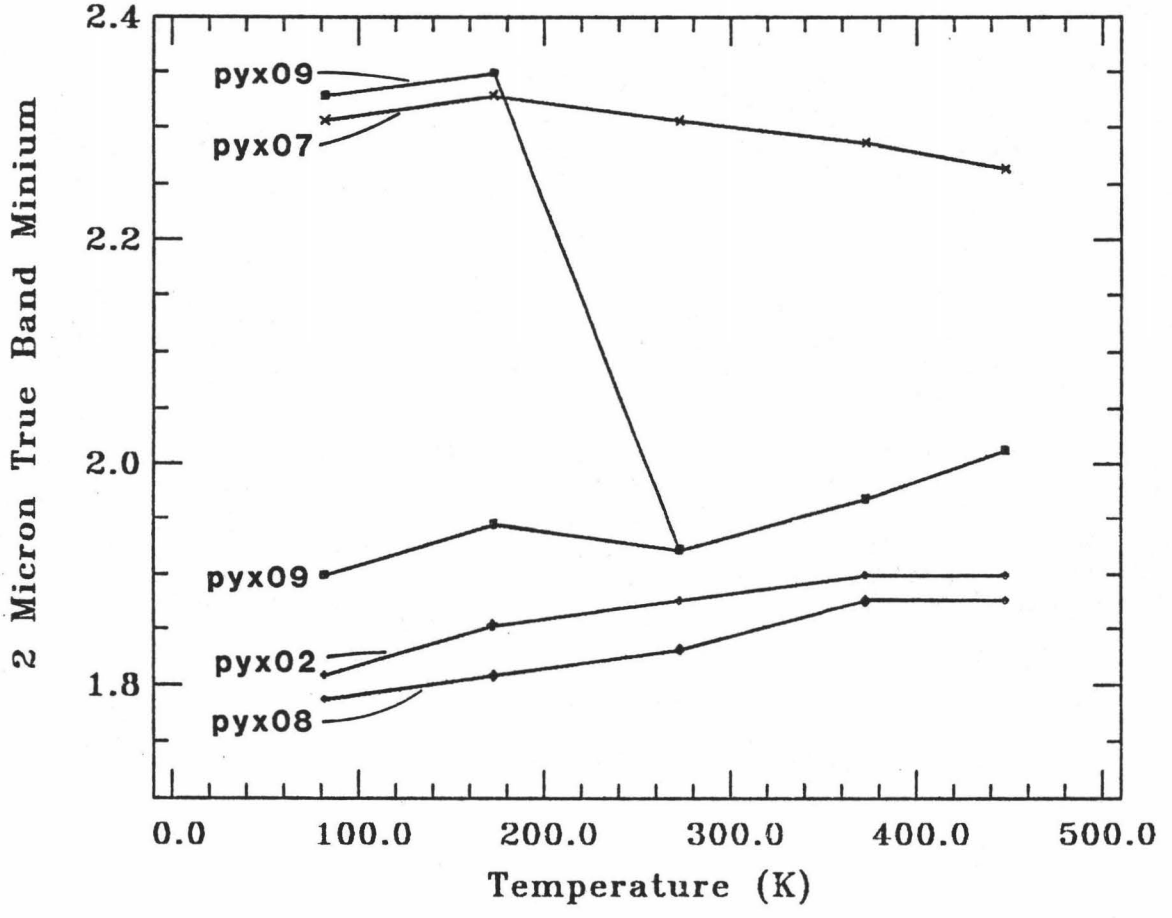

Figure 12. Effects of temperature on the 2μm true band minimum for all minerals of this study which have a 2μm band.

Table 2. Splitting Energy of 1 and 2μm Bands in Pyroxenes

T(K)	1 micron(cm^{-1})	2 micron(cm^{-1})	splitting(cm^{-1})†
PYX02			
82	10822	5531	5291
173	10822	5397	5425
273	10822	5330	5492
373	10822	5266	5556
458	10822	5266	5556
PYX08			
78	10822	5596	5226
173	10822	5531	5291
273	10822	5461	5361
373	10822	5330	5492
458	10822	5330	5492
PYX07			
83	9671	4336	5335
173	9671	4296	5375
273	9671	4336	5335
373	9671	4374	5297
458	9671	4417	5254

† errors are limited by the channel-to-channel differences in the 1μm region and are $\pm 120 cm^{-1}$.

In an octahedral environment ferrous iron, (d^6) configuration, has three lower energy (t_{2g}) and two higher energy (e_g) levels. In pyroxenes the 1μm band is a result of the transition from the lowest t_{2g} level to the higher e_g level, whereas the 2μm band is due to the transition from the lowest t_{2g} level to the lower e_g level (Goldman and Rossman, 1977). The energy difference between the 1 and 2μm bands is therefore, equal to the splitting energy of the two e_g levels of Fe^{2+} in the distorted M(2) site. The greater the splitting energy the greater the distortion of the M(2) site. Table 2 lists the splitting energy as a function of temperature for PYX02, PYX08, and PYX07. Thus, as temperature increases the splitting energy of the orthopyroxenes increases, implying the M(2) site is becoming more distorted. However, the clinopyroxene splitting energy decreases with increasing temperature, implying the M(2) site is becoming less distorted. An interesting effect of the site becoming more symmetric is that the crystal field bands should become less intense due to the Laporte selection rule. Close inspection of Figure 8 (Chapter 3) shows that the 2μm band of PYX07 becomes less intense with increasing temperature in agreement with these considerations. These differing trends in the 2μm band of the pyroxenes also agree with the conclusions reached by Smyth (1973) based on high temperature X-ray studies which show that with increasing temperature, the clinopyroxene primitive monoclinic structure gains symmetry by straightening the silicate chains so that they become crystallographically equivalent. However, in the orthopyroxene no such displacement to gain symmetry is possible, and straightening of the silicate chains proceeds much more slowly than in clinopyroxene (Smyth, 1973).

Table 3. Slopes, Intercepts, and Statistical Error Data for Pyroxene 2μm TBM

PYX02					
corr. coeff.	std dev. residuals	slope	uncertainty (95% level)	intercept	uncertainty (95% level)
0.948	7.5×10^{-3}	1.29×10^{-4}	4.92×10^{-5}	0.589	1.49×10^{-2}
PYX08					
0.977	5.3×10^{-3}	1.40×10^{-4}	3.44×10^{-5}	0.569	1.04×10^{-2}
PYX07					
0.829	6.8×10^{-3}	-5.80×10^{-5}	4.42×10^{-5}	.848	1.34×10^{-2}

A linear, least squares routine presented by Mortimer (1981) has been adapted in an attempt to quantify the pyroxene 2μm TBM position, as a function of temperature. The discrete values of PYX02, PYX07, and PYX08 TBM were used as input. All samples are best described by the equation:

$$\ln(2\mu m\ TBM) = mT + b \qquad \text{(eqn 1)}$$

where T is the temperature in Kelvin, m is the slope, and b is the intercept when T=0K. Table 3 lists values of slope and intercepts for these minerals, as well as, statistical parameters. It is reassuring that both orthopyroxenes result in similar values which are significantly different than those for clinopyroxene. Caution is urged in applying these results to wide ranges of pyroxene composition since they are based on a very limited data set.

At a second level of analysis, a non-linear, least squares, Gaussian fitting analysis, based on an algorithm presented by Kaper et. al., (1966) and discussed by Farr et al., (1980) (the program has since been rewritten to simultaneously fit up to twenty Gaussian functions), was performed on a limited subset (OLV01, PYX02, and PYX07) of the minerals over a limited wavelength region (the 1μm region). It was hoped this analysis would uniquely characterize both positions and symmetries of absorption bands as a function of temperature. The specific approach was to remove a straight line continuum for each temperature and then fit Gaussians using the natural logarithm of the reflectance relative to the continuum and inverse wavelengths, thus making the analysis of the data proportional to the absorption coefficient of the mineral as a function of energy (Clark and Roush, 1984).

The PYX02 82K data was first to be analyzed and the absorption appeared to be saturated when plotted as ln(r) versus $1/\lambda$, which could lead to spurious Gaussians needed to describe the feature. Fortunately, a data set for the same pyroxene, at the same temperature, but of a finer grain size (<45μm) existed, and when plotted as described above it did not appear saturated. One, two, and three Gaussians were used to analyze this finer grain size data and since only the two Gaussian analysis converged to a solution, it was felt that two Gaussians uniquely described the data. Subsequently, no additional Gaussians were needed to fit the larger grain size data, and resultant fits and residuals are shown in Figures 13a through 13e. Figure 14 is a plot of individual Gaussian parameters (centers, heights, and widths) as a function of temperature. Individual Gaussian centers move to longer wavelengths and widths increase as temperature increases. The depth of the shorter wavelength Gaussian (band 2) increases while the longer wavelength Gaussian (band 1) depth decreases as temperature increases. However, all these variations in individual parameters do not effect the combined Gaussian envelope TBM as seen in Figure 15.

It is important to assess what physical processes these individual Gaussians may represent. There are five distinct processes which could result in resolution of two individual absorption bands in the 1μm of the orthopyroxene spectra: 1)both bands represent electronic transitions due to Fe^{2+} located in the orthopyroxene M(2) crystallographic site; 2)the individual bands represent electronic transitions due to Fe^{2+} located in both the orthopyroxene M(1) and M(2) crystallographic sites; 3)vibronic coupling results in allowing a second, otherwise forbidden, electronic transition due to Fe^{2+} in the orthopyroxene M(2) crystallographic site; 4)the individual bands represent two discrete

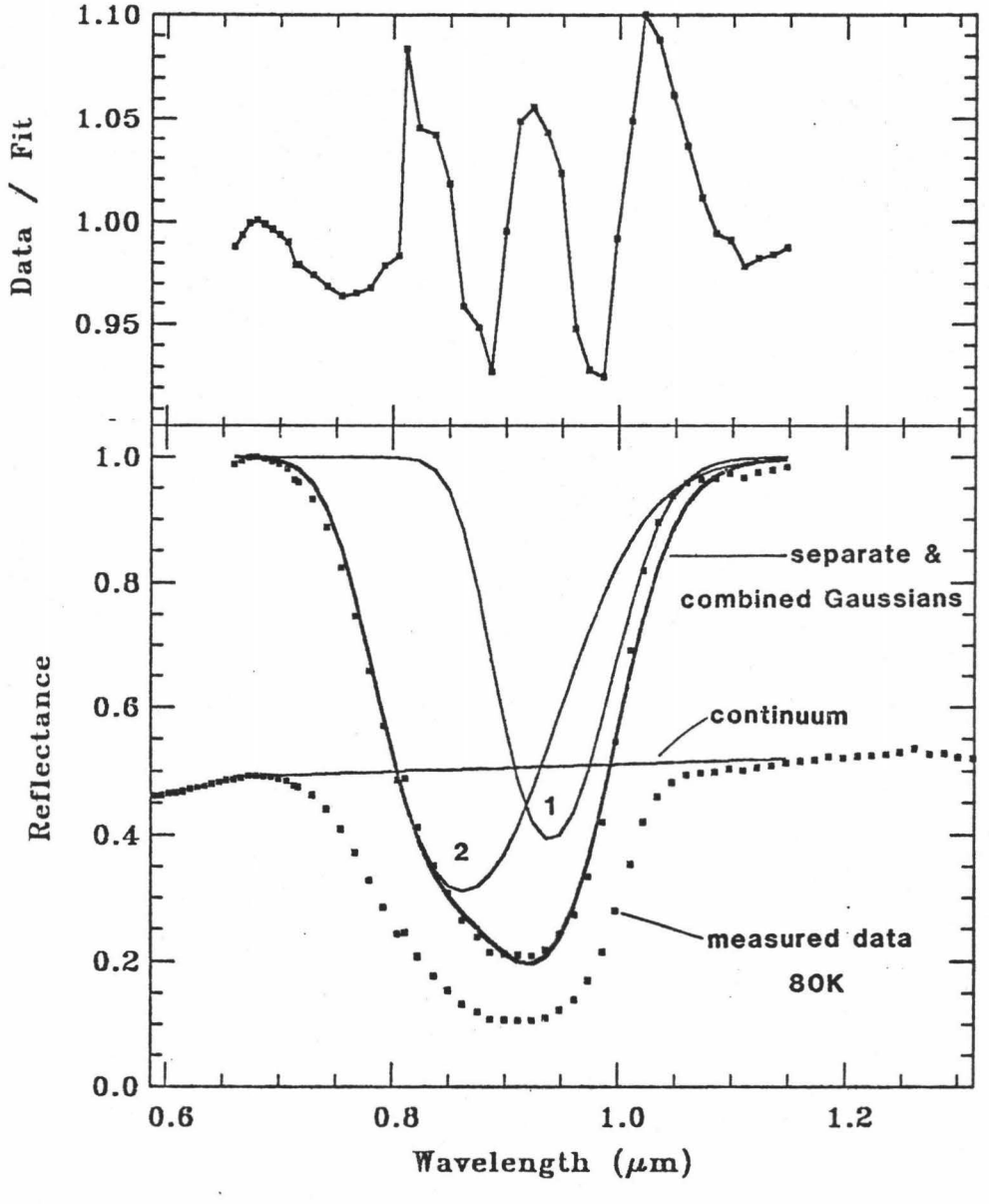

Figure 13a. Deconvoluted Gaussian bands and residuals for PYX02 spectrum at ≈80K.

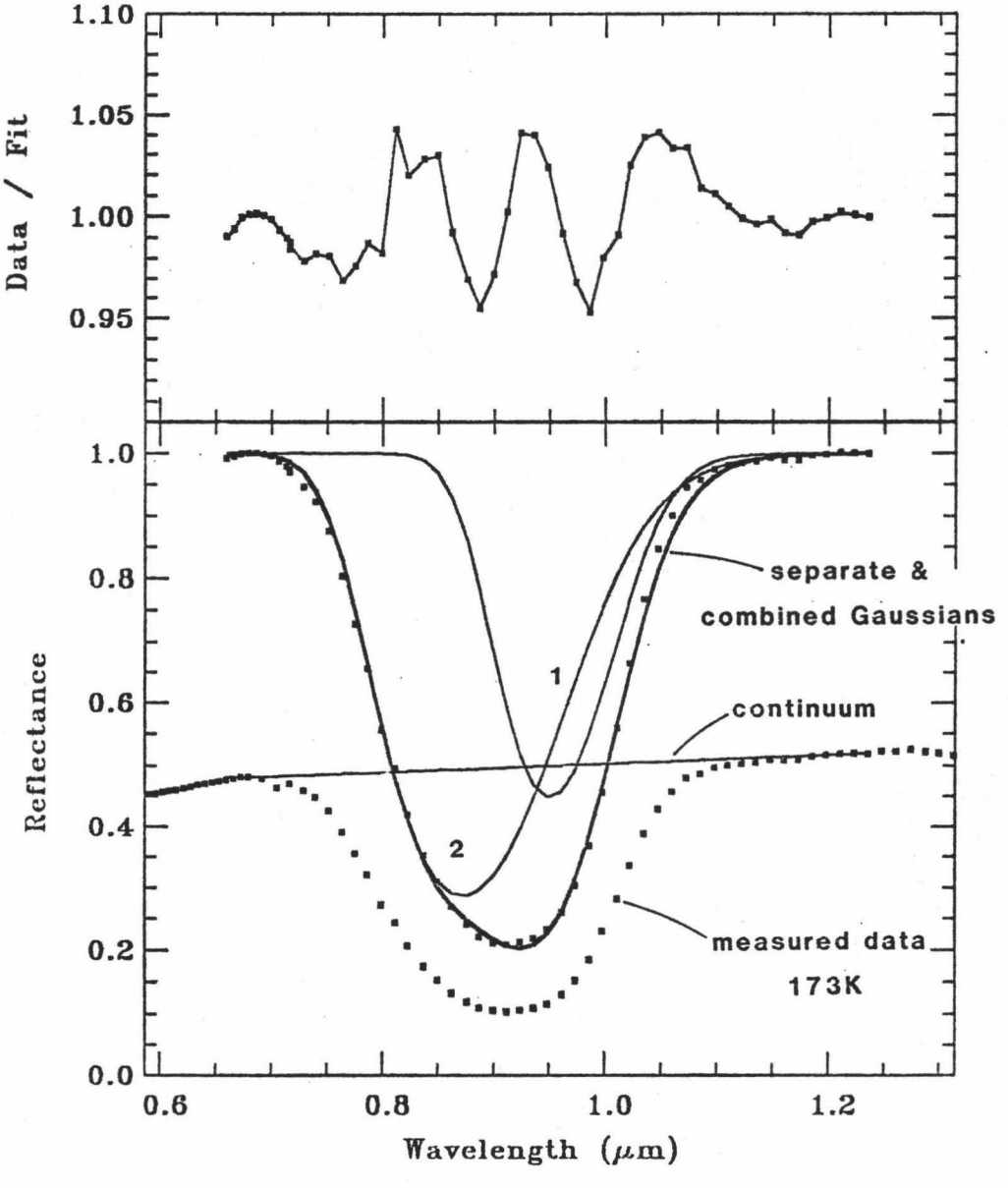

Figure 13b. Deconvoluted Gaussian bands and residuals for PYX02 spectrum at 173K.

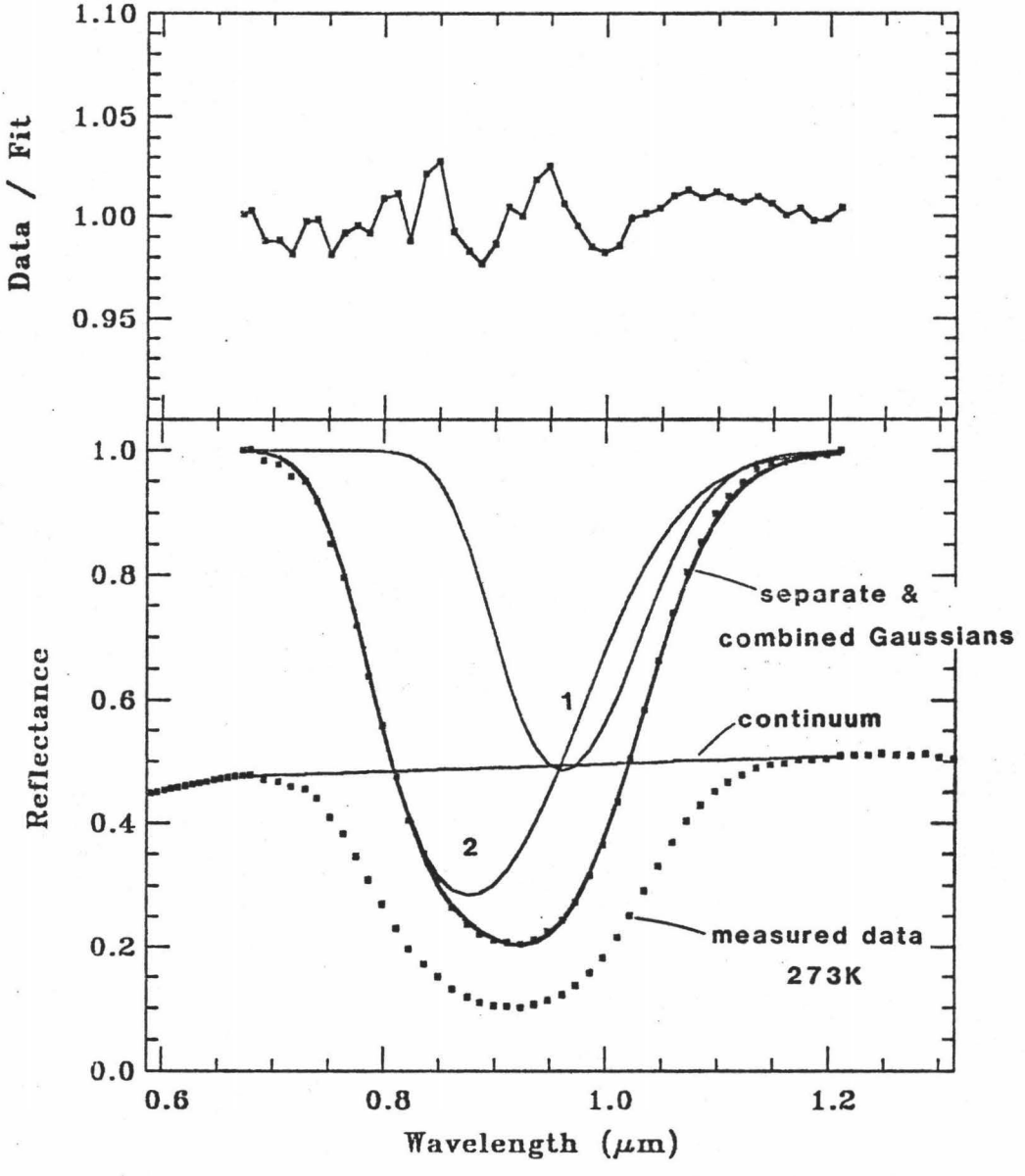

Figure 13c. Deconvoluted Gaussian bands and residuals for PYX02 spectrum at 273K.

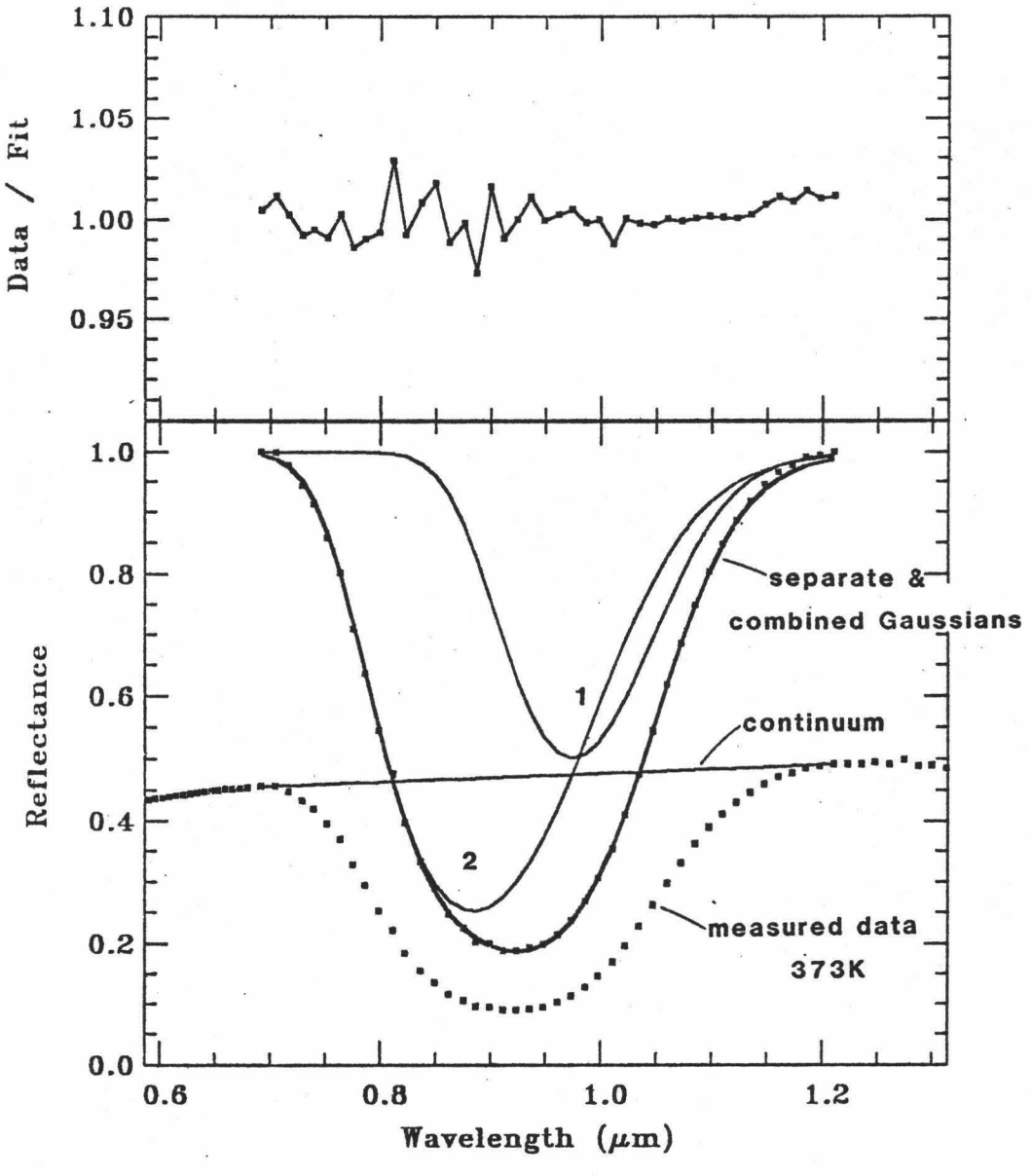

Figure 13d. Deconvoluted Gaussian bands and residuals for PYX02 spectrum at 373K.

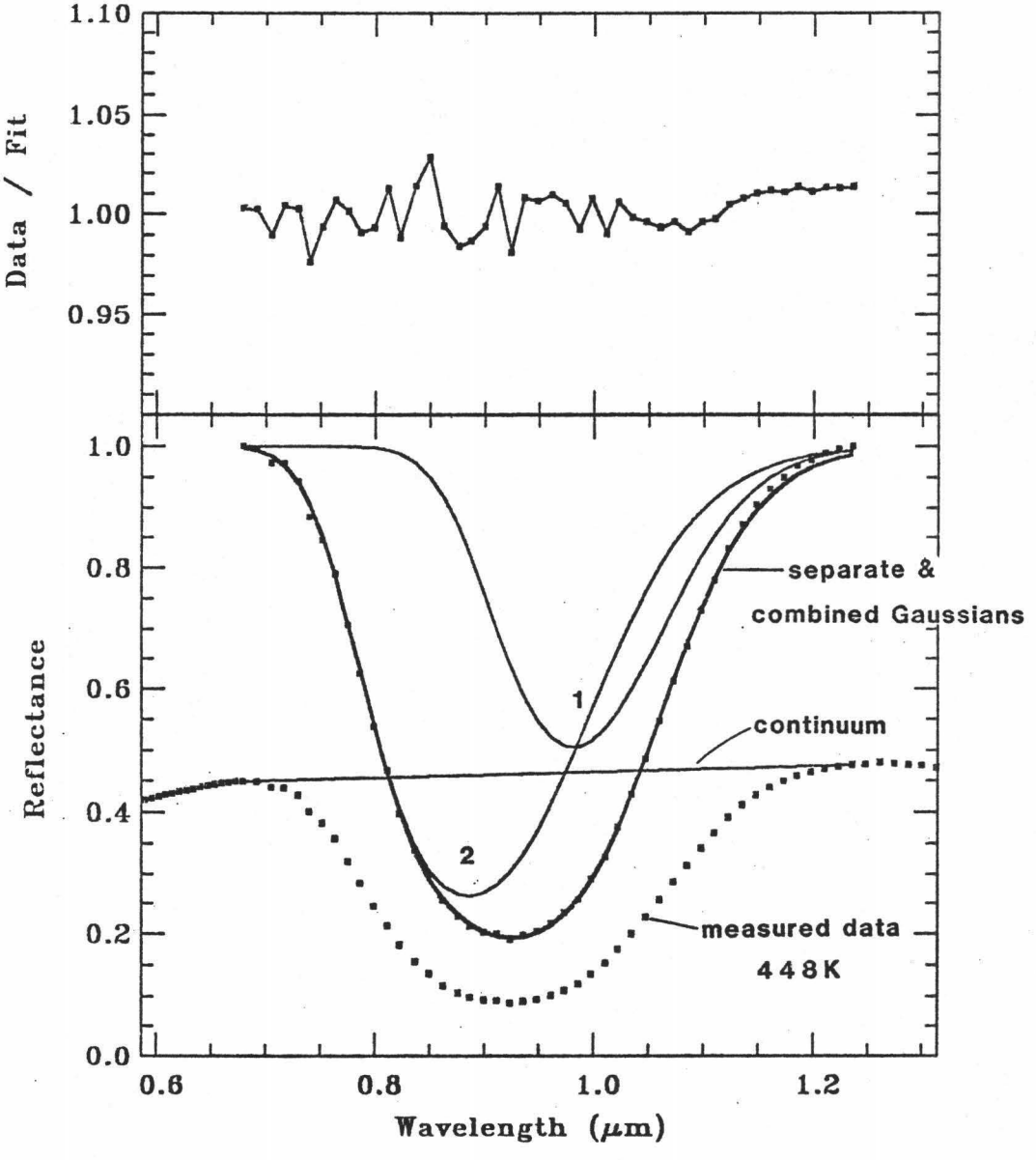

Figure 13e. Deconvoluted Gaussian bands and residuals for PYX02 spectrum at 448K.

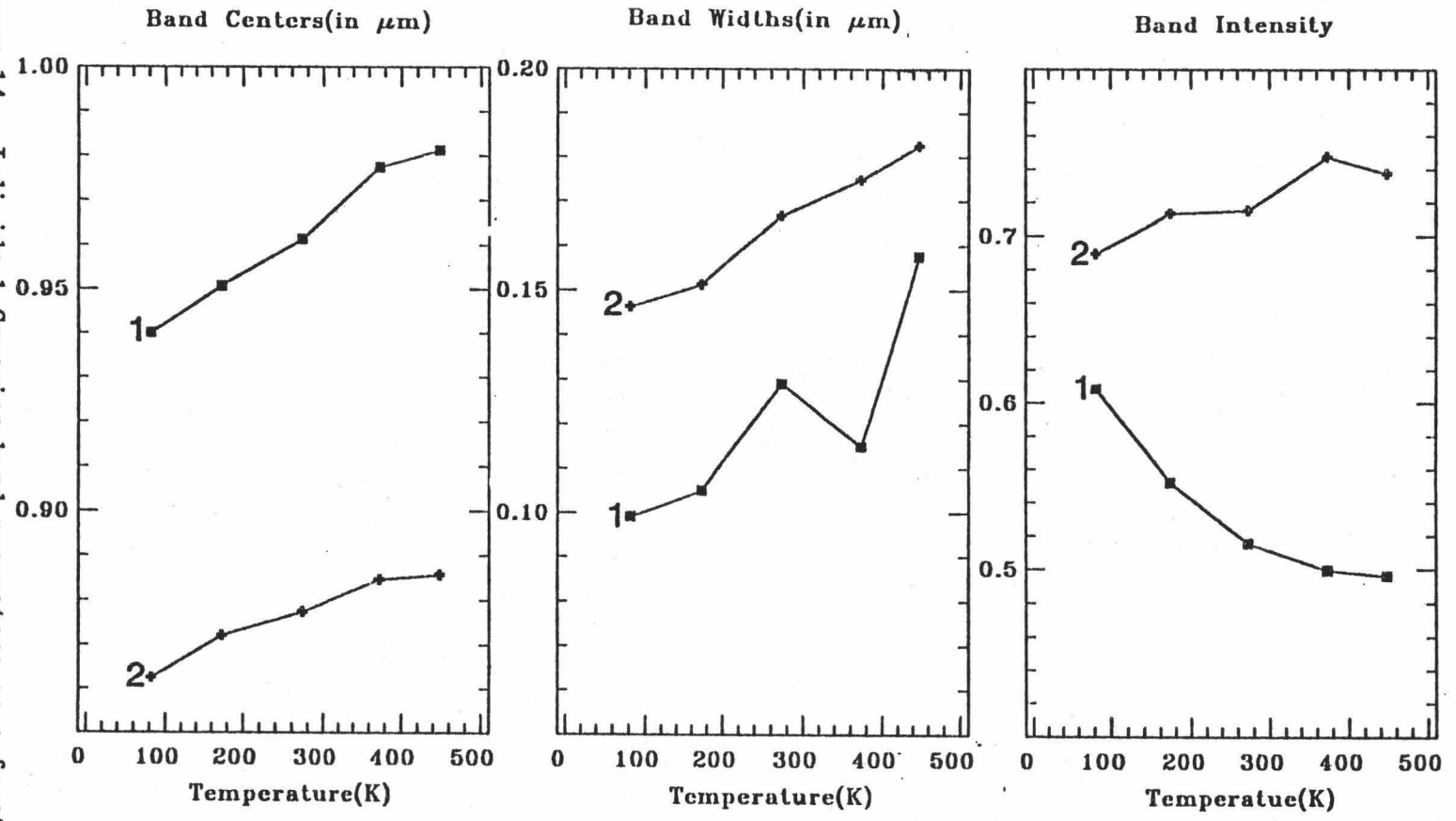

Figure 14. Individual Gaussian band parameters as a function of temperature for PYX02.

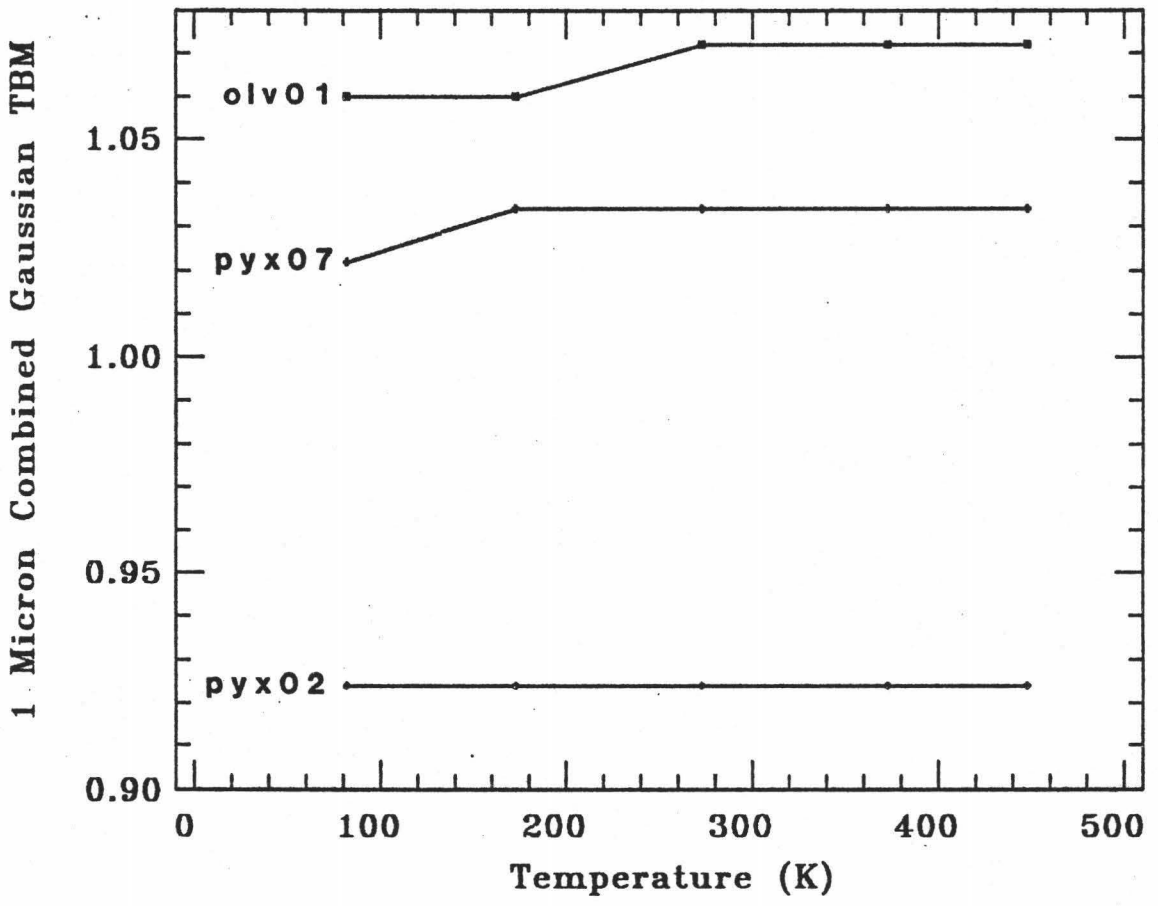

Figure 15. Combined Gaussian envelope true band minimum of PYX02, PYX07, and OLV01.

mineral phases; and 5) the nature of these absorptions are intrinsically asymmetric but can be characterized by two Gaussians. I will address each of these possibilities and discuss how individual Gaussian parameters would be expected to vary as a function of temperature for each process.

The high temperature X-ray studies of orthopyroxene (Smyth, 1973; Sueno et al., 1972) show that increasing temperature would result in differential expansion of the M(2) crystallographic site and an increase in individual metal-oxygen distances. The crystal field splitting energy is approximately inversely proportional to the fifth power of the metal-oxygen distances (Burns, 1970), and if X-ray diffraction data existed for this mineral at the same temperature it might be possible to put even greater constraints on this relationship. In any case, increasing temperature would reduce the energy required for a given electronic transition and result in band centers shifting to longer wavelengths. This is indeed the trend seen in Figure 14. Thermal vibrations of the metal ion about the center of the crystallographic site would increase with increasing temperature and result in broadening an absorption band (Burns, 1970). A trend also seen in Figure 14. The intensity of an absorption band is directly related to the probability that a given transition will occur, as such increasing temperature could act to increase or decrease the probability so it is not straight forward to predict how the intensity of a specific transition will be effected by temperature. Goldman and Rossman (1977) identified three crystal field transitions due to Fe^{2+} in the orthopyroxene M(2) site and their schematic energy level diagram is shown in Figure 16. Applying their analysis to the individual Gaussians of this study, the highest energy transition ($^5A_1 \rightarrow {}^5A_1$) would correspond to Gaussian 2 in

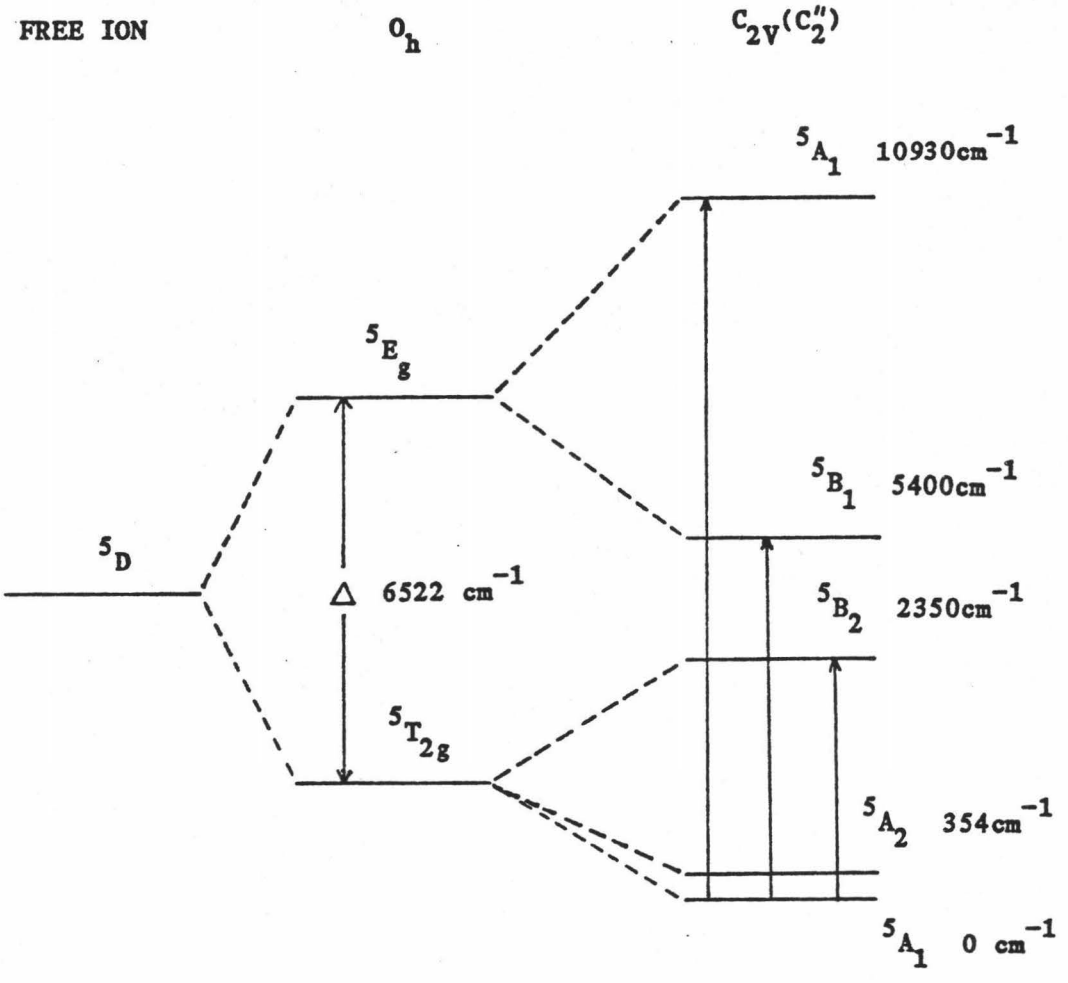

Figure 16. Schematic energy level diagram for orthopyroxene M(2) crystal site (from Goldman and Rossman, 1977).

Figure 14, however, this band does not occur at the proper wavelength to correspond directly to the $^5A_1 \rightarrow {}^5A_1$ transition. The only other possible band in this wavelength region to correspond to Gaussian 1 of Figure 14 would be the $^5A_2 \rightarrow {}^5A_1$ transition. Since this is not the ground state it should have a band intensity much less than the $^5A_1 \rightarrow {}^5A_1$ transition, however this is not the case as seen in Figure 14 since both bands have similar intensity. In fact, the Gaussian intensity variation as a function of temperature would require the probability of Gaussian 1 to decrease while Gaussian 2 increased. In light of these considerations, it is inconsistent to attribute the two individual Gaussian bands to electronic transitions due to Fe^{2+} located solely in the M(2) crystallographic site of orthopyroxene.

If the individual Gaussians represent electronic transitions due to Fe^{2+} located in both the M(1) and M(2) crystallographic sites of orthopyroxene there are three bands, located at ≈.89 (M(1)), ≈.91 (M(2)), and 1.15 (M(1))μm, which could potentially be resolved (Rossman, 1980). The Gaussians are located at .86-.885μm and .94-.98μm Assuming Gaussian 2 corresponds to the .89μm M(1) band and Gaussian 1 corresponds to a mixture of the .91μm M(2) and 1.15μm M(1) bands, both should shift to longer wavelengths and increase in width as temperature increases based on the information presented in the high temperature X-ray structural studies.

In this case, the intensity of Gaussian 2 could increase while the intensity of Gaussian 1 decrease because of an order-disorder mechanism which prefentially fills the M(1) sites with Fe^{2+} relative to the M(2) site at higher temperatures (Smyth, 1973). This intensity trend is seen in the Gaussian analysis, however, Bancroft et al., (1967) show that little, if any, Fe^{2+} occupies the M(1) site in the Bamble

bronzite. Also, the order-disorder mechanism invoked above does not occur until temperatures exceed 500°C and the time scale of these measurements is much too short for this mechanism to be active (Smyth, 1973). These two considerations imply that an interpretation relating the two resolved Gaussians to electronic transitions due to Fe^{2+} in both the M(1) and M(2) crystallographic sites of orthopyroxene is premature and inconclusive.

Vibronic coupling is a mechanism by which an electronic transition becomes allowed, or is more probable, due to the simultaneous excitation of a vibrational mode (Cotton, 1963). The fundamental vibrational modes for pyroxenes occur between ≈9 and ≈11μm (Lyon and Green, 1975) so any contributions near 1μm will be due to overtones and combinations of the normal modes. In fact, in this region higher order overtones (8th, 9th or 10th) and combinations would have to be invoked for the vibronic coupling mechanism and thus would have small intensities (a decrease in intensity of ≈30% for each overtone (Clark, pers. comm., 1984). No indication is seen in the spectra of absorptions due to lower order overtones (3rd or 4th) and combinations out to 2.5μm. Infrared spectroscopy of two enstatites (Launer, 1952) in the 2 to 15μm region show no sharp features from 2 to ≈6μm. As temperature increased, one would expect the intensity of the vibronically activated absorption to increase, but still remain much less that of the electronically allowed transition. Since individual Gaussian intensities are similar, and the intensity of the smaller Gaussian (band 1) actually decreases with increasing temperature, it is difficult to invoke vibronic coupling as a viable mechanism resulting in two individual absorption bands. However, this conclusion is based on the limited wavelength region of this study and to properly address this question,

a study concerning the variation of the fundamental vibrational modes as a function of temperature, utilizing mid-infrared or Raman spectroscopic techniques, would be necessary.

This study assumes a homogeneous composition for all of the minerals. If this is not the case, then resolution of two discrete absorptions due to two mineral phases may be possible. Several studies (Mori and Takeda, 1980; Takeda, 1979; and Nord, 1978) have identified localized regions of compositional hetrogeneity on the scale of a few to hundreds of angstroms in chemically homogeneous orthopyroxenes. Nord (1980) has identified high calcium zones (up to 25 mole%) in orthopyroxenes from both Bamble, Norway and Jackson County, North Carolina which make up ≈6% of the entire sample volume. These localized Ca-rich zones have a crystal structure characteristic of pigeonite. Thus, potentially two individual Gaussians may represent these discrete components. The short wavelength band would correspond to the (orthopyroxene) component while the long wavelength band to a (pigeonite) component. From crystal field considerations one would expect both bands to behave similarly with increasing temperature. However, the individual Gaussian intensities have opposing trends which would require a solid state migration of Fe^{2+} from the pigeonite to orthopyroxene component which is unlikely for the temperature range of this study. Also, the intensity of Gaussian 1 is much greater than would be expected for this Gaussian being due to only 6% of the entire sample volume since pigeonite has an absorption coefficient which is about a factor of two less than that for orthopyroxene (Burns et al., 1975).

Polarized transmission spectra of orthopyroxene (Burns, 1970; Goldman and Rossman, 1977) also appear asymmetric in each orientation and it may be that these absorptions are intrinsically so. The

Gaussian fitting routine here does not have the capability to evaluate skewed Gaussians and may tend to resolve these as two bands. I believe it would be premature to conclude anything concerning the intrinsic nature of these absorptions without conducting a broader approach with Gaussian analysis.

From these considerations, it is apparently difficult to assign the two individual Gaussians to specific chemical, electronic, or vibrational mechanisms. Whatever mechanism to be invoked for changes in the spectral properties of orthopyroxene as a function of temperature must address two facts: 1)the overall absorption band minimum does not change, and 2)the long wavelength side of this band shows an increase in absorption with increasing temperature. However, the Gaussian analysis presented does provide a unique method for characterizing the 1μm absorption feature of orthopyroxene for a wide range of band symmetries and as such, may be useful for deconvolution of mineral mixtures which contain orthopyroxene as a component.

A similar approach was taken with the PYX07 data, except that no finer grain size measurements were available. Again, analyses with one, two, and three Gaussians were performed. In this case, both two and three Gaussian fits converged for all temperatures except for the highest, where three Gaussians failed to converge. A comparison of Figures 17 and 18 show that the two Gaussian analysis of this data yields a more consistent trend of individual parameters than a three Gaussian analysis, for this reason, and the fact that three Gaussian analysis does not converge at the highest temperature, a two Gaussian analysis is preferred for characterizing the reflectance spectra of the 1μm region of PYX07 as a function of temperature. Figures 19a through 19e shows the resultant Gaussian fits and residuals for the two

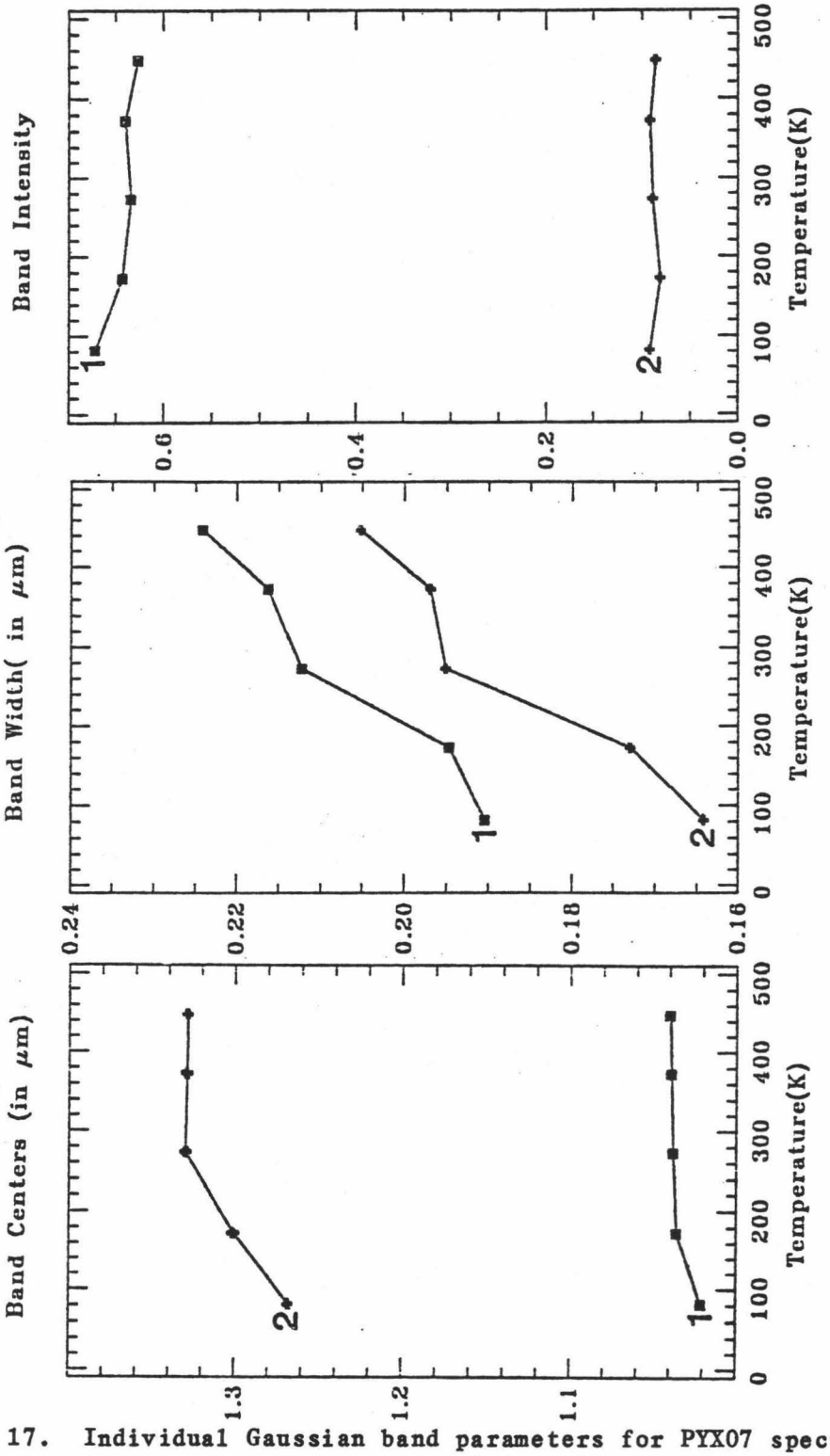

Figure 17. Individual Gaussian band parameters for PYX07 spectra at various temperatures using a 2 Gaussian anaylysis.

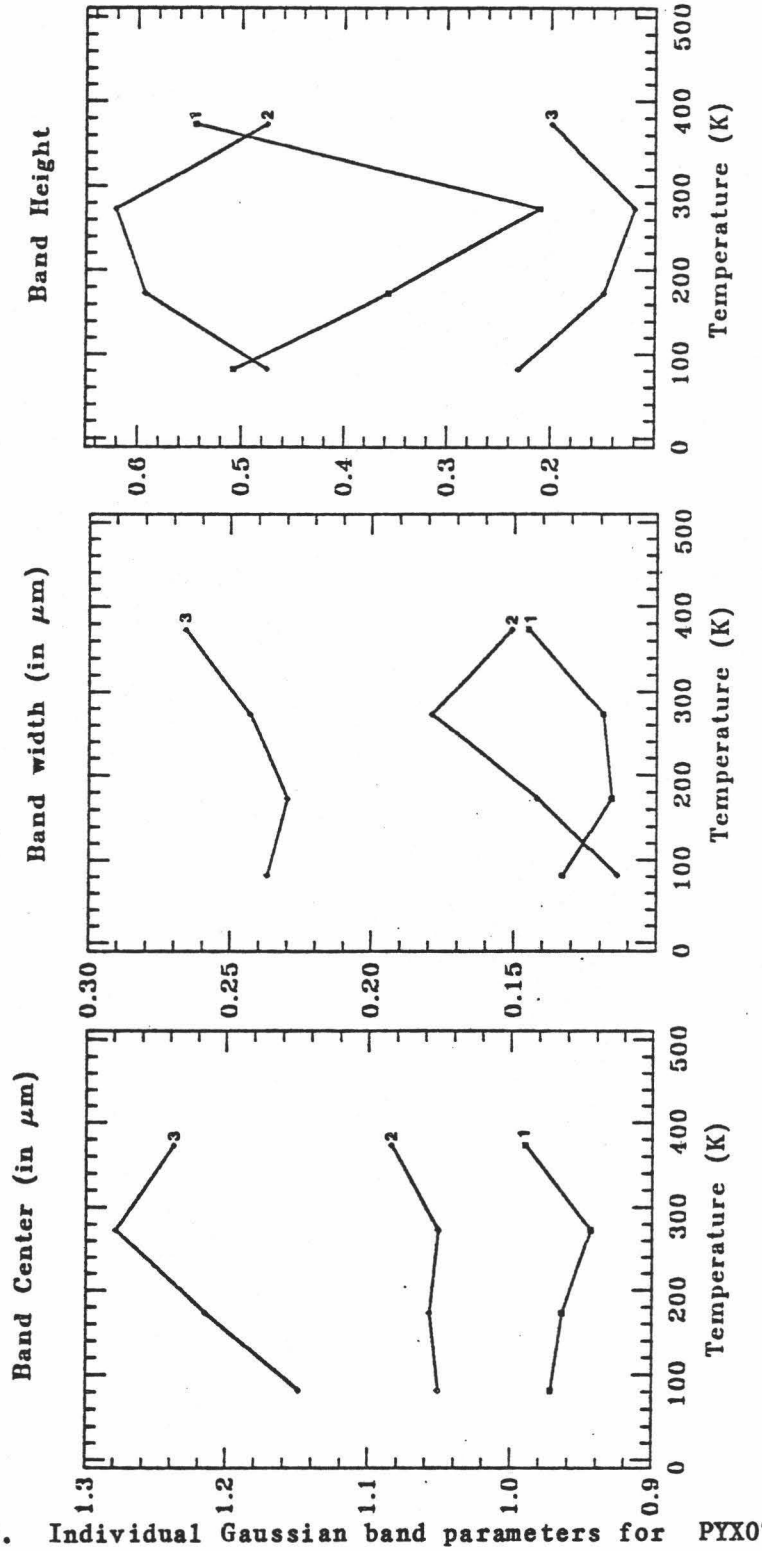

Figure 18. Individual Gaussian band parameters for PYX07 spectra at various temperatures using a 3 Gaussian analysis.

Gaussian analysis. Figure 17 shows that individual Gaussian centers move to longer wavelengths and widths increase with increasing temperature. Both Gaussian heights decrease with increasing temperature. However, these variations in individual parameters do not effect the combined Gaussian TBM as seen in Figure 15, where the difference at the lowest temperature again corresponds to a single wavelength channel and is believed insignificant, as discussed previously. The mechanisms discussed previously for orthopyroxene which could result in two individual absorptions will be discussed for the clinopyroxene.

High temperature X-ray studies for clinopyroxene (Cameron et al., 1973; Brown et al., 1972; Smyth, 1974) show that individual metal-oxygen distances of the M(1) and M(2) crystallographic sites increase at higher temperatures. If these Gaussians represent transitions due to Fe^{2+} located solely in the M(2) crystallographic site, this expansion of the metal-oxygen distances would result in band centers and widths increasing as discussed previously, and is illustrated in Figure 17. Unfortunately, there is no schematic energy level diagram as was presented for orthopyroxene. However, consideration of a generalized energy level diagram, similar to the orthopyroxene and with the energy levels held constant with respect to each other, is useful. Using this scheme, Gaussian 1 corresponds to the $^5A_1 \rightarrow {}^5A_1$ transition and Gaussian 2 would correspond to the $^5A_2 \rightarrow {}^5A_1$ transition. In this case, the relative intensities of the Gaussians are as one would expect. The decrease in intensity of these bands with increasing temperature would imply that the site is becoming more symmetric, which is in agreement with the previous discussion concerning the shifting of the 2μm TBM. The difference in the band positions would require that the seperation of the two lowest energy levels be about $2000cm^{-1}$ which is about one or

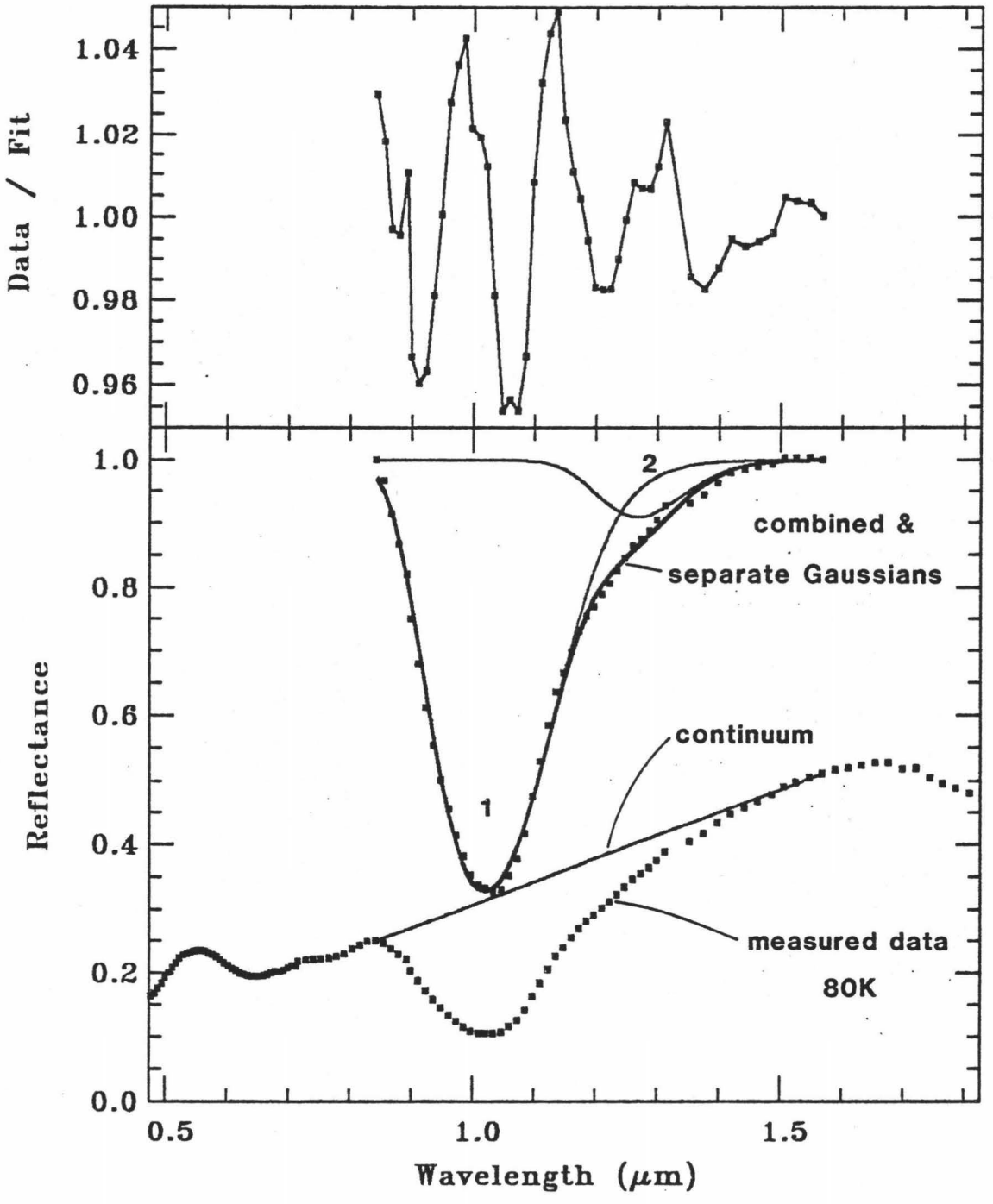

Figure 19a. Deconvoluted Gaussian bands and residuals for PYX07 spectrum at ≈80K.

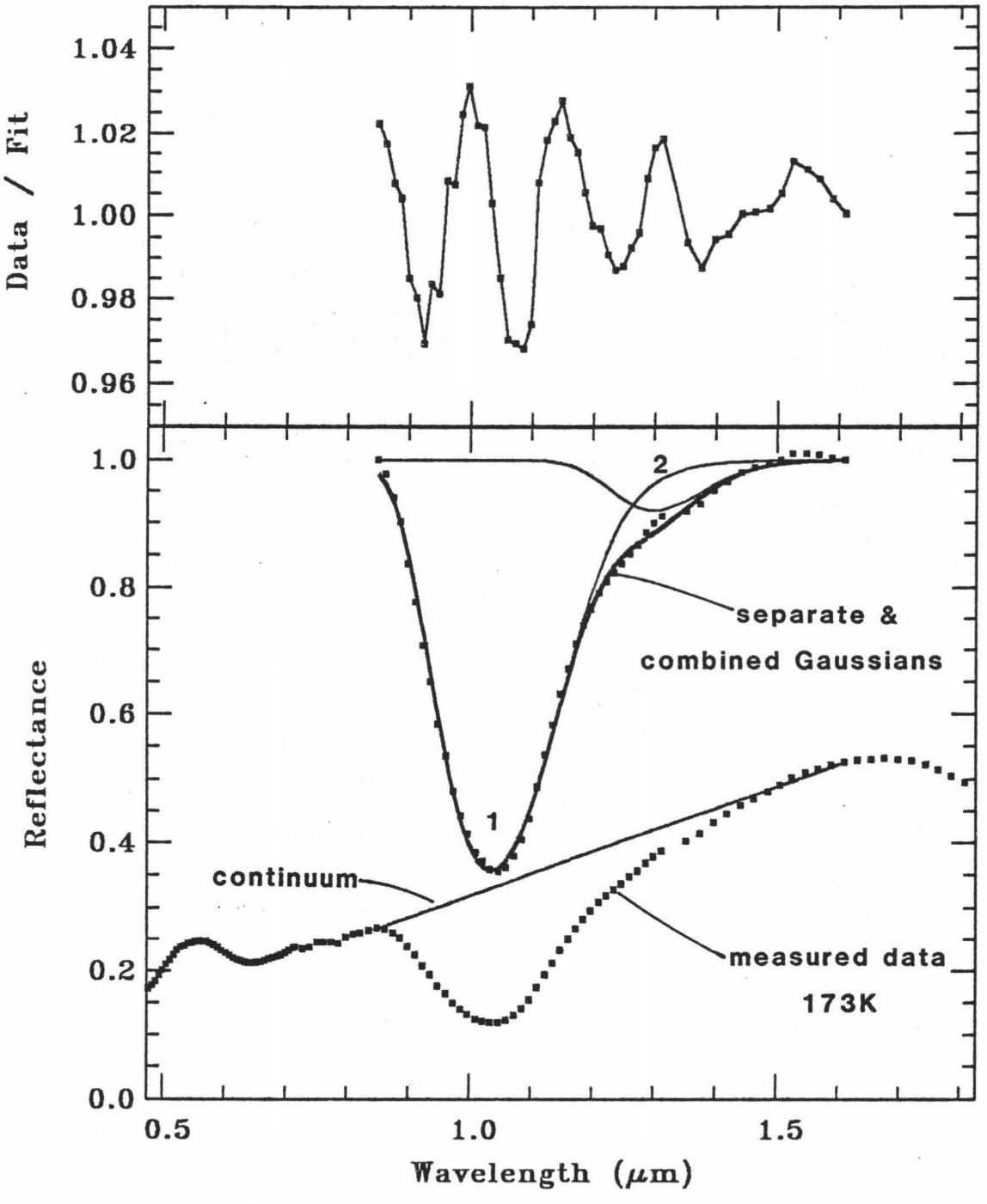

Figure 19b. Deconvoluted Gaussian bands and residuals for PYX07 spectrum at 173K.

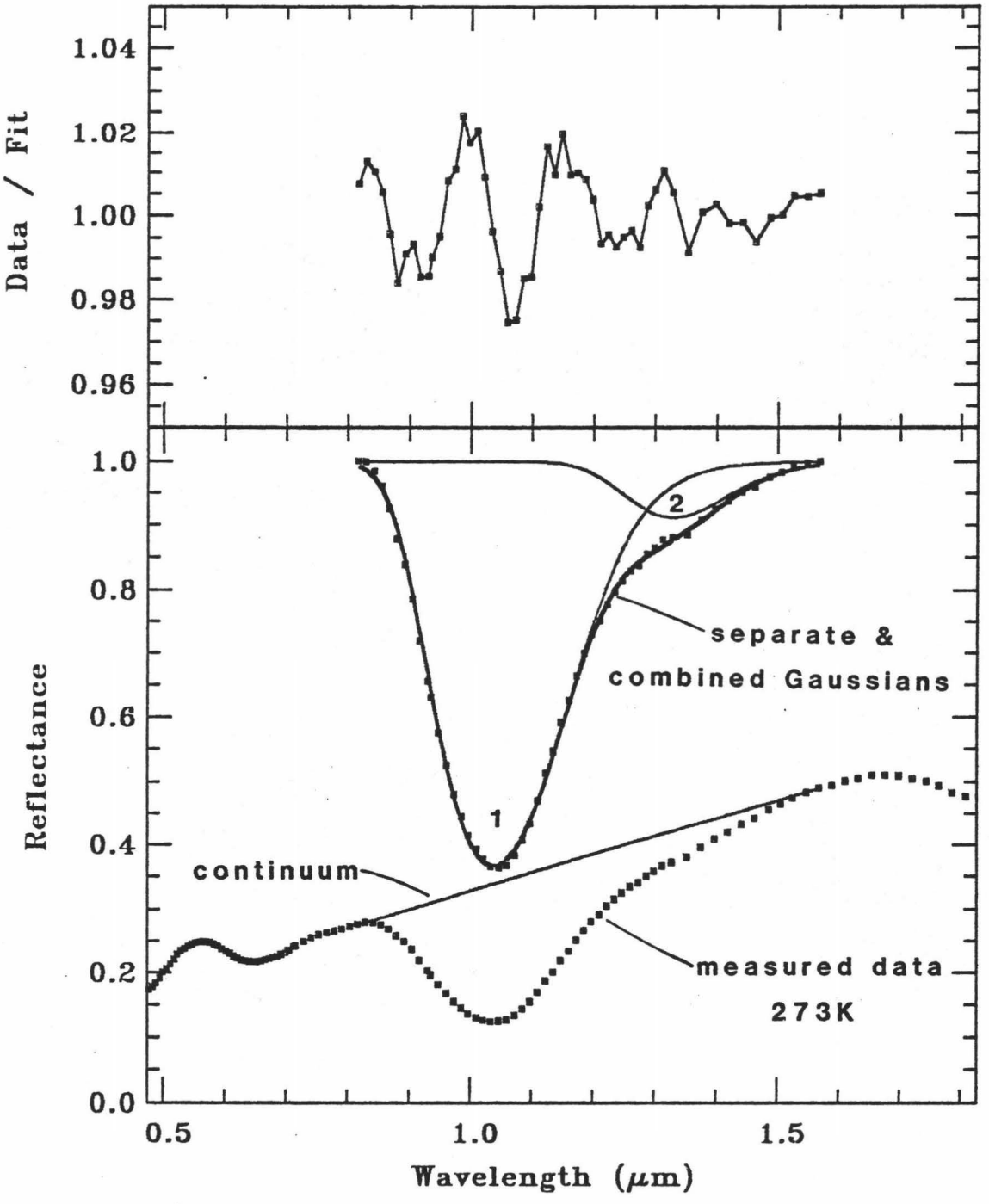

Figure 19c. Deconvoluted Gaussian bands and residuals for PYX07 spectrum at 273K.

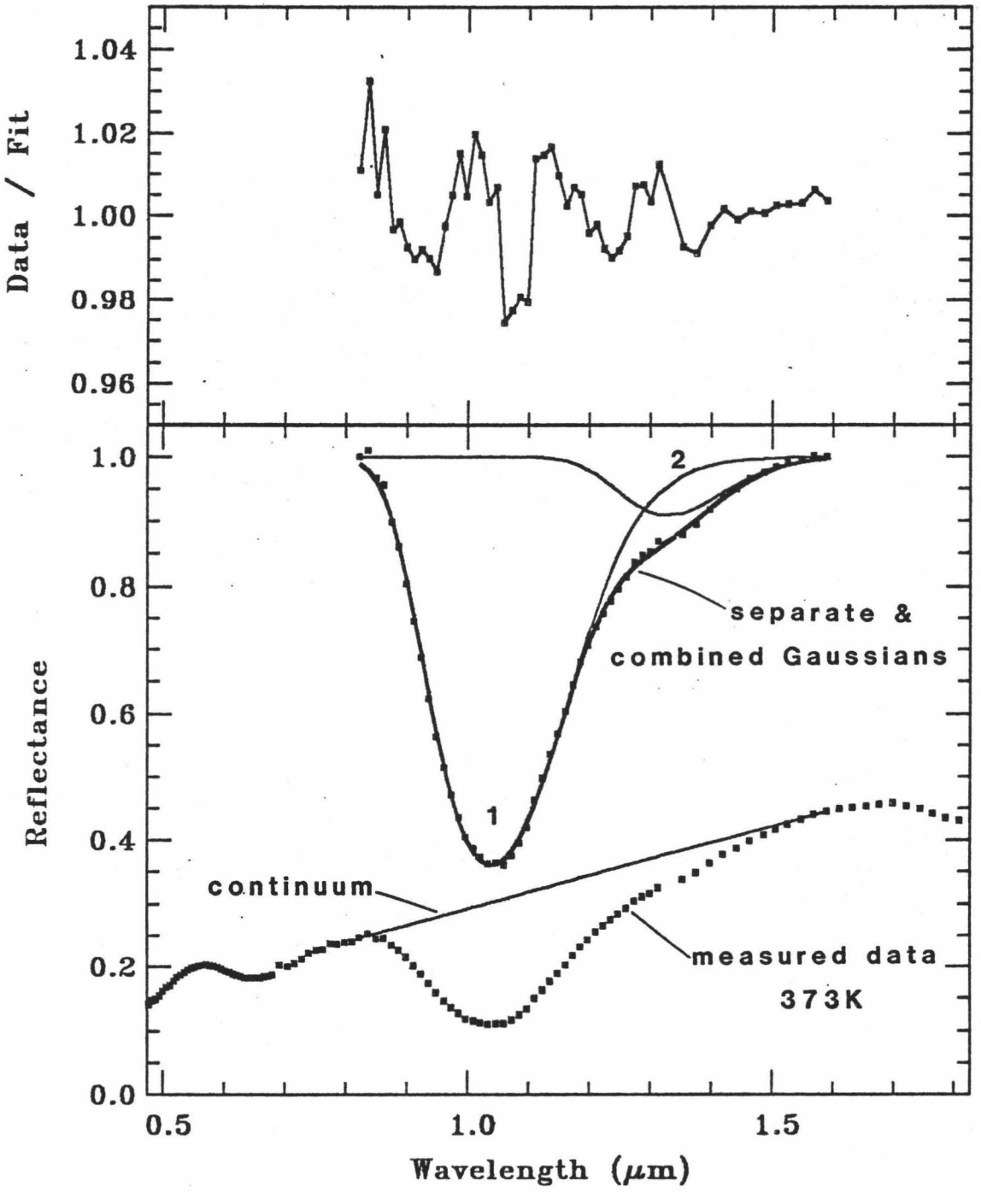

Figure 19d. Deconvoluted Gaussian bands and residuals for PYX07 spectrum at 373K.

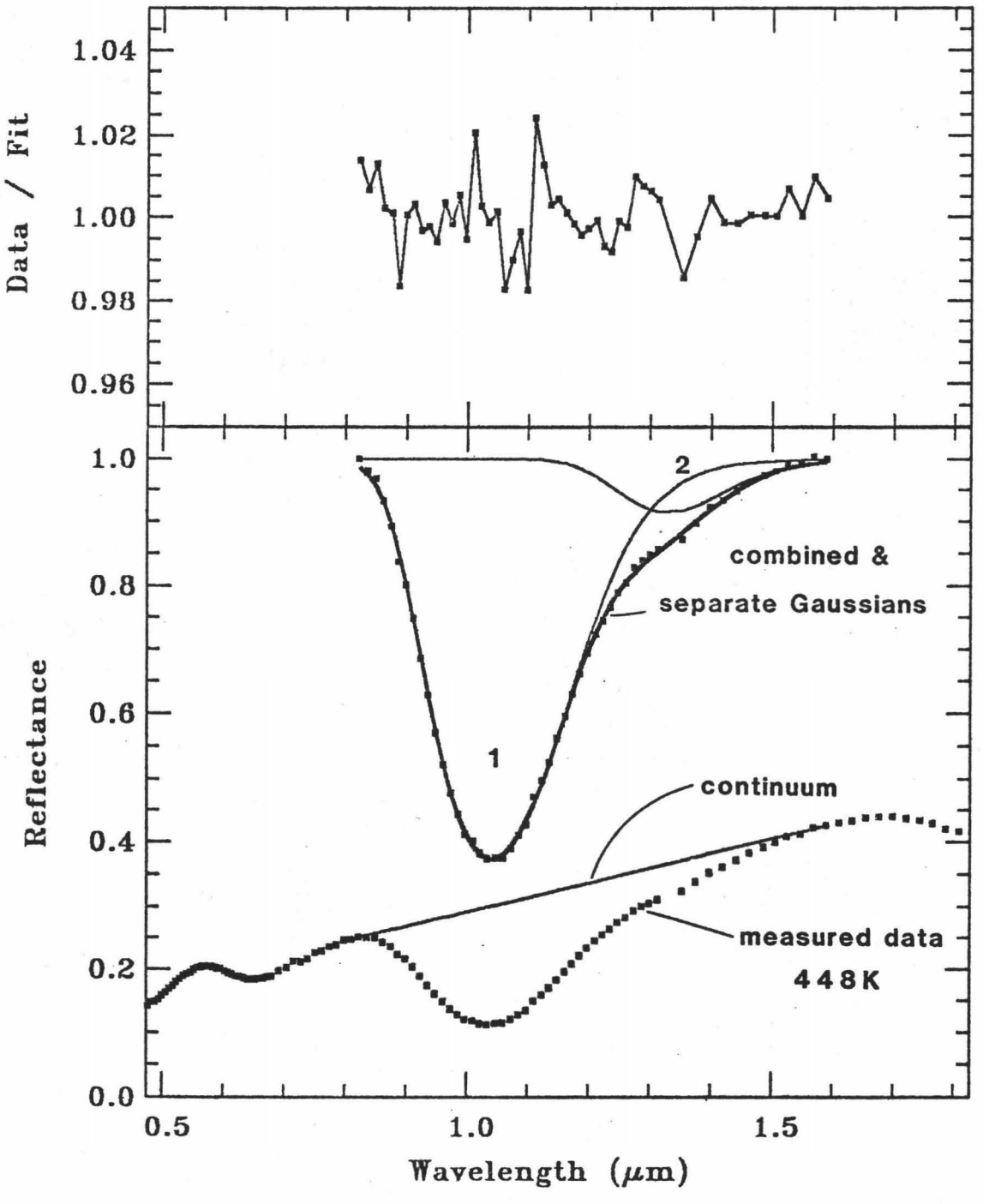

Figure 19e. Deconvoluted Gaussian bands and residuals for PYX07 spectrum at 448K.

two orders of magnitude greater than would be expected (Burns, 1970). This argues against the two individual Gaussians resulting from Fe^{2+} solely in the M(2) crystallographic site in clinopyroxene.

If the individual Gaussians represent electronic transitions due to Fe^{2+} located in both the M(1) and M(2) crystallographic site in clinopyroxene there are three bands located at ≈.97((M1)), ≈1.03(M(2)), and ≈1.20(M(1))μm, which could potentially be resolved (Rossman, 1980). Assuming the 1.02-1.04μm Gaussian (band 1) corresponds to the ≈1.03μm M(2) band, and the ≈1.26-≈1.34μm Gaussian (band 2) corresponds to the 1.20μm M(1) band, both would be expected to behave similarly as a function of temperature. This is the case for all three parameters of both Gaussians plotted in Figure 17. Thus, it appears that absorptions due to electronic transitions of Fe^{2+} located in both the M(1) and M(2) crystallographic site in clinopyroxene is a viable mechanism for resolving two individual Gaussians.

As with the orthopyroxene, vibronic coupling is a potential mechanism which would allow resolution of two seperate bands. The relative intensities of the two Gaussians are approximately as would be predicted assuming band 2 represents the vibronically activated transition (Cotton, 1963). Vibrational motion of the crystal structure is favored by increasing temperature, hence, the intensity of band 2 should increase with temperature, but Figure 17 shows the opposite trend. Again, it is difficult to envision the higher order overtones or combinations of fundamental vibrations resulting in even the low intensity of Gaussian band 2. Hunt et al., (1950) present the spectra of an augite from 2 to 16μm which has little indication of sharp overtones or combinations short of ≈4.4μm. However, until the temperature dependence of the fundamental modes is studied, this vibronic coupling

mechanism can not be totally discounted.

If two discrete components result in the individual Gaussians resolved, band 1 would correspond to a clinopyroxene absorption while band 2 would probably represent absorption due to plagioclase or olivine. However, optical examination of the sample revealed no plagioclase and little (1 to 2 weight% at most) olivine (Singer, pers. comm., 1983). Therefore, it is unlikely the individual Gaussians represent two distinct mineral phases.

From considerations outlined above, there is a single mechanism resulting in two resolvable absorption bands while remaining consistent with interpretation of Gaussian parameters. It is likely that the two resolved bands represent electronic transitions due to Fe^{2+} located in both the M(1) and M(2) crystallographic site in clinopyroxene. Gaussian analysis applied to a wide compositional range of clinopyroxenes would be capable of directly addressing this current interpretation.

The broad absorption seen in olivine slightly longer than 1μm is composed of three overlapping Fe^{2+} crystal field absorptions located at ≈.85-.90, ≈1.05-1.07, and ≈ 1.1-1.24μm (Burns, 1970). These absorptions correspond to the $^5E_5 \rightarrow {}^5B_{1g}$ (M(1)), $^5A_1 \rightarrow {}^5E$ (upper) (M(2)), and $^5E_g \rightarrow {}^5A_{1g}$ (M(1)) electronic transitions respectively, and are due to Fe^{2+} located in the M(1) and M(2) crystallographic sites (Burns, 1974). The Gaussian analysis of OLV01 was performed in hopes of distinguishing these three bands. However, the absorption band centered at ≈.65μm overlaps the region of interest so one additional Gaussian was included to account for this feature, resulting in a four Gaussian analysis of OLV01. This band at ≈.65μm has been attributed to $Fe^{2+} \rightarrow Fe^{3+}$ charge transfer (Mao and Bell, 1972), a spin-forbidden Fe^{2+} transition (Burns, 1970; Runciman et al., 1973), and Cr^{3+} crystal field transition (Burns

et al., 1973; Adams, 1975). The current analysis, including this feature, might help distinguish the correct mechanism responsible. The resultant fits and residuals are shown in Figure 20a through 20e. Figure 21 shows that Gaussians 1, 3, and 4 move to longer wavelengths as temperature increases while Gaussian 2 moves to shorter wavelengths. Also, Gaussians 1, 3, and 4 increase in width while Gaussian 2 decreases in width as temperature increases. Gaussians 2, 3, and 4 show an overall increase in intensity while Gaussian 1 decreases intensity as temperature increases. Again the combined Gaussian envelope TBM remains uneffected by variations of individual Gaussian parameters as seen in Figure 15, with the variations insignificant, as discussed previously.

Since Gaussians 2, 3, and 4 correspond well to the crystal field transitions discussed by Burns (1974), the analysis of these features will be discussed first. The parameters of Gaussians 3 and 4 exhibit trends which are consistent with crystal field predictions of how these bands would react to increased temperature. Gaussian 2 exhibits anomalous behavior in center and width values compared to Gaussians 3 and 4, and since it arises from a transition due to Fe^{2+} in the M(1) site as Gaussian 4 does, it is important to consider what causes this deviation. Both liquid nitrogen and high temperature X-ray studies of Forsterite (Smyth and Hazen, 1973; Hazen, 1976) and Fayalite (Smyth, 1975; Hazen, 1977) indicate an overall expansion of the M(1) and M(2) crystal sites. However, each site undergoes differing distortion as temperature is increased. All M(1)-O distances expand with increasing temperature but the bonds located within the x-y plane show greater rates of expansion than the bonds along the z-axis. Thus, the overall symmetry of the site is compressed along the z-axis as temperature

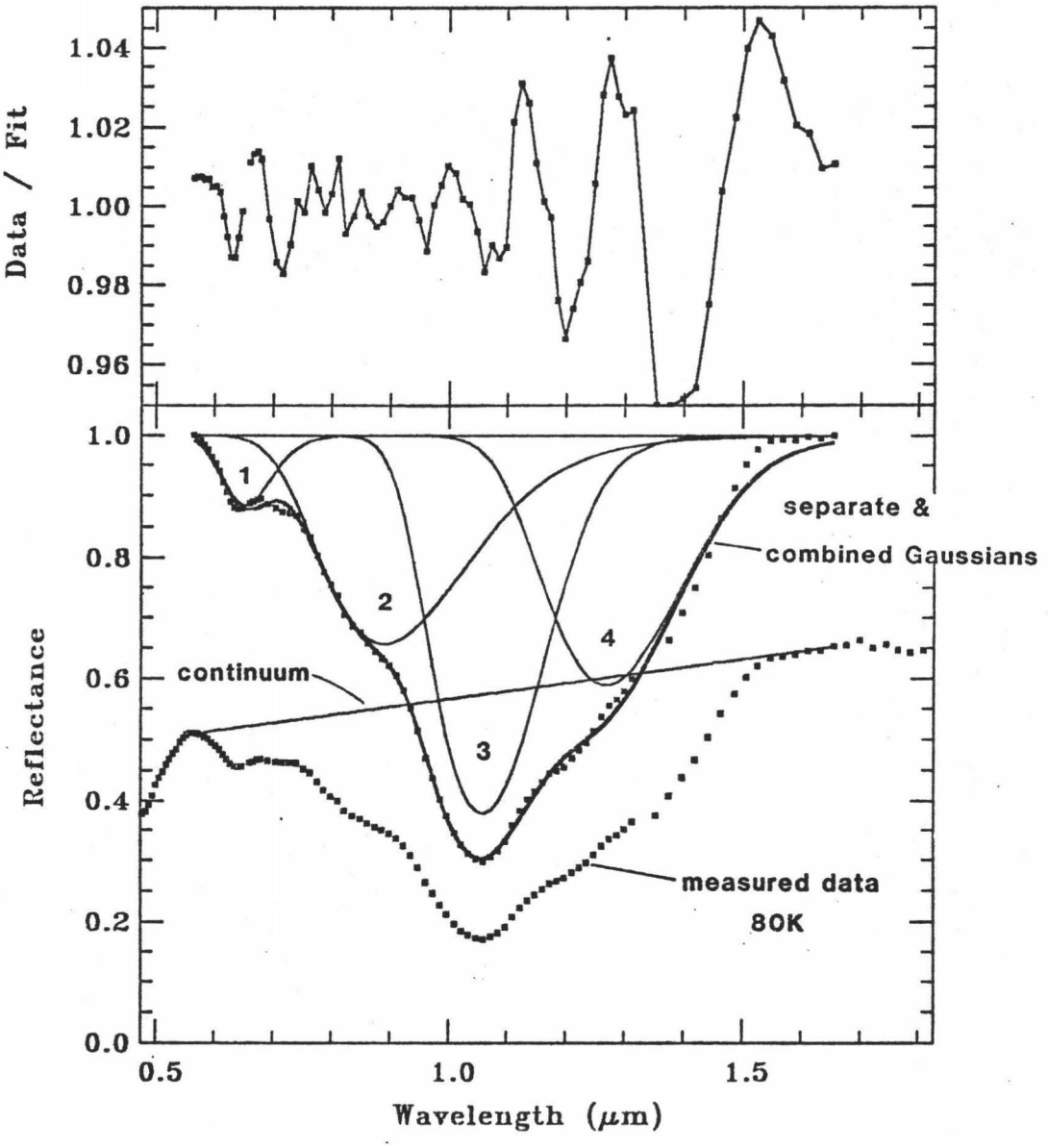

Figure 20a. Deconvoluted Gaussian bands and residuals of OLV01 spectrum at ≈80K.

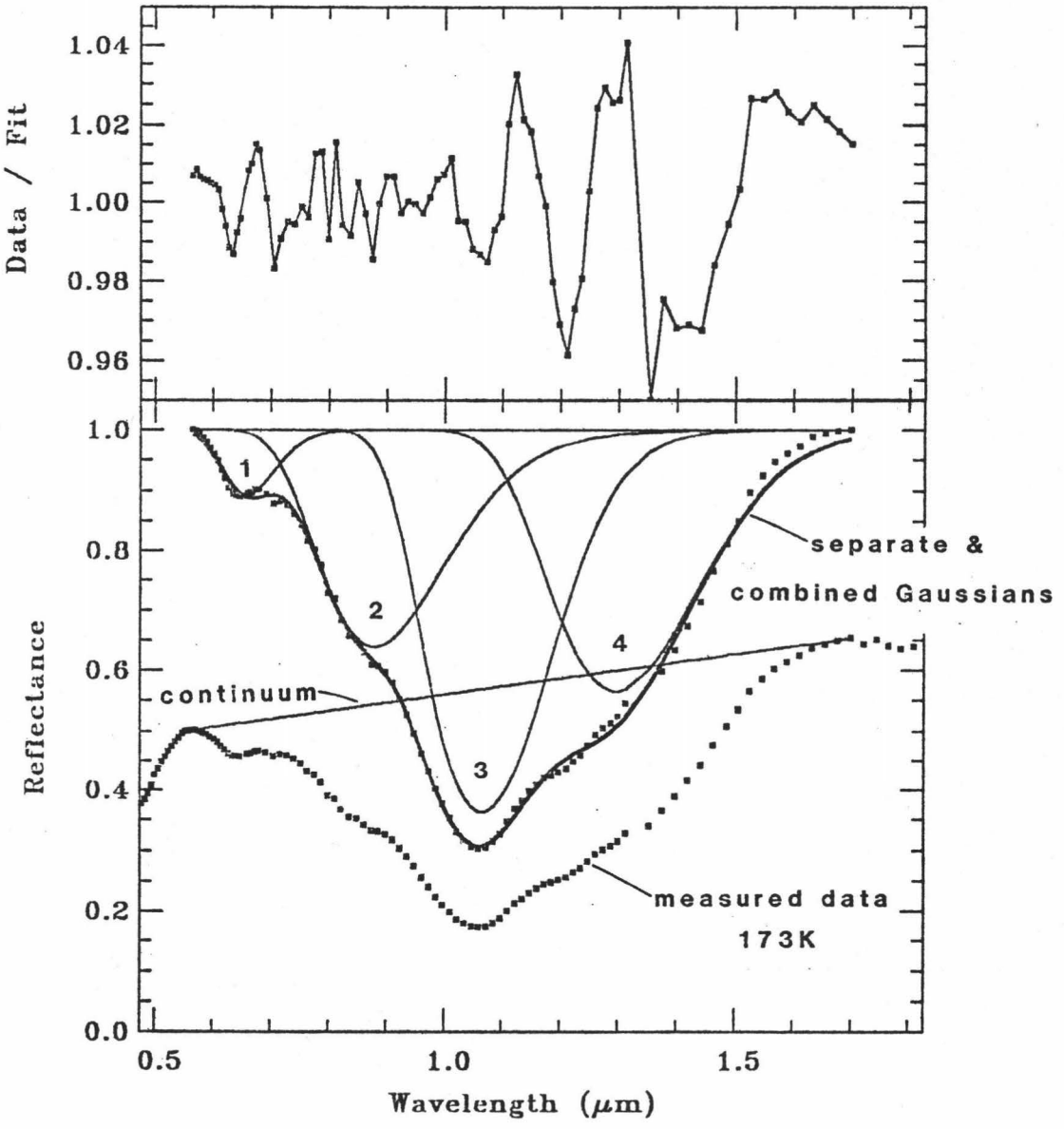

Figure 20b. Deconvoluted Gaussian bands and residuals of OLV01 spectrum at 173K.

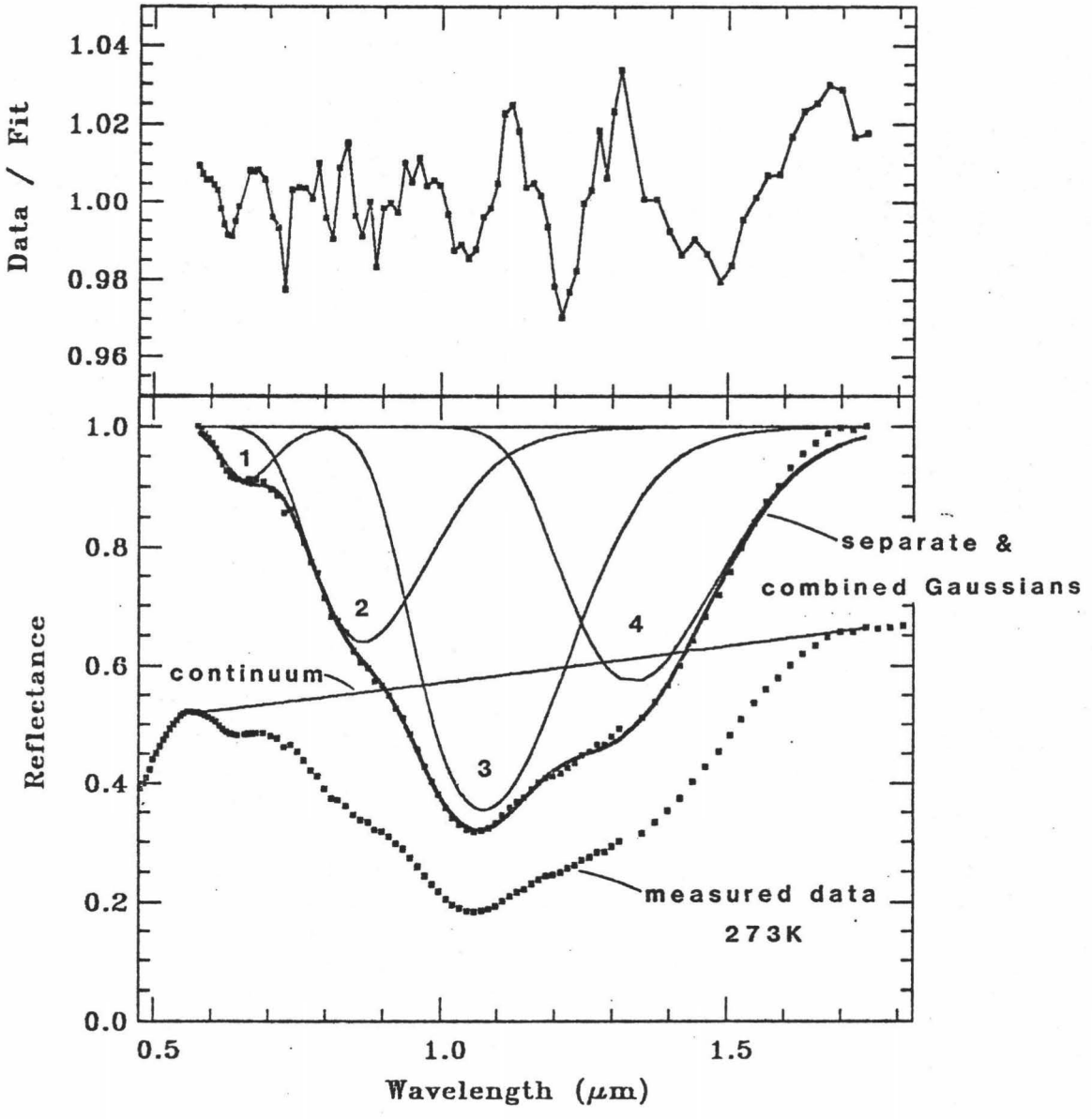

Figure 20c. Deconvoluted Gaussian bands and residuals of OLV01 spectrum at 273K.

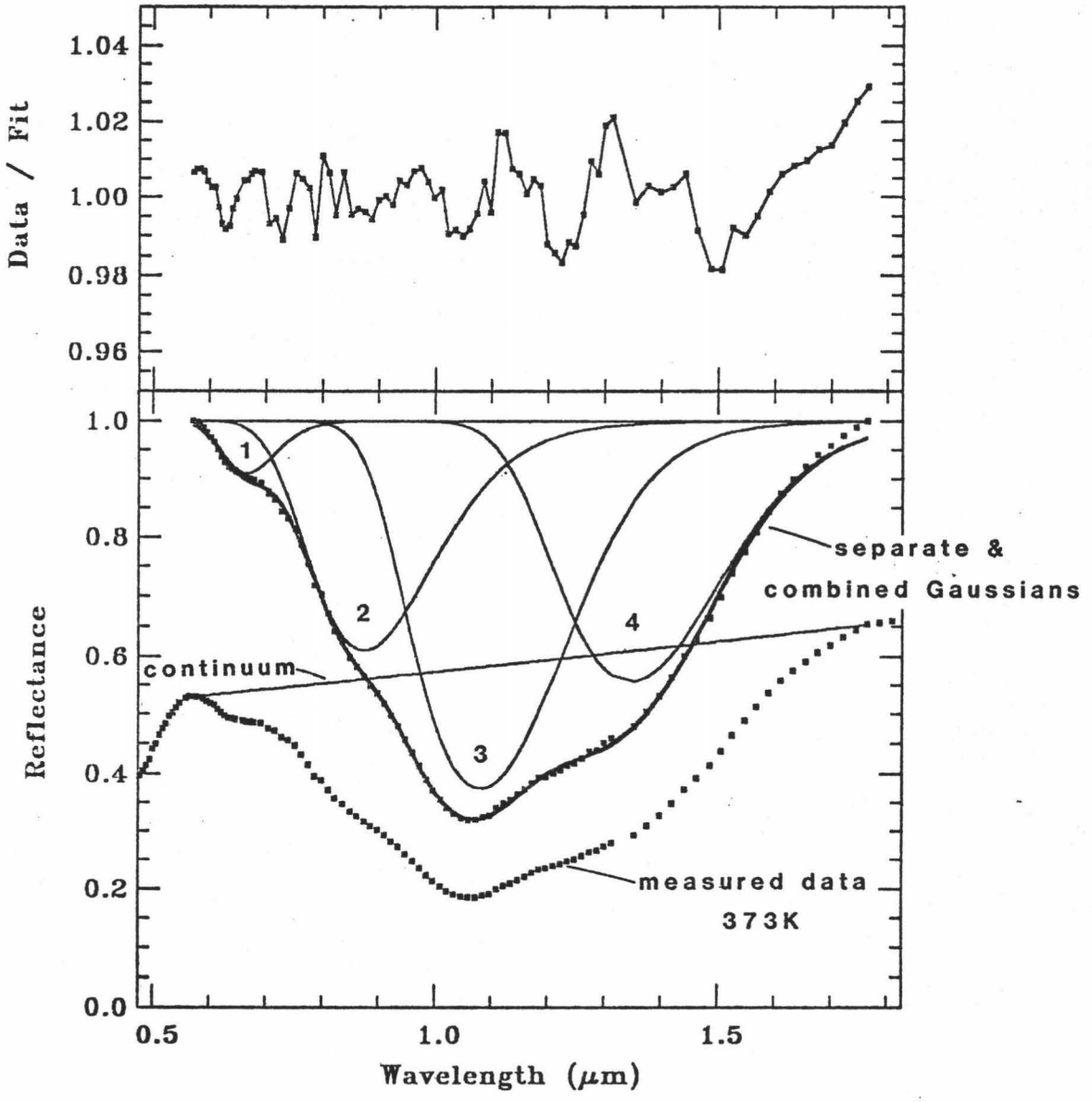

Figure 20d. Deconvoluted Gaussian bands and residuals of OLV01 spectrum at 373K.

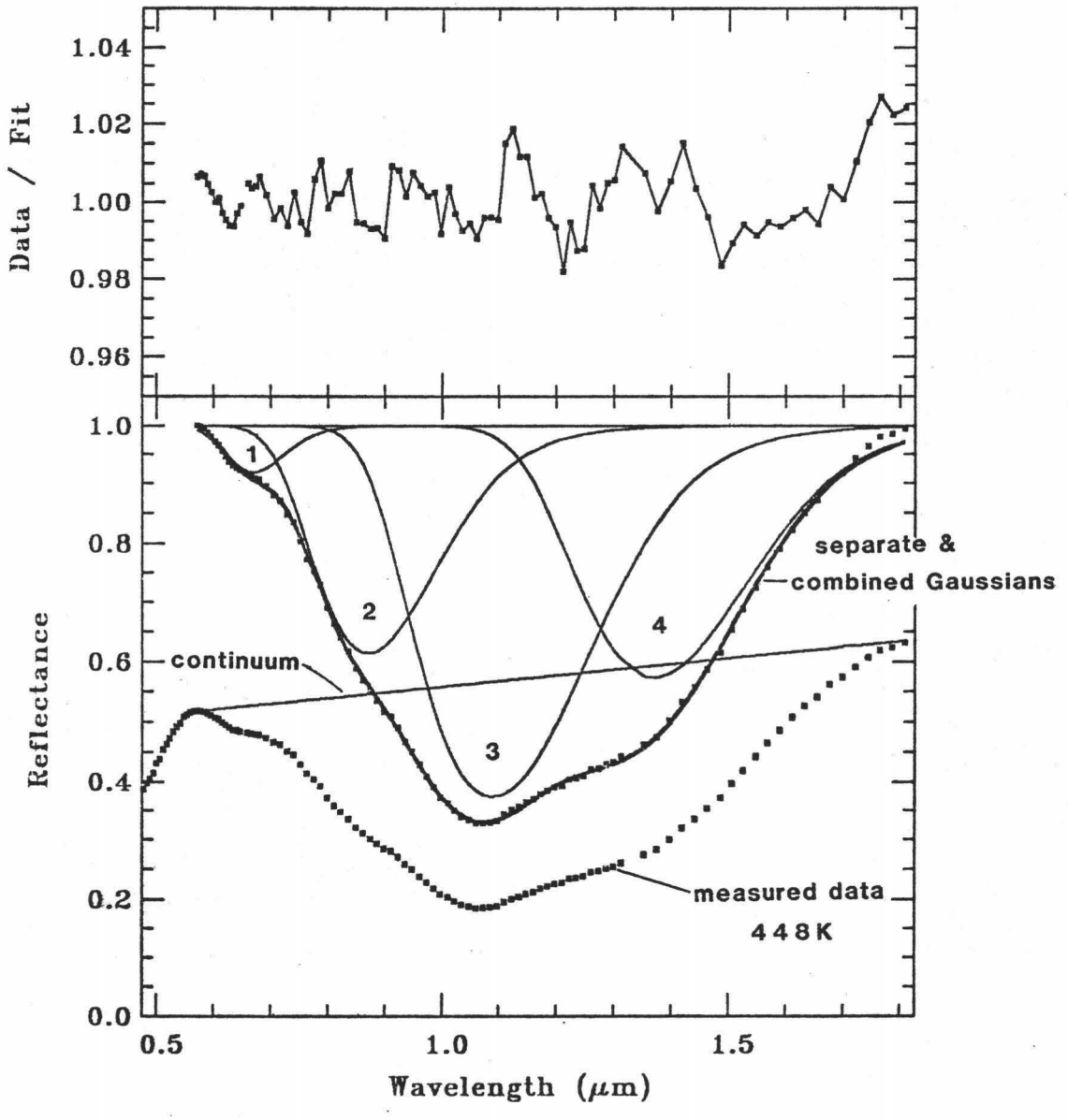

Figure 20e. Deconvoluted Gaussian bands and residuals of OLV01 spectrum at 448K.

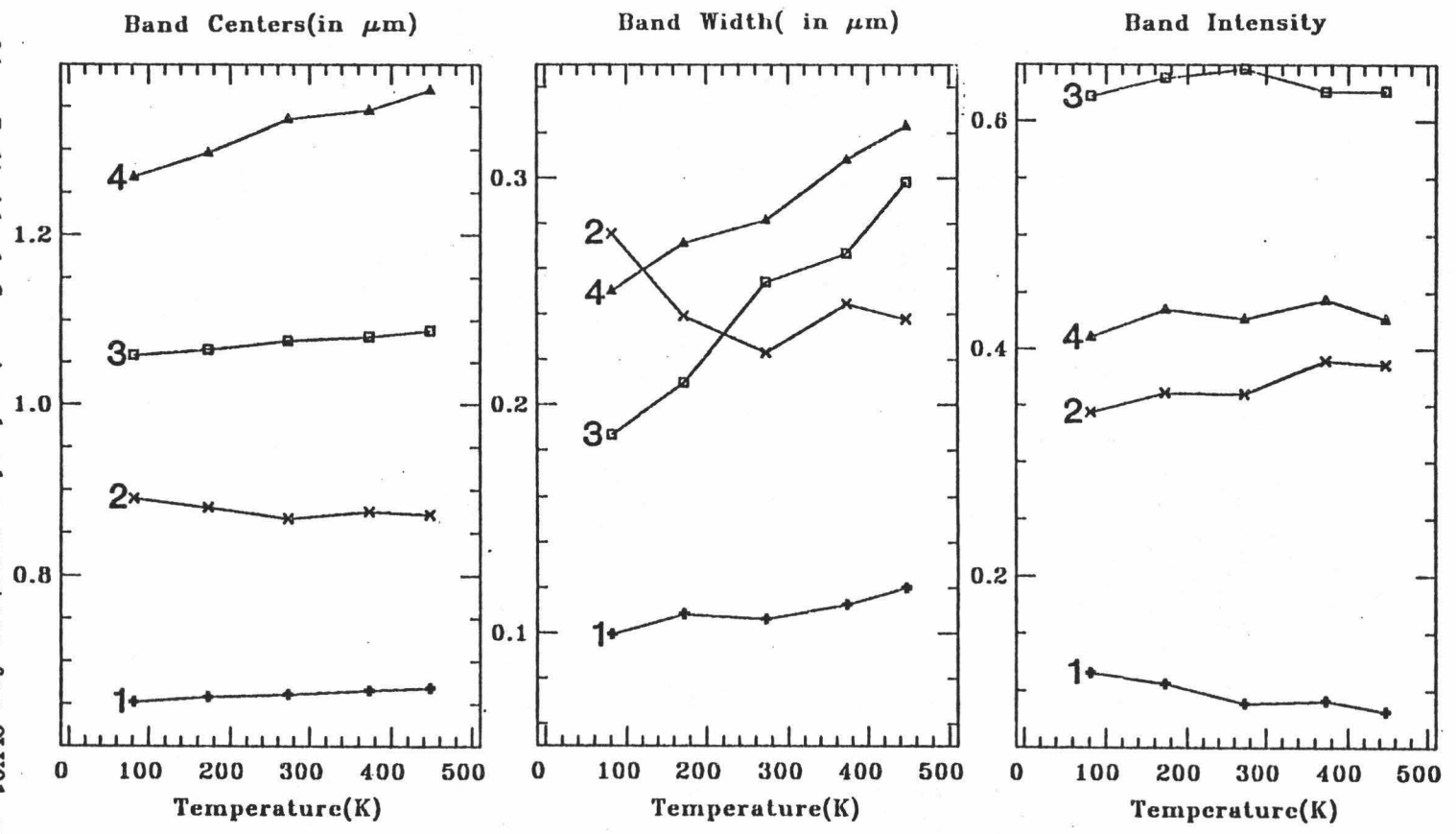

Figure 21. Individual Gaussian band parameters for OLV01 spectra as a function of temperature.

increases leading to a lower symmetry environment. This lowering of symmetry should result in greater splitting of the upper energy levels with transitions to both moving to lower energies since the entire site is expanding. Another possible mechanism effecting the trends of Gaussian 2 parameters is interaction with Gaussian 1 within the Gaussian fitting routine itself. This could effect both Gaussian centers but since the intensity of Gaussian 1 is so small, the trend of Gaussian 2 band width is probably real. It is difficult to assign a specific mechanism which can explain the parameter trends of Gaussian 2.

If Gaussian 1 is due to the Fe^{2+}->Fe^{3+} charge transfer (Mao and Bell, 1972), as temperature increases the distances between adjacent cations also increases so that it requires more energy to accomplish the same transition. This would be expressed as a shifting of the band center to shorter wavelengths and a decrease in band intensity. The Gaussian results are conflicting as band centers do not exhibit the proper trend while the band intensity does. If Gaussian 1 is due to a Fe^{2+} spin-forbidden band the band intensity should increase as more energy is put into the system (temperature increased). This is the exact opposite of the trend seen in Figure 21. If Gaussian 1 is due to a Cr^{3+} crystal field transition it should show similar trends as the Fe^{2+} bands, again the band intensity shows anomalous behavior compared to the other three bands. Thus, this analysis has not resolved the physical mechanism resulting in this absorption feature. If the interaction of Gaussians 1 and 2 within the fitting routine itself is occurring and it was possible to eliminate, this question could potentially be resolved.

REFERENCES

Adams, J.B. (1975), Uniqueness of Visible and Near-Infrared Reflectance Spectra of Pyroxenes and Other Rock-Forming Minerals. In Infrared and Raman Spectroscopy of Lunar and Terrestrial Minerals (C. Karr, Ed.), p91-116, Academic Press, New York, NY.

Bancroft, G.M., Burns, R.G., and Howie, R.A. (1967) Determination of the cation distribution in the orthopyroxene series by the Mossbauer effect., Nature, 213, 1221-1223.

Brown, G.E., Papike, J.J., and Sueno, S., (1972), A Comparison of the Structures of Low and High Pigeonite., JGR, 77, 5778-5789.

Burns, R.G., (1970), Mineralogical Applications of Crystal Field Theory, Cambridge Univ. Press, London., 224p.

Burns, R.G., (1974), The Polarized Spectra of Iron in Silicates: Olivine. A discussion of Neglected Contributions from Fe^{2+} Ions in M(1) Sites, Am. Mineral. 59, 625-629.

Burns, R.G., Huggins, F.E.. and Abu-Eid, R.M., (1972), Polarized Absorption Spectra of Single Crystals of Lunar Pyroxenes and Olivines., The Moon, 4, 93-102.

Cameron, M.P., Sueno, S., Prewitt, C.T., and Papike, J.J., (1974), High Temperature Crystal Chemistry of Acmite, Diopside, Hedenbergite, Jadite, Spodumene, and Ureyite., Am. Mineral., 58, 594-618.

Clark, R.N., (1981), Water Frost and Ice: The Near-Infrared Spectral Reflectance 0.65-2.5, JGR, 86, 3087-3096.

Clark, R.N., (1983), Spectral Properties of Mixtures of Montmorillonite and Dark Carbon Grains: Implications for Remote Sensing Minerals Containing Chemically and Physically Adsorbed Water, JGR, 88, 10635-10644.

Clark, R.N. and Roush, T.L., (1984), Reflectance Spectroscopy: Quantitative Analysis Techniques for Remote Sensing Applications, in press.

Cotton, F.A., (1963) Chemical Applications of Group Theory, Wiley-Interscience, New York, NY, 386p.

Farr, T.G., Bates, B.A., Ralph, R.L., and Adams J.B., (1980) Effects of overlapping optical absorption bands of pyroxene and glass on the reflectance spectra of lunar soils. Proc. Lunar Planet. Sci. Conf. 11th, 719-729.

Goldman, D.S. and Rossman, G.R., (1977), The spectra of Iron in Orthopyroxene revisited: The splitting of the ground state, Am. Mineral., 62, 151-157.

Hazen, R.M., (1976), Effects of temperature and pressure on the crystal structure of forsterite, Am. Mineral., 61, 1280-1293.

Hazen, R.M., (1977), Effects of temperature and pressure on the crystal structure of ferromagnesian olivine, Am. Mineral., 62, 286-295.

Hazen, R.M., Mao, H.K., and Bell, P.M., (1977) Effects of compositional variation on absorption spectra of lunar olivines, Proc. Lunar Sci. Conf. 8th, 1081-1090.

Hazen, R.M., Bell, P.M., and Mao, H.K., (1978) Effects of compositional variation on absorption spectra of lunar pyroxenes., Proc. Lunar Planet. Sci. Conf. 10th, 2919-2934.

Hunt, J.M., Wisherd, M.P., and Bonham, L.C., (1950) Infrared Absorption Spectra of Minerals and Other Inorganic Compounds., Anal. Chem., 22, No. 12, 1478-1497.

Kaper, H.G., Smits, D.W., Schwarz, U., Takakubo, K., and Van Worder, H., (1966), Computer analysis of observed distributions into Gaussian components, Bull. Astron. Inst. Neth., 18, 465-487.

Launer, P.J., (1952) Regularities in the Infrared Absorption Spectra of Silicate Minerals., Am. Mineral., 37, 764-784.

Lyon, R.J.P. and Green, A.A., (1975) Reflectance and Emittance of Terrain in the Mid-Infrared (6-25μm) Region. in Infrared and Raman Spectroscopy of Lunar and Terrestrial Minerals., C. Karr Jr. Ed., Academic Press, New York, NY, 375p.

Mao, H.K. and Bell, P.M., (1972), Interpretation of the Pressure Effect on the Optical Absorption Bands of Natural Fayalite to 20kB, Carnagie Inst. Yr. Bk. 1971, 524-527.

McCord, T.B., Clark, R.N., Hawke, B.R., McFadden, L.A., Owensby, P.D., Pieters, C.M., and Adams, J.B., (1981), Moon: Near-Infrared Spectral Reflectance, A First Good Look, JGR, 86, 10883-10892.

Mori, H. and Takeda, H., (1980) Deformational history of Diogenites., 13th Lunar and Planetary Symposium, Inst. Space and Aeronautical Sci., Univ. of Tokyo, 239-246.

Mortimer, R.G., (1981) Mathematics for Physical Chemistry, Macmillan Publishing Co., Inc., New York, NY, 405p.

Nord, G.L., Jr., (1978) The composition and structure of Guinier-Preston zones in lunar orthopyroxene., 9th International Congress on Electron Microscopy, Vol. 1, 266-267.

Nord, G.L., (1980), Composition, Structure, and Stability of Guinier-Preston Zones in Lunar and Terrestrial Orthopyroxene., Phys. Chem. Minerals, 6, 109-120.

Rossman, G.R., (1980) Pyroxene Spectroscopy, in Reviews in Mineralogy, Volume 7, Pyroxenes, C. Prewitt Ed., Mineralogical Society of America, Washington, D.C., 525p.

Runciman, W.A., Sengupta, D., and Gourley, J.T., (1973), The Polarized Spectra of Iron in Silicates II. Olivine., Am. Mineral., 58, 451-456.

Singer, R.B., (1981), Near-Infrared Spectral Reflectance of Mineral Mixtures: Systematic Combinations of Pyroxenes, Olivine, and Iron Oxides., JGR, 86, 7967-7982.

Smyth, J.R., (1973), An Orthopyroxene Structure Up to 850°C., Am. Mineral., 58, 636-648.

Smyth, J.R., (1974), The High Temperature Crystal Chemistry of Clinohypersthene., Am. Mineral., 59, 1069-1082.

Smyth, J.R., (1975), High Temperature Crystal Chemistry of Fayalite., Am. Mineral., 60, 1092-1097.

Smyth, J.R. and Hazen, R.M., (1973), The Crystal Structures of Forsterite and Hortonolite at Several Temperatures Up to 900°C., Am. Mineral., 58, 588-593.

Sueno, S., Cameron, M., and Prewitt, C.T., (1976), Orthoferrosilite: High Temperature Crystal Chemistry., Am. Mineral., 61, 38-53.

Takeda, H., (1979), A Layered-Crust Model of a Howardite Parent Body, Icarus, 40, 455-470.

White, W.B. and Keester, K.L., (1966), Optical Absorption Spectra of Iron in the Rock-Forming Silicates., Am. Mineral., 51, 774-791.

CHAPTER V: APPLICATIONS TO REMOTE SENSING

APPLICATIONS TO REMOTE SENSING

In order to investigate the effects of surface temperature variations on reflectance spectra of planetary bodies, a theoretical surface must be constructed. A standard thermal model will be used as a basis for constructing the surface, and the assumptions of that model are presented in Morrison and Lebofsky (1979) but will be reviewed here for clarity. The standard model assumes: 1)the surface is exactly spherical; 2)it is composed of a rough dielectric material with low thermal conductivity to a depth of at least a few centimeters implying it is in instantaneous thermal equilibrium with the insolation; 3)the photometric properties are those of a dark, dusty surface; 4)in the infrared the emissivity is near unity and less than a few percent of the absorbed insolation is radiated from the unlit hemisphere; and 5)the body is airless and slowly rotating. If these criteria are met then the surface temperature distribution can be expressed by the equation of Brown et al. (1982) as:

$$T(\mu) = 1.523 \times 10^{9}\left[\frac{1 - (.6p_v)}{R^2\varepsilon_b}\right]^{1/4} \mu^{1/4}K \,, \qquad \text{(eqn 1)}$$

where p_v is the geometric or visual albedo ($.6p_v$= bond albedo), R is the heliocenteric distance of the body in centimeters (R>>r, the radius of the body), ε_b is the bolometric emissivity, and μ is the cosine of the angle between the surface normal and the incoming radiation.

It is important to consider how the variables of equation 1 can effect resultant calculated temperatures. This was accomplished by calculating aphelion and perihelion average surface temperature (where $\mu=\bar{\mu}=2/\pi$) using the orbital parameters of 4 Vesta. The average aphelion

and perihelion surface temperature, as a function of geometric albedo, are shown in the first seven rows of Table 4. As seen, surface temperatures differ by about 20±K from aphelion to perihelion for a given albedo, and only by approximately 50K over a wide range of albedo. Rows eight through twelve represent variations of surface temperature as a function of bolometric emmisivity. Differences between calculated aphelion and perihelion surface temperatures are about 30K for a single value and slightly more than approximately 100K over a wide range of values. The heliocentric distance, R, is related to the distance at aphelion, R_a, and perihelion, R_p, by the following equations:

$$R_a = (a + c) \qquad \text{(eqn 2)}$$

$$R_p = (a - c) \qquad \text{(eqn 3)}$$

where,

$$c = \sqrt{a^2 - b^2} \qquad \text{(eqn 4)}$$

and

$$b = \sqrt{1 - e^2} \qquad \text{(eqn 5)}$$

where a is the semi-major axis of the ellipse, b is the semi-minor axis, c is the distance from the center of the ellipse to the focus, and e is the eccentricity. Thus, R_a and R_p can be expressed as a function of the semi-major axis and the eccentricity. Rows thirteen thru twentyfive of Table 4 list the aphelion and perihelion surface

Table 4. Effects of Physical and Orbital Parameter Variation on Average Aphelion and Perihelion Average Calculated Surface Temperature.

row	visual albedo	a+	emmis-ivity	eccen-tricitiy	aphelion temp. (K)	perihelion temp. (K)
1	.001	2.36	.9	.0935	225.6	247.8
2	.1	2.36	.9	.0935	222.2	244.1
3	.2	2.36	.9	.0935	218.6	240.1
4	.4	2.36	.9	.0935	210.7	231.4
5	.6	2.36	.9	.0935	201.9	221.7
6	.8	2.36	.9	.0935	191.6	210.5
7	.999	2.36	.9	.0935	179.5	197.2
8	.229	2.36	.2	.0935	316.8	347.9
9	.229	2.36	.4	.0935	266.4	292.6
10	.229	2.36	.6	.0935	240.7	264.4
11	.229	2.36	.8	.0935	224.0	246.0
12	.229	2.36	1.0	.0935	211.8	232.7
13	.229	1.0	.9	.0935	334.1	367.0
14	.229	2.0	.9	.0935	236.4	259.5
15	.229	3.0	.9	.0935	192.9	211.9
16	.229	4.0	.9	.0935	167.1	183.5
17	.229	5.0	.9	.0935	149.4	164.1
18	.229	2.36	.9	.01	226.3	228.6
19	.229	2.36	.9	.05	221.9	233.3
20	.229	2.36	.9	.1	216.8	239.7
21	.229	2.36	.9	.2	207.6	254.3
22	.229	2.36	.9	.4	192.2	293.6
23	.229	2.36	.9	.6	179.8	359.6
24	.229	2.36	.9	.8	169.5	508.5
25	.229	2.36	.9	.999	160.9	7192.0

+ semi-major axis

temperature as a function of these two parameters. Varying the semi-major axis results in a difference of about 15-30K between aphelion and perihelion surface temperature while extremes of this variable show a difference of approximately 185-200K. Eccentricity has a dramatic effect on aphelion and perihelion surface temperature extremes with small eccentricity resulting in temperature differences of about 2-12K while large eccentricity yields temperature differences of approximately 340 to several thousand K, and 85 to several thousand K over wide ranges of eccentricity In subsequent discussions, it appears that the orbital parameters of a given surface will influence extremes of temperature at aphelion and perihelion to a greater extent than physical parameters of surface materials. This is not surprising since the orbital parameters determine how near the sun a body is located at any point during its orbit.

In order to investigate the effect of a temperature distribution on a monomineralic surface it is necessary to determine the reflected flux from a series of annuluses, each of which represent a different temperature on the surface. The derivation relating the flux contribution to the illumination and viewing geometry of an annulus is presented in Appendix 1. A computer program was designed to use this relationship and given input parameters and the number of temperature increments would calculate the average temperature and spectral contribution from each interval. Input parameters and resultant flux contribution from four temperature intervals are listed for two main-belt asteroids, 4 Vesta and 8 Flora, and two earth-crossing asteroids, 433 Eros and 877 Alinda, are listed in Table 5. Bolometric emissivity was kept constant at .9 and the total number of temperature intervals was 45 in each case. Due to the limited nature of the laboratory data,

Table 5. Resultant Flux Contributions from Various Temperature Intervals for Several Asteroid Bodies.

433 Eros, semi-major axis 1.46, eccentricity .221, p_v .174				
position	contribution from temperature interval			
	< 125K	125-225K	225-325K	> 325K
aphelion	0.0%	4.00%	95.8%	.2%
perihelion	0.0%	.3%	20.0%	79.7
877 Alinda, semi-major axis 2.52, eccentricity .554, p_v.166				
aphelion	.5%	99.5%	0.0%	0.0%
perihelion	0.0%	.3%	20.0%	79.7%
4 Vesta, semi-major axis 2.36, eccentricity .0935, p_v .229				
aphelion	0.0%	41.0%	59.0%	0.0%
perihelion	0.0%	12.5%	87.5%	0.0%
8 Flora, semi-major axis 2.01, eccentricity .1485, p_v .144				
aphelion	0.0%	17.5%	82.5%	0.0%
perihelion	0.0%	3.0%	96.8%	.2%

semi-major axis and visual albedos from Morrison (1977) and eccentricities average of values by Bender (1979) and Williams (1979).

discrete temperature intervals were defined as follows:

$T_{model} < 125K$ represented by ~80K laboratory data

$125K < T_{model} < 225K$ represented by 173K laboratory data

$225K < T_{model} < 325K$ represented by 273K laboratory data

$325K < T_{model} < 425K$ represented by 373K laboratory data

$T_{model} > 425K$ represented by 448K laboratory data

The last temperature increment was not needed for surfaces modelled. In the current model the flux contribution of each mineral, located within a specific temperature interval, can be calculated and the resulting spectrum of the entire surface can be expressed mathematically as:

$$R_{Total(\lambda)} = \sum_{i=1}^{n} x_i R_{i(\lambda,T_i)}, \qquad \text{(eqn 6)}$$

where $R_{Total(\lambda)}$ is the total reflectance, x_i is the spectral contribution (ie. flux) due to the ith temperature interval, and $R_{i(\lambda,T_i)}$ is the reflectance of the mineral at each wavelength λ, and temperature, i. The contribution due to temperatures <125K are insignificant in most cases, and were only used for calculating spectra of 877 Alinda at aphelion. Examples of resultant temperature distributions at aphelion and perihelion, for 4 Vesta and 433 Eros are presented in Figures 22 and 23, respectively.

MONOMINERALIC SURFACES

The measured reflectance of OLV01, PYX02, and PYX07 was used and the resultant monomineralic calculated spectra are presented in Figures 24, 25, 26, and 27. The spectra of the two main-belt asteroids, 4 Vesta (Figure 24) and 8 Flora (Figure 25), show minor differences when

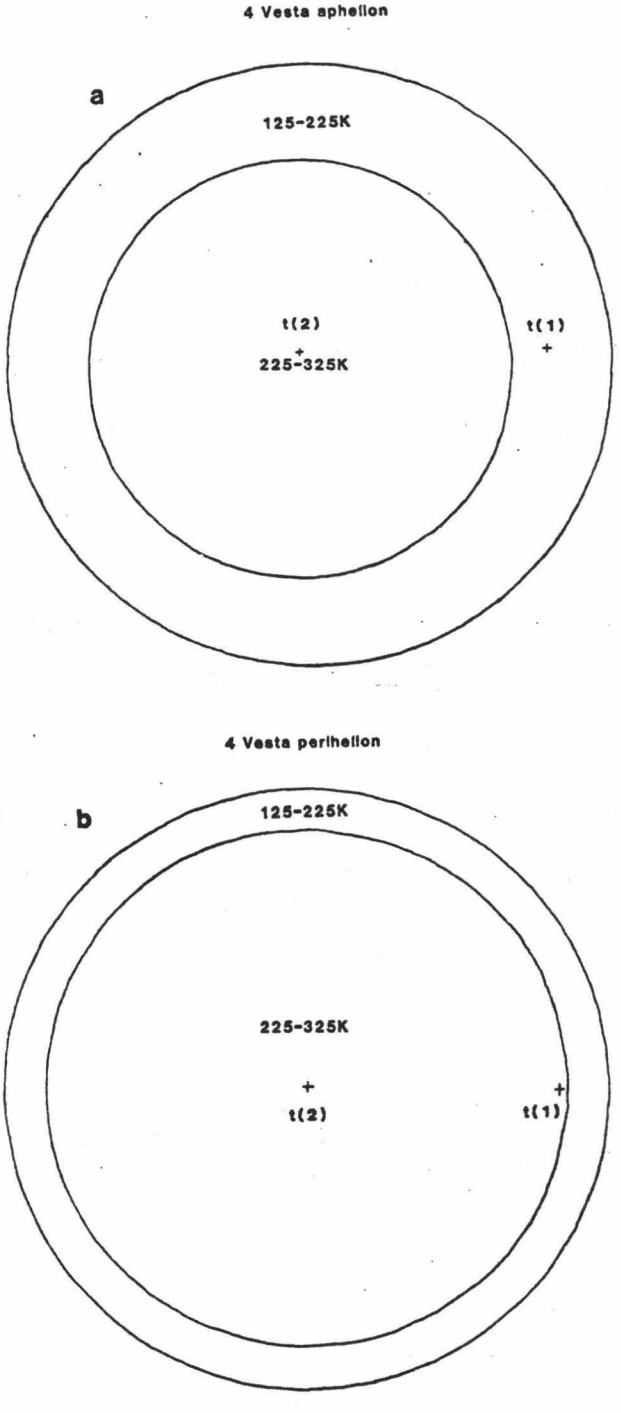

Figure 22. Projected temperature distribution for 4 Vesta, (a)aphelion, (b)perihelion, t(1) and t(2) correspond to where the center of the spot is located for bimineralic surfaces.

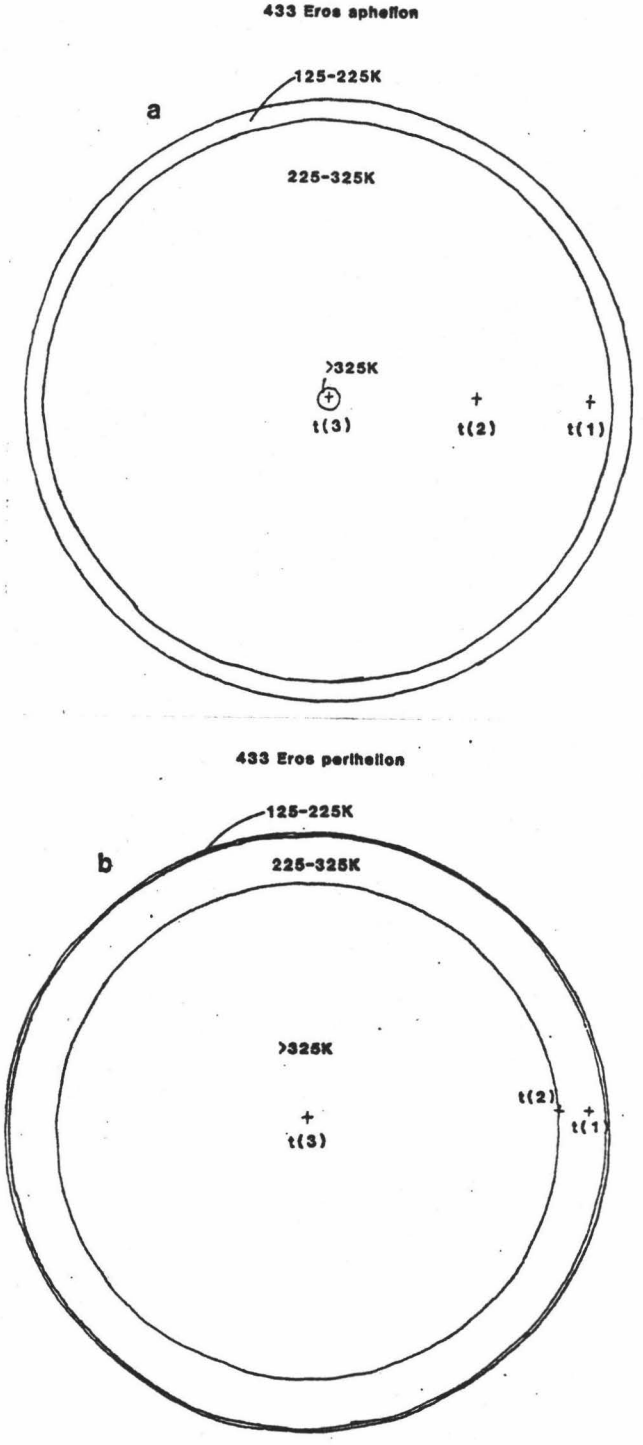

Figure 23. Projected temperature distribution for 433 Eros, (a)aphelion, (b)perihelion, t(1), t(2), and t(3) correspond to where the center of the spot is located for bimineralic surfaces.

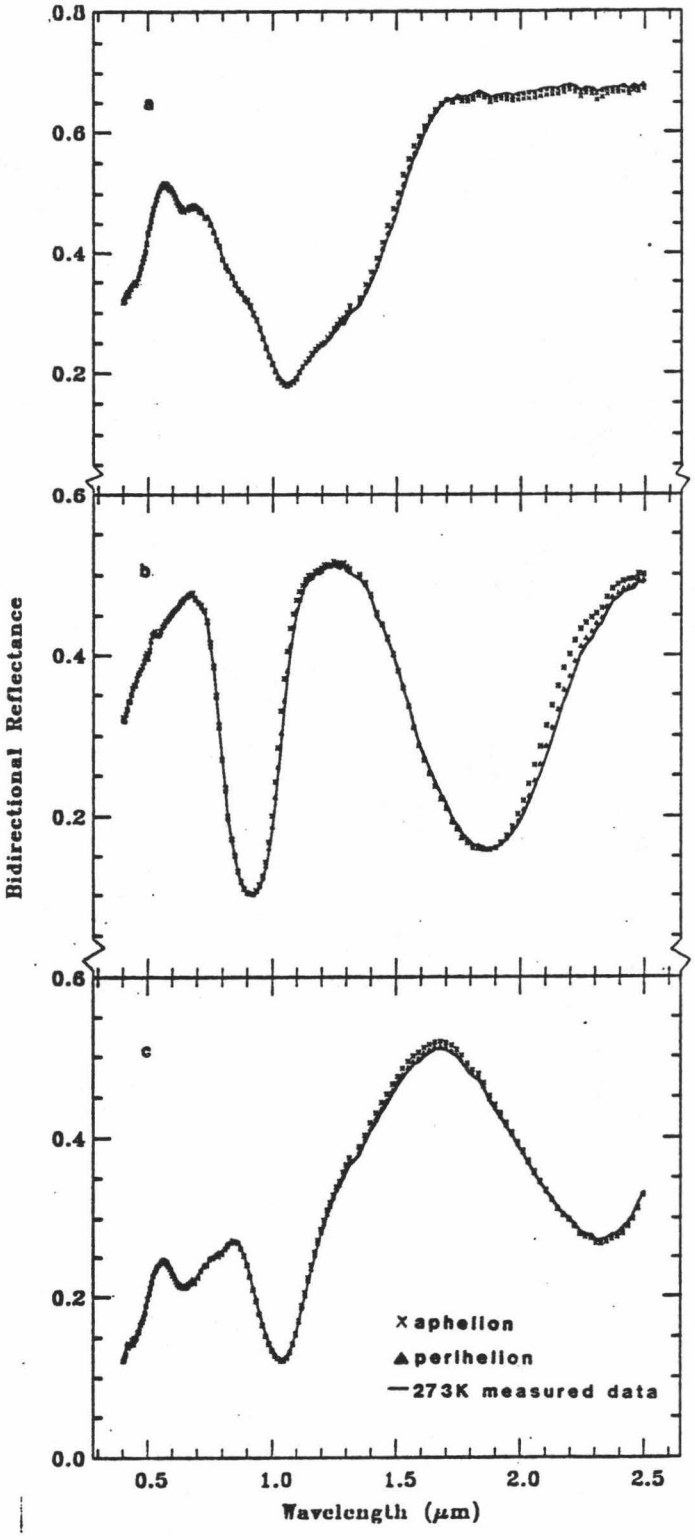

Figure 24. Calculated spectra for a monomineralic surface using the orbital and physical parameters of 4 Vesta, (a)olivine, (b)orthopyroxene, and (c)clinopyroxene.

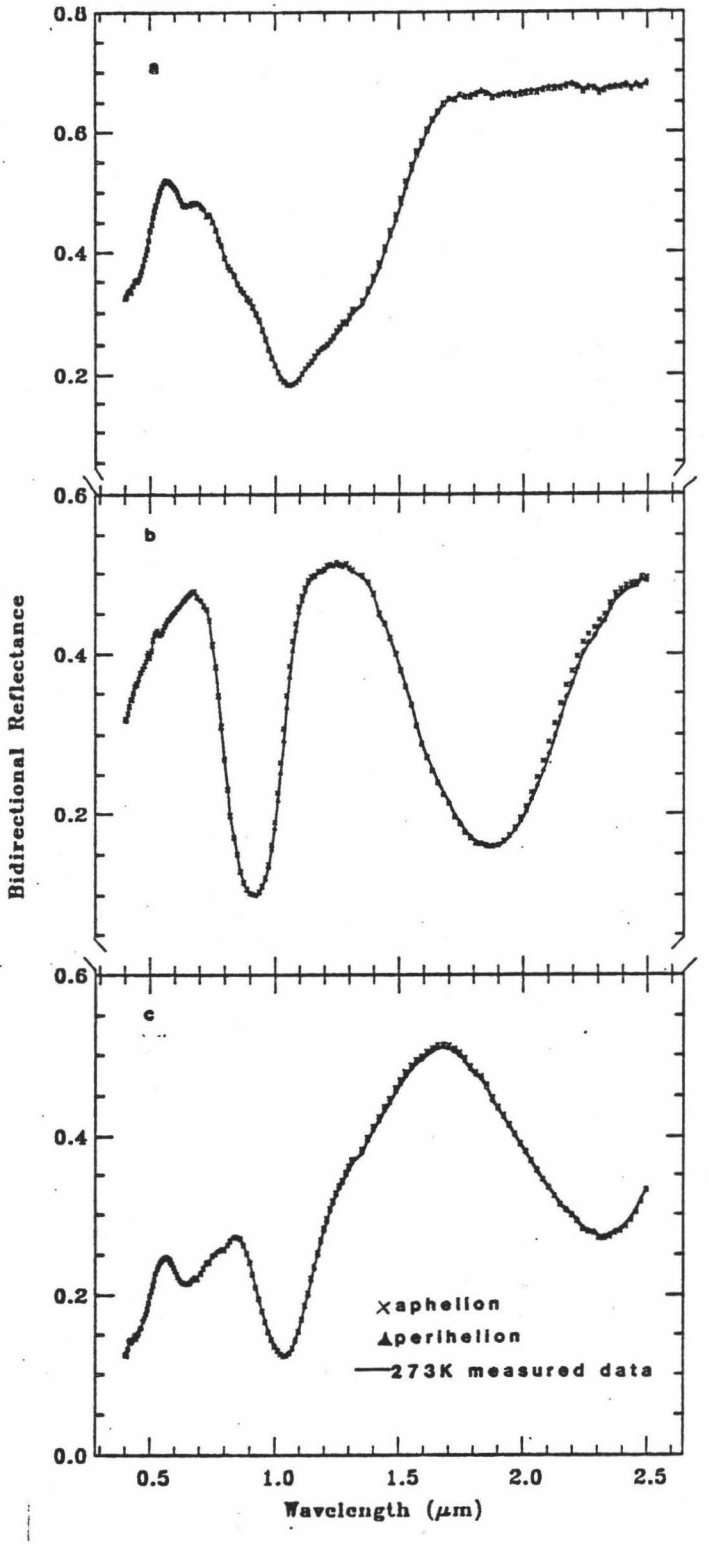

Figure 25. Calculated spectra for monomineralic surface using the orbital and physical parameters of 8 Flora, (a)olivine, (b)orthopyroxene, and (c)clinopyroxene.

aphelion and perihelion data are compared and it is unlikely that one would interpret any difference in chemical or mineralogical composition at the two orbital extremes. However, the spectra of the earth crossers, 433 Eros (Figure 26) and 877 Alinda (Figure 27), show significant differences in absorption band width and apparent minimum position when aphelion and perihelion data are compared which could lead to errors in mineral chemical composition. The aphelion and perihelion calculated spectra of 433 Eros are best matched by the 273K and 373K laboratory data, respectively. The aphelion and perihelion calculated spectra of 877 Alinda are best matched by the 173K and 373K laboratory data, respectively. I will use apparent band minima (ABM), defined as the minimum reflectance value within the region of an absorption band, since Adams (1974) has related the position of the 1 and 2μm absorptions in pyroxenes to iron and calcium concentration within the pyroxenes. In order to directly compare the data presented here with Adams' diagrams (1974, Figures 3 and 5), .025μm needs to be subtracted from data measured on our instruments (Gaffey, pers. comm., 1984).

As an example of the potential errors involved due to differences in the ABM of pyroxenes on a surface of an earth crossing asteroid at aphelion and perihelion consider the spectra of 433 Eros and 877 Alinda. If the surface of 433 Eros is composed of orthopyroxene, at aphelion the 1μm ABM is located at .899μm and the 2μm ABM is 1.851μm. Using the diagrams from Adams (1974) these positions would correspond to a 0-2% Calcium content and a 18% Iron content. At perihelion the 1μm ABM is at .899μm and the 2μm ABM is at 1.874μm corresponding to a 0-2% Calcium and 24.5% Iron content. Thus, while the Calcium content remains unchanged, the Iron content, and therefore the Magnesium content, changes by 6%. A more dramatic difference is illustrated by

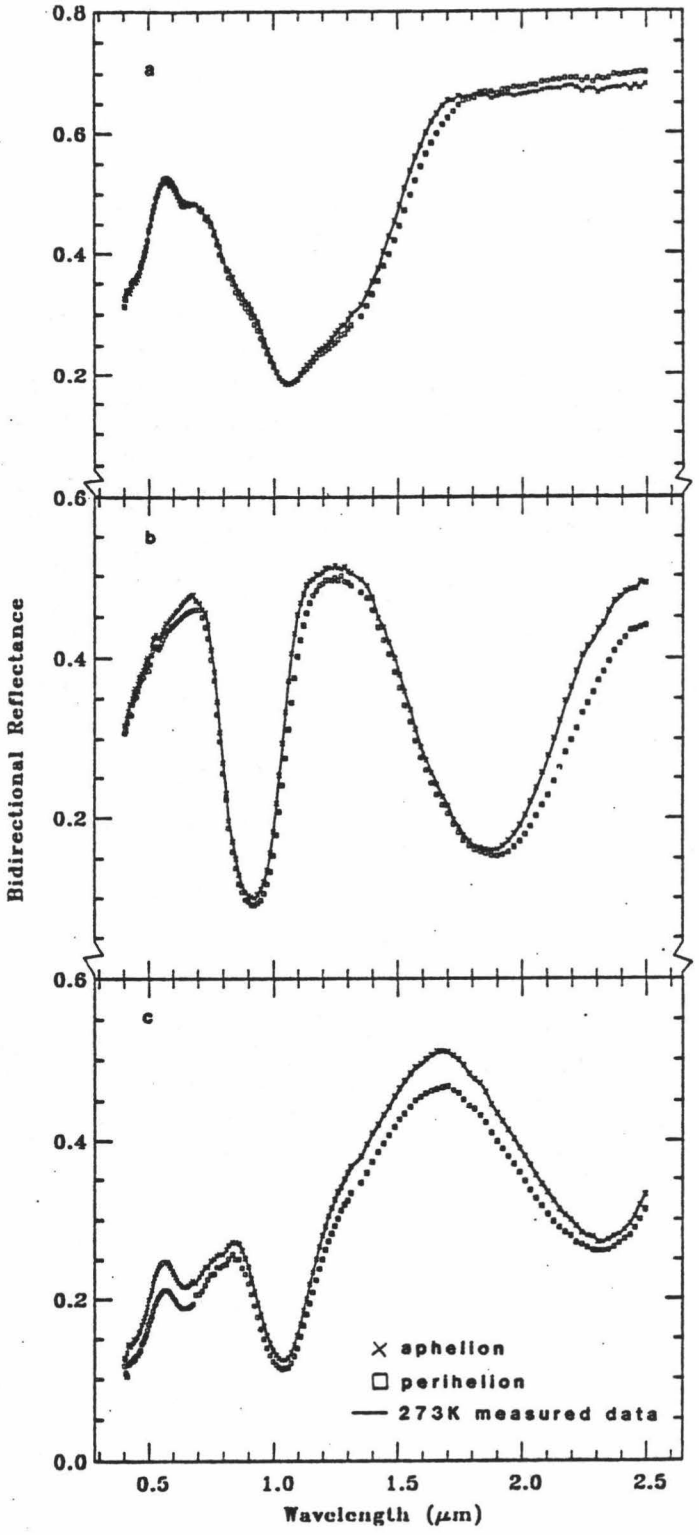

Figure 26. Calculated spectra for monomineralic surface using the orbital and physical parameters of 433 Eros, (a)olivine, (b)orthopyroxene, and (c)clinopyroxene.

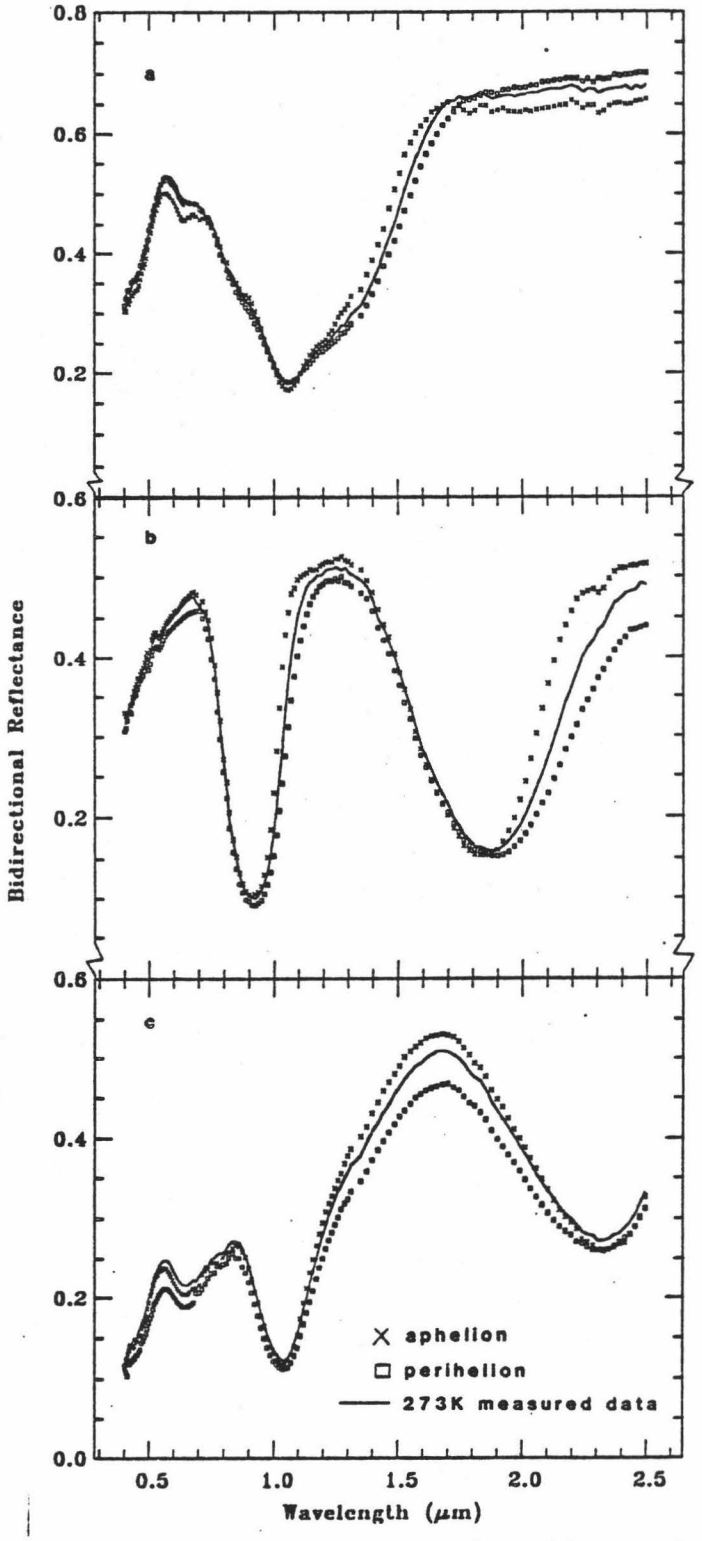

Figure 27. Calculated spectra for monomineralic surface using the orbital and physical parameters of 877 Alinda, (a)olivine, (b)orthopyroxene, and (c)clinopyroxene.

considering the same effects for an orthopyroxene surface of 877 Alinda. At aphelion, the band positions would be interpreted as 0% Calcium and 11.5% Iron, while at perihelion would yield 0-2% Calcium and 24.5% Iron. Thus, both of these surfaces would be interpreted by petrologists as being composed of the bronzite variety of orthopyroxene at aphelion and perihelion. However, meteoricists would interpert both surfaces as being composed of bronzite at aphelion and hypersthene at perihelion.

The same analysis of these surfaces composed of clinopyroxene is more difficult to assess due to the nature of the relationship of the 2μm ABM to Iron content. However, the assignment of 39% Calcium, based on the ABM of the 1μm band, would remain unchanged for both surfaces at perihelion and aphelion.

TWO COMPONENT MIXTURES

The orbital and physical parameters for two surfaces, 4 Vesta and 433 Eros, and the laboratory data of OLV01, PYX02, and PYX07 were used to model a more complex situation. The surface is designed such that it is composed of a major mineral component which has a spot of defined areal extent that rotates across the field of view. This model assumes that the viewing geometry is at zero phase, the center of the spot is located along the equator, and ignores any opposition effect. The spot is defined to have an areal coverage equal to 20% of the projected disk when it is centered at the sub-solar/observer point. Time intervals between locations of the spot on the disk are defined to correspond to the maximum spectral contribution of the spot to each temperature interval on the entire disk and are labelled in Figures 22 and 23. The spectral contribution at each time increment, due to each temperature interval, and the total contribution of the spot is listed in Table 6.

Table 6. Spectral Contribution of Each Component for a Two Component Surface. Based on Actual Orbital and Physical Data for Each Surface.

4 Vesta									
	posi-	125-225 (K)		225-325 (K)		>325 (K)		total	
time	tion	comp a	spot	comp a	spot	comp a	spot	comp a	spot
t(1)	ap.	.83	.17	.9	.1	0.0	0.0	.871	.129
t(2)	ap.	1.0	0.0	.645	.527	0.0	0.0	.689	.311
t(1)	per.	.81	.19	.87	.13	0.0	0.0	.8625	.1375
t(2)	per.	1.0	0.0	.645	.355	0.0	0.0	.689	.311
433 Eros									
t(1)	ap.	.88	.12	.88	.12	1.0	0.0	.878	.122
t(2)	ap.	1.0	0.0	.75	.25	1.0	0.0	.76	.24
t(3)	ap.	1.0	0.0	.678	.322	0.0	1.0	.689	.311
t(1)	per.	.84	.16	.84	.16	1.0	0.0	.896	.104
t(2)	per.	.85	.15	.82	.18	.88	.12	.868	.132
t(3)	per.	1.0	0.0	1.0	0.0	.61	.39	.689	.311

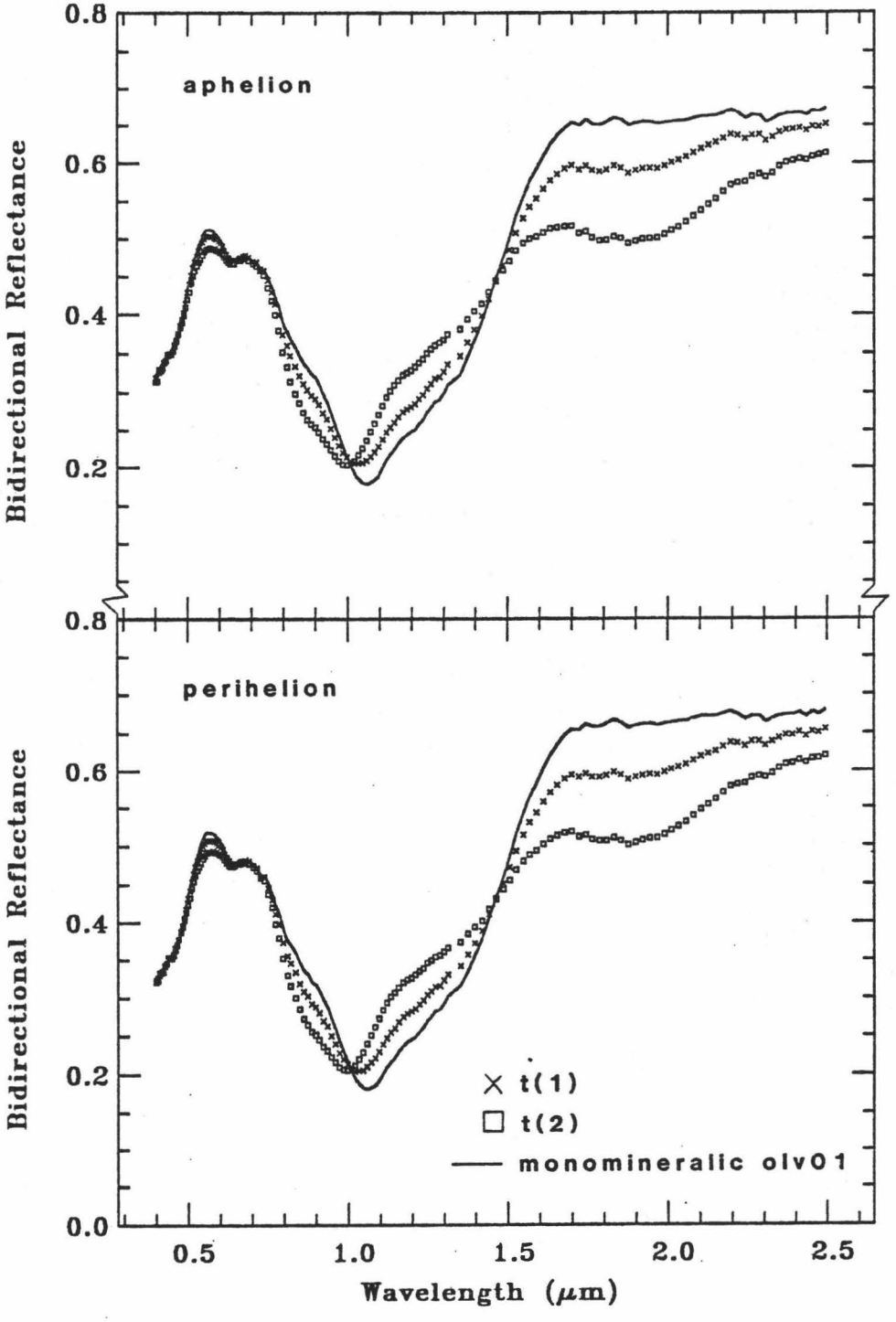

Figure 28. Calculated olivine surface with orthopyroxene spot mixture spectra for two time increments at aphelion and perihelion using the orbital and physical data of 4 Vesta.

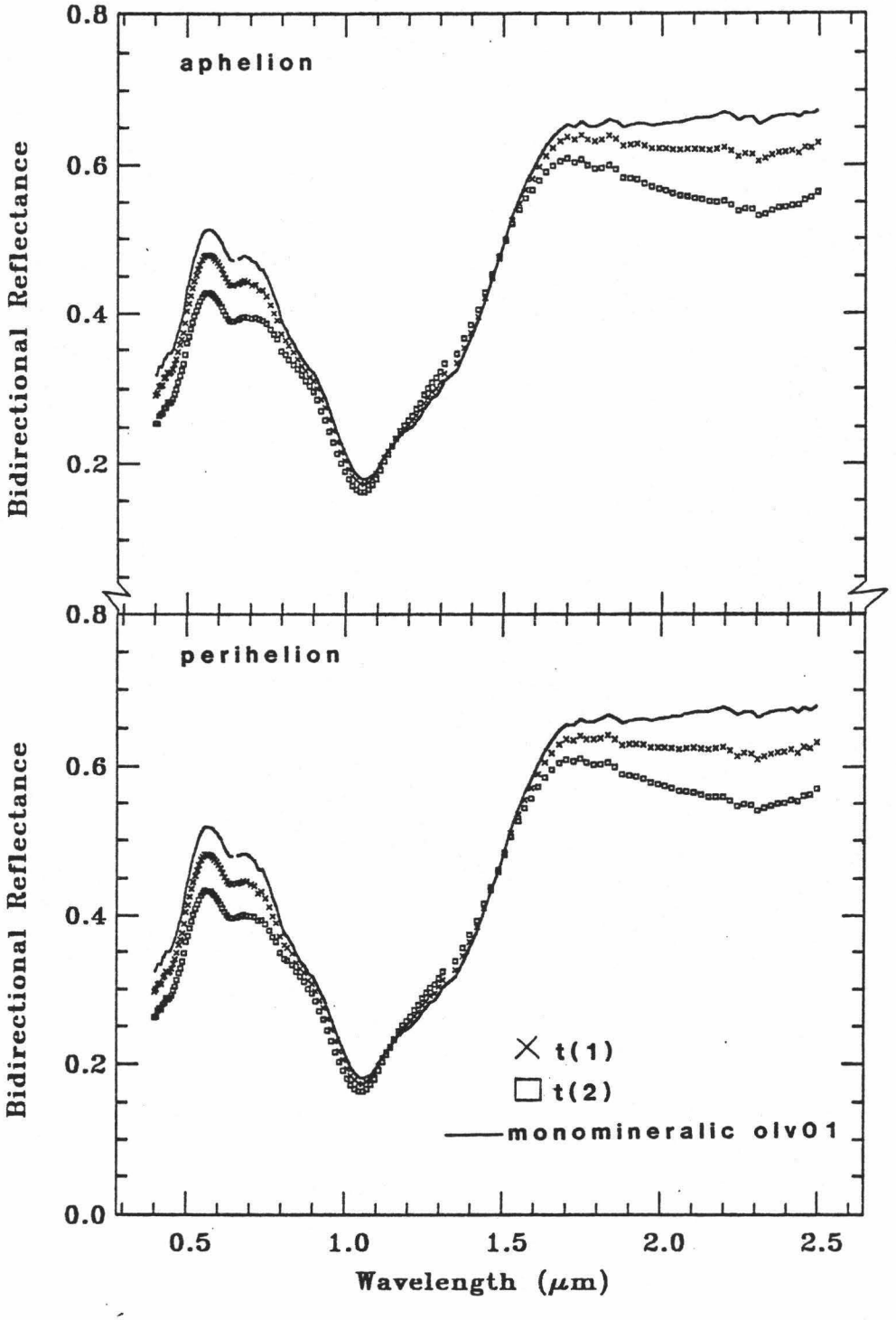

Figure 29. Calculated olivine surface with clinopyroxene spot mixture spectra for two time increments at aphelion and perihelion using the orbital and physical data of 4 Vesta.

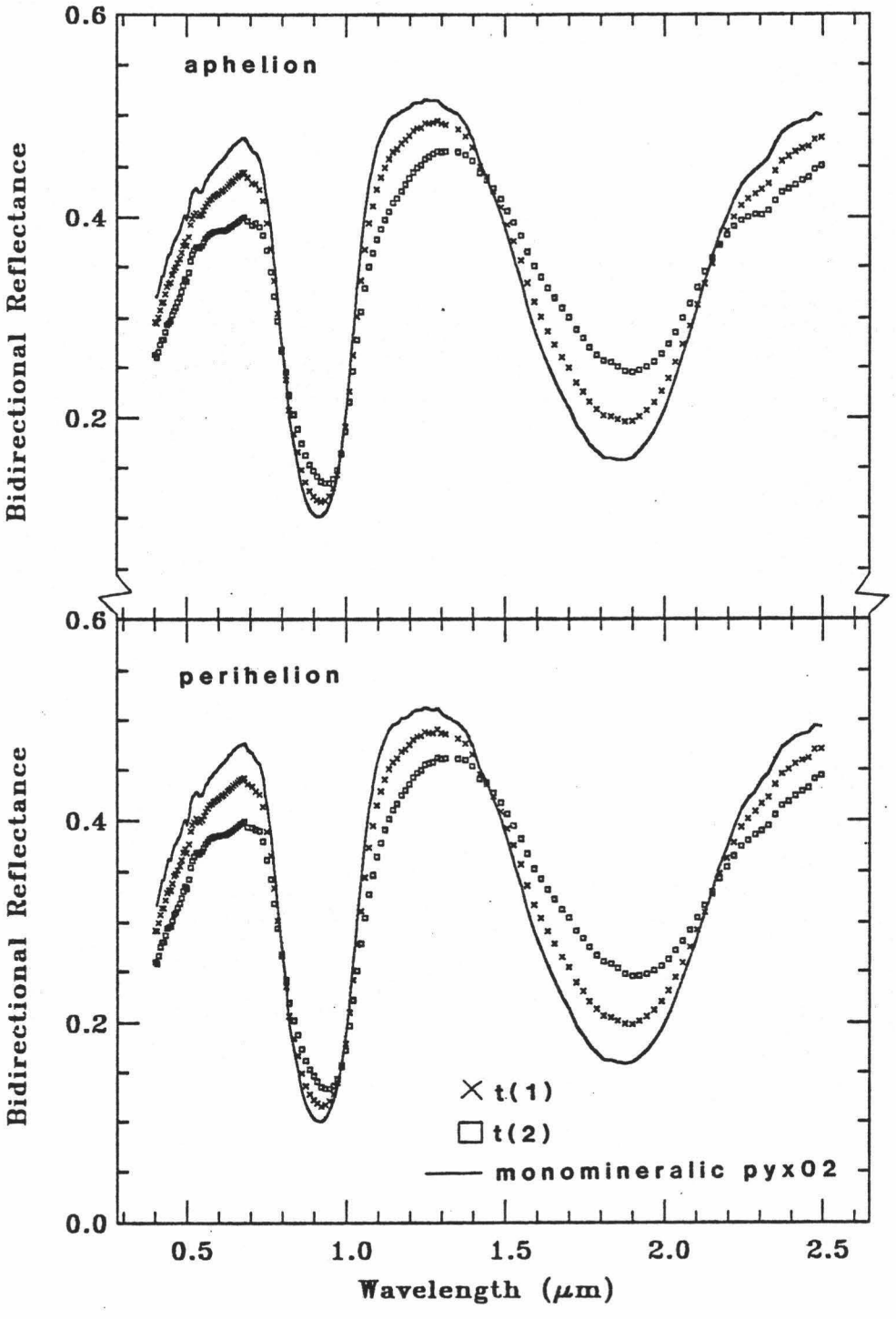

Figure 30. Calculated orthopyroxene surface with clinopyroxene spot mixture spectra for two time increments at aphelion and perihelion using the orbital and physical data of 4 Vesta.

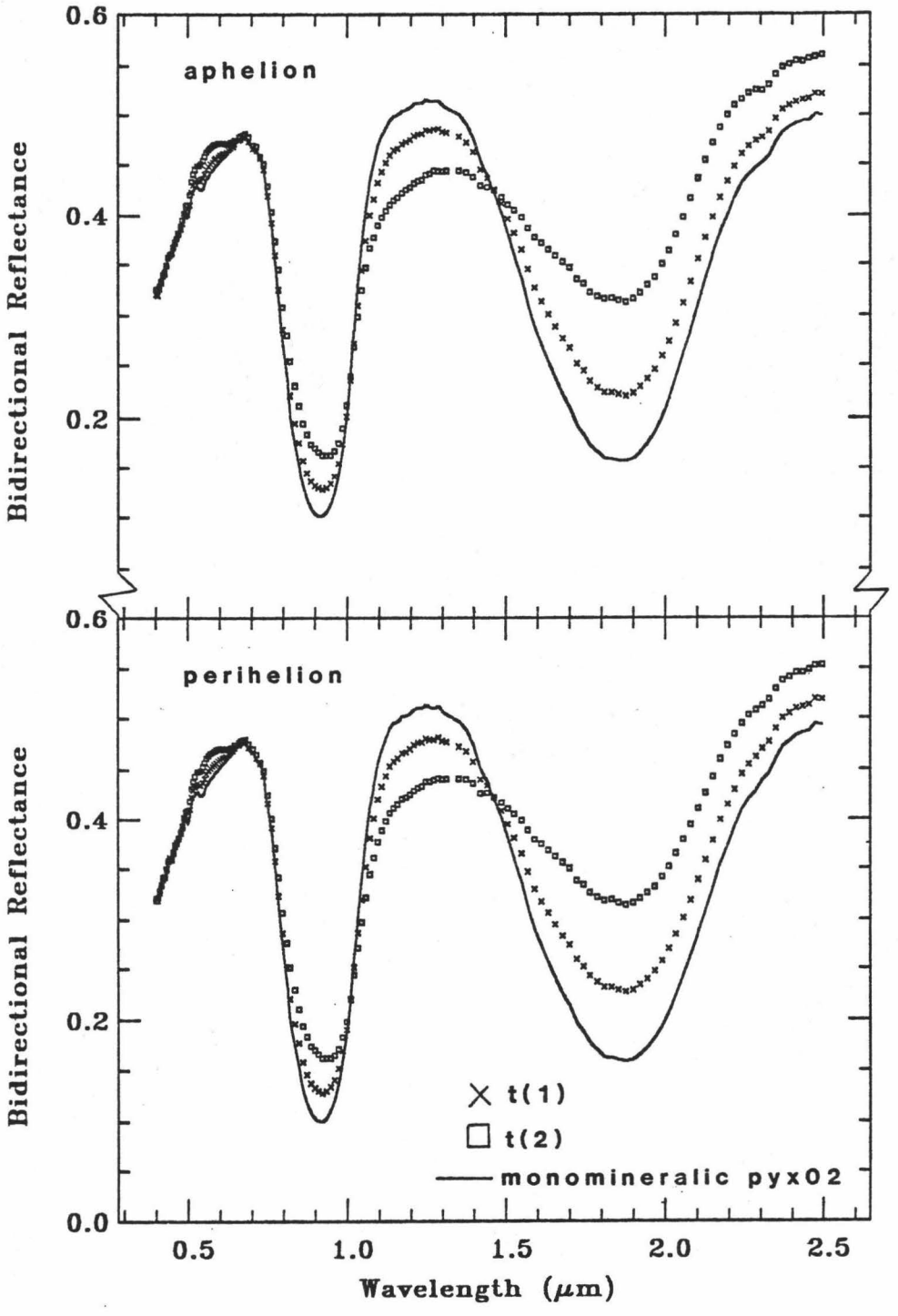

Figure 31. Calculated orthopyroxene surface with olivine spot mixture spectra for two time increments at aphelion and perihelion using the orbital and physical data of 4 Vesta.

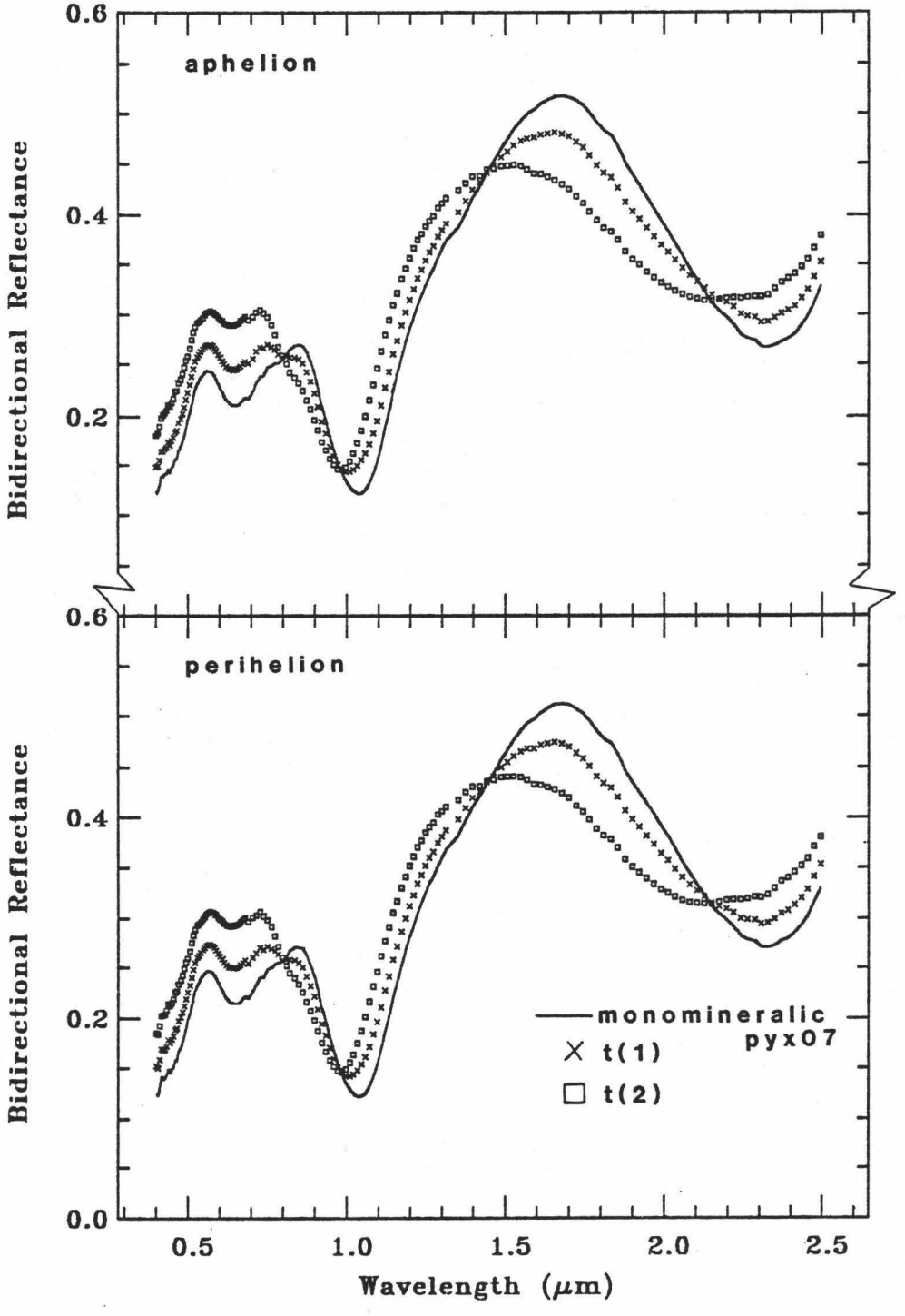

Figure 32. Calculated clinopyroxene surface with orthopyroxene spot mixture spectra for two time increments at aphelion and perihelion using the orbital and physical data of 4 Vesta.

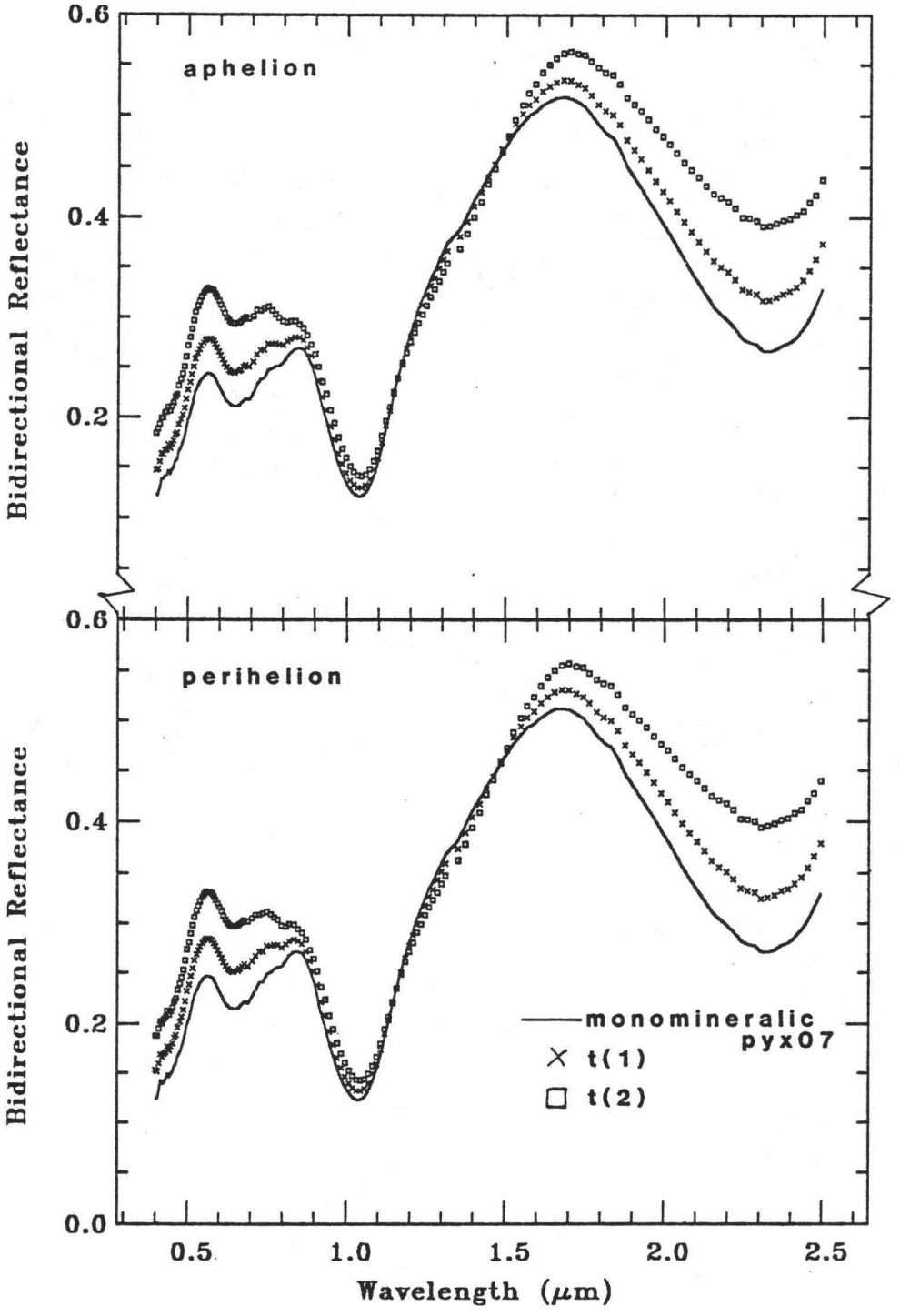

Figure 33. Calculated clinopyroxene surface with olivine spot mixture spectra for two time increments at aphelion and perihelion using the orbital and physical data of 4 Vesta.

The resultant, calculated spectra for 4 Vesta are shown, for various combinations of orthopyroxene, clinopyroxene, and olivine, in Figures 28 to 33. One conclusion drawn from these figures is that for a given time increment there are minor, insignificant, differences between calculated spectra at aphelion and perihelion. However, there are obvious differences between calculated spectra of sequential time increments at both aphelion and perihelion. These spectral differences include shifting of the ABM for both the 1 and 2μm absorptions for most examples as well as, significant changes in the visible region.

Table 7 and 8 are lists of all spectral mixtures at aphelion and perihelion and the ABM of the 1 and 2μm for each time increment for 4 Vesta and 433 Eros, respectively. The values for mixtures with olivine (olv) as the main component (comp a) show that the 2μm ABM remain unchanged, not surprising since olivine has no absorption feature in this region so that any absorption present is due to the other component present. The values for the 1μm ABM do not change with clinopyroxene (cpx) as the "spot", but shift to shorter wavelengths between time increments with the presence of orthopyroxene (opx). If the pyroxene is the major component and olivine is the minor component, again the 2μm ABM is uneffected. However, in this case the 1μm ABM remain relatively uneffected. A spectral mixture with clinopyroxene as the major component and orthopyroxene as the "spot" results in both the 1 and 2μm ABM shifting to shorter wavelengths between successive time increments while a mixture with amounts of the two components reversed results in a shifting of the 1μm ABM to longer wavelengths and the 2μm ABM remaining uneffected.

A similar analysis was performed using the orbital and physical parameters of 433 Eros. The resultant calculated spectra are shown in

Table 7. 1 and 2μm Apparent Band Minimum for 4 Vesta.

comp a	spot	time	position	1 micron	2 micron
olv	cpx	t(1)	aphelion	1.060	2.306
olv	cpx	t(2)	aphelion	1.054	2.306
olv	cpx	t(1)	perihelion	1.060	2.306
olv	cpx	t(2)	perihelion	1.060	2.306
olv	opx	t(1)	aphelion	1.022	1.876
olv	opx	t(2)	aphelion	.998	.1876
olv	opx	t(1)	perihelion	1.022	1.876
olv	opx	t(2)	perihelion	.998	1.876
cpx	opx	t(1)	aphelion	.998	2.306
cpx	opx	t(2)	aphelion	.986	2.150
cpx	opx	t(1)	perihelion	.998	2.306
cpx	opx	t(2)	perihelion	.986	2.150
cpx	olv	t(1)	aphelion	1.047	2.306
cpx	olv	t(2)	aphelion	1.047	2.306
cpx	olv	t(1)	perihelion	1.047	2.306
cpx	olv	t(2)	perihelion	1.047	2.306
opx	cpx	t(1)	aphelion	.924	1.876
opx	cpx	t(2)	aphelion	.936	1.899
opx	cpx	t(1)	perihelion	.924	1.899
opx	cpx	t(2)	perihelion	.936	1.899
opx	olv	t(1)	aphelion	.924	1.876
opx	olv	t(2)	aphelion	.936	1.876
opx	olv	t(1)	perihelion	.924	1.876
opx	olv	t(2)	perihelion	.924	1.876

Table 8. 1 and 2μm Apparent Band Minima for 433 Eros.

comp a	spot	time	position	1 micron	2 micron
olv	cpx	t(1)	aphelion	1.060	2.306
olv	cpx	t(3)	aphelion	1.060	2.306
olv	cpx	t(1)	perihelion	1.060	2.286
olv	cpx	t(3)	perihelion	1.060	2.286
olv	opx	t(1)	aphelion	1.034	1.876
olv	opx	t(3)	aphelion	.998	1.876
olv	opx	t(1)	perihelion	1.034	1.899
olv	opx	t(3)	perihelion	.998	1.899
cpx	opx	t(1)	aphelion	1.011	2.306
cpx	opx	t(3)	aphelion	.986	2.150
cpx	opx	t(1)	perihelion	1.011	2.286
cpx	opx	t(3)	perihelion	.992	2.150
cpx	olv	t(1)	aphelion	1.040	2.306
cpx	olv	t(3)	aphelion	1.047	2.306
cpx	olv	t(1)	perihelion	1.034	2.328
cpx	olv	t(3)	perihelion	1.047	2.286
opx	cpx	t(1)	aphelion	.924	1.899
opx	cpx	t(3)	aphelion	.936	1.899
opx	cpx	t(1)	perihelion	.924	1.899
opx	cpx	t(3)	perihelion	.948	1.945
opx	olv	t(1)	aphelion	.924	1.899
opx	olv	t(3)	aphelion	.924	1.876
opx	olv	t(1)	perihelion	.924	1.899
opx	olv	t(3)	perihelion	.948	1.899

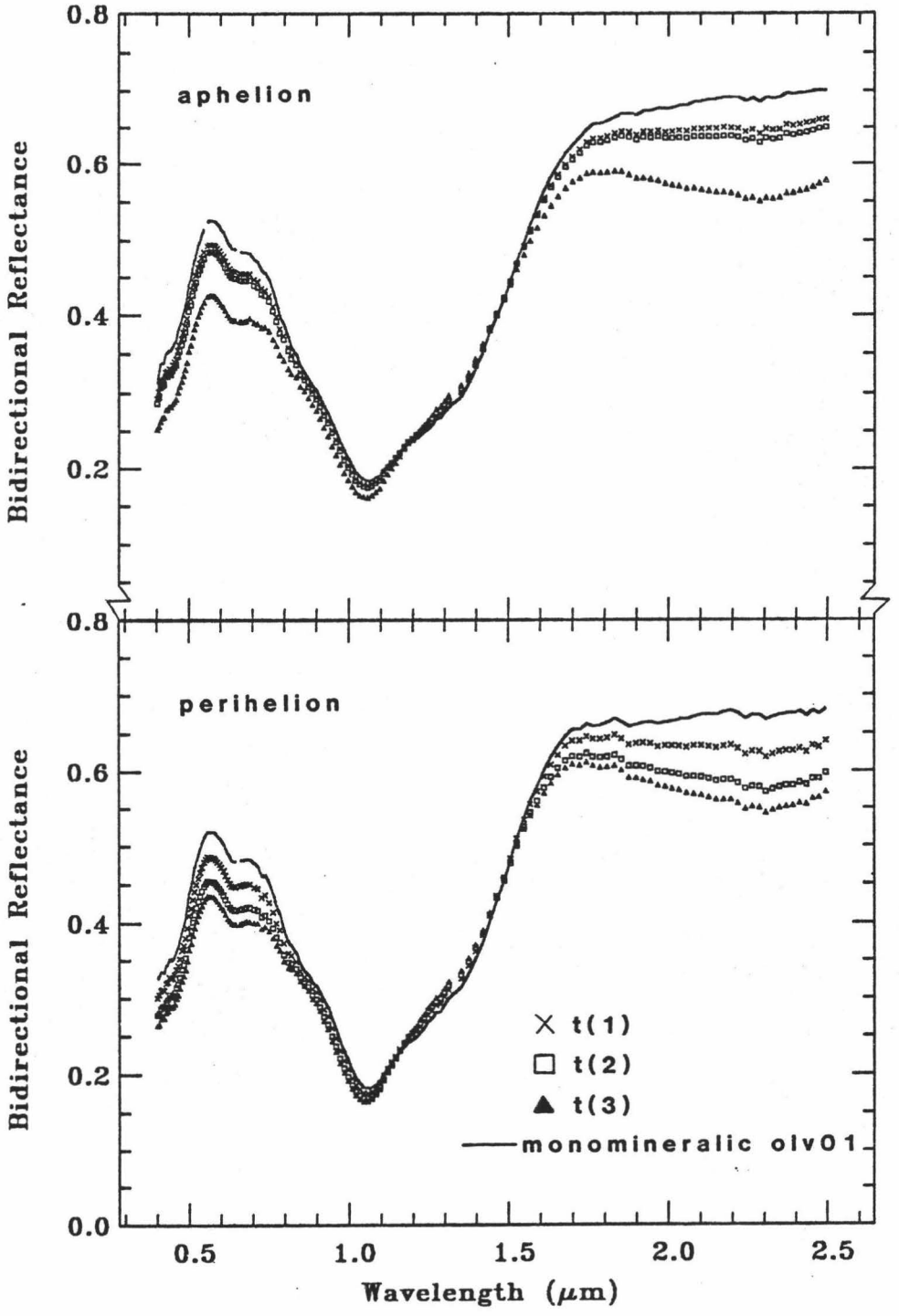

Figure 34. Calculated olivine surface with clinopyroxene spot mixture spectra of three time increments at aphelion and perihelion using the orbital and physical parameters of 433 Eros.

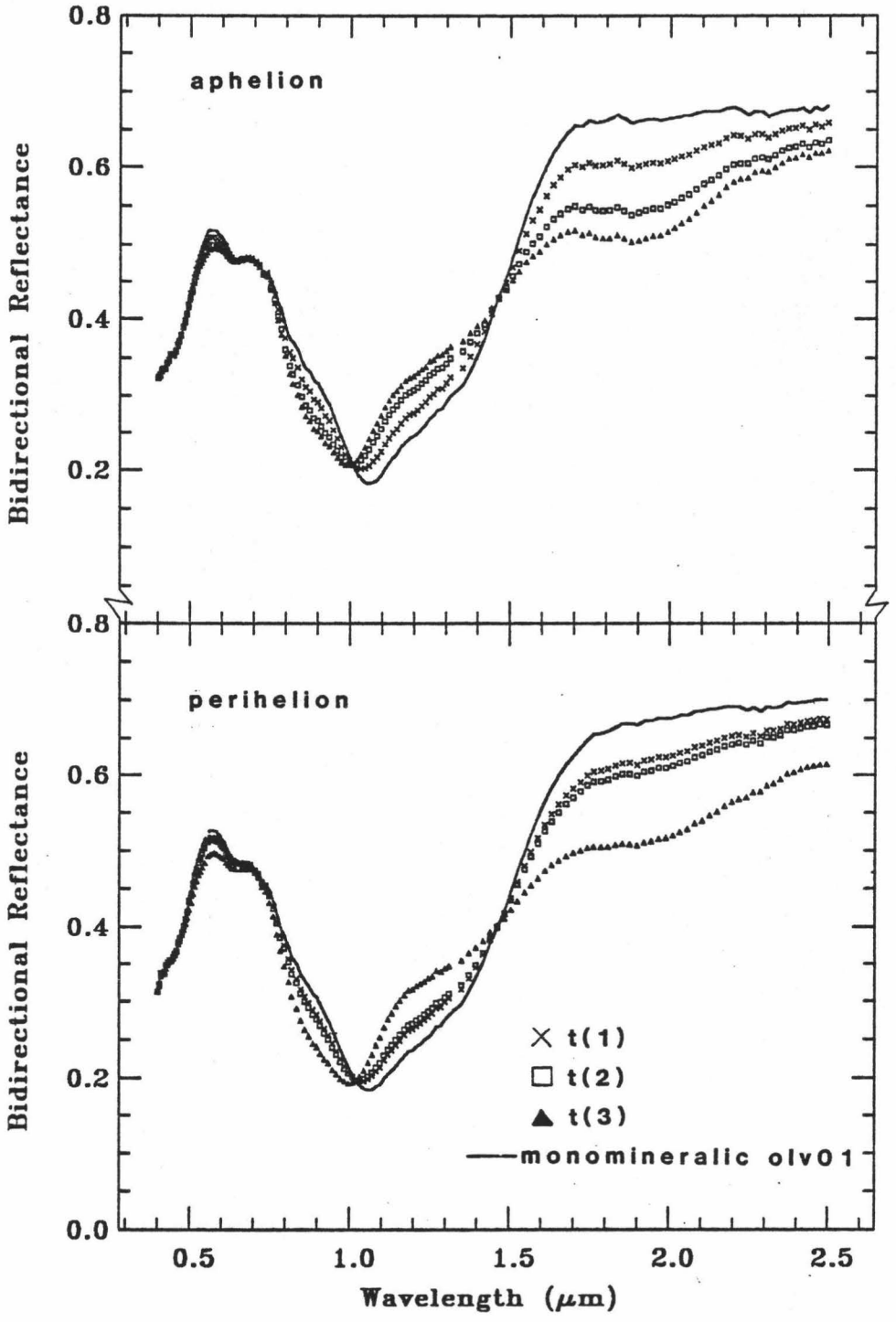

Figure 35. Calculated olivine surface with orthopyroxene spot mixture spectra of three time increments at aphelion and perihelion using the orbital and physical parameters of 433 Eros.

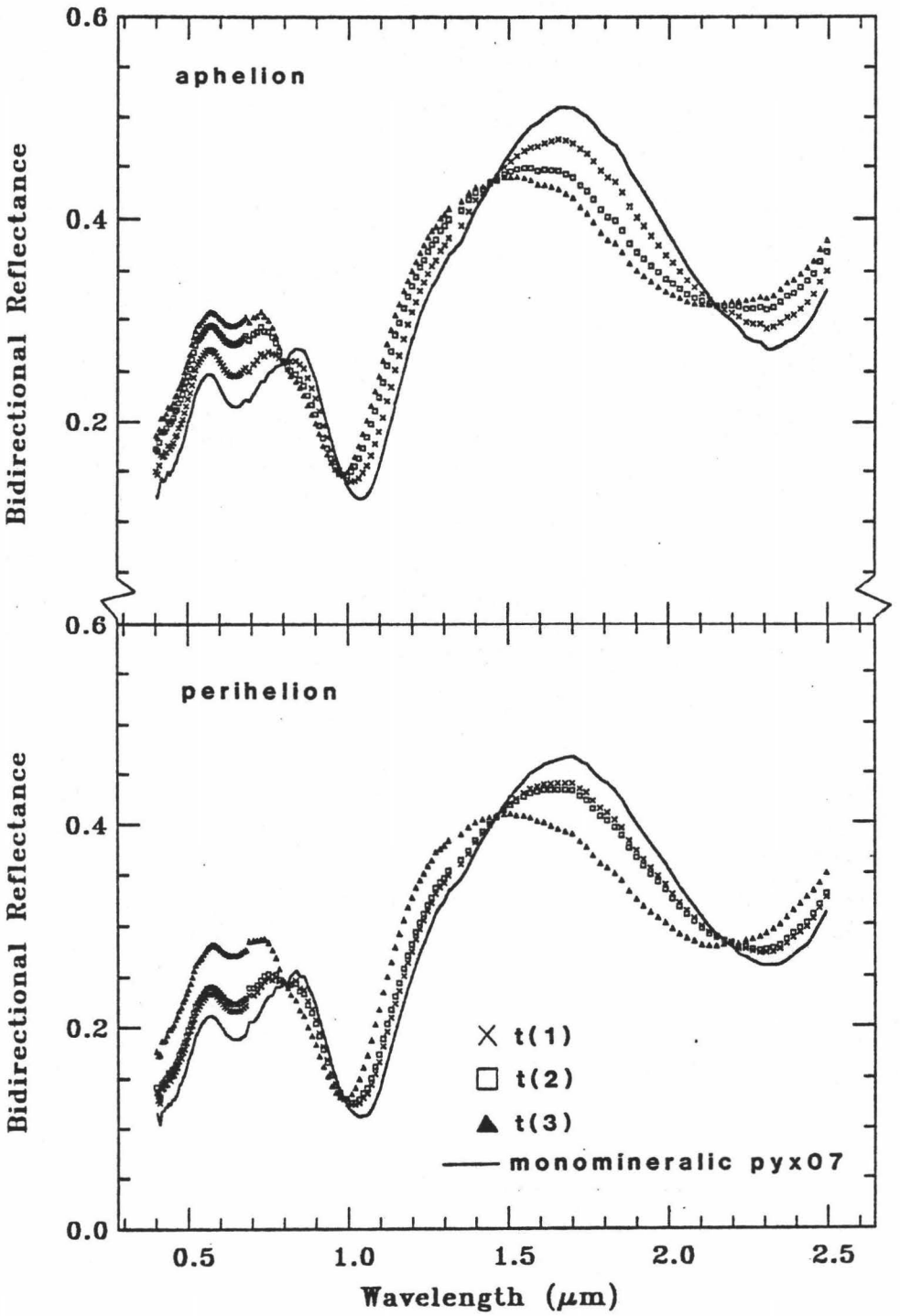

Figure 36. Calculated clinopyroxene surface with orthopyroxene spot mixture spectra of three time increments at aphelion and perihelion using the orbital and physical parameters of 433 Eros.

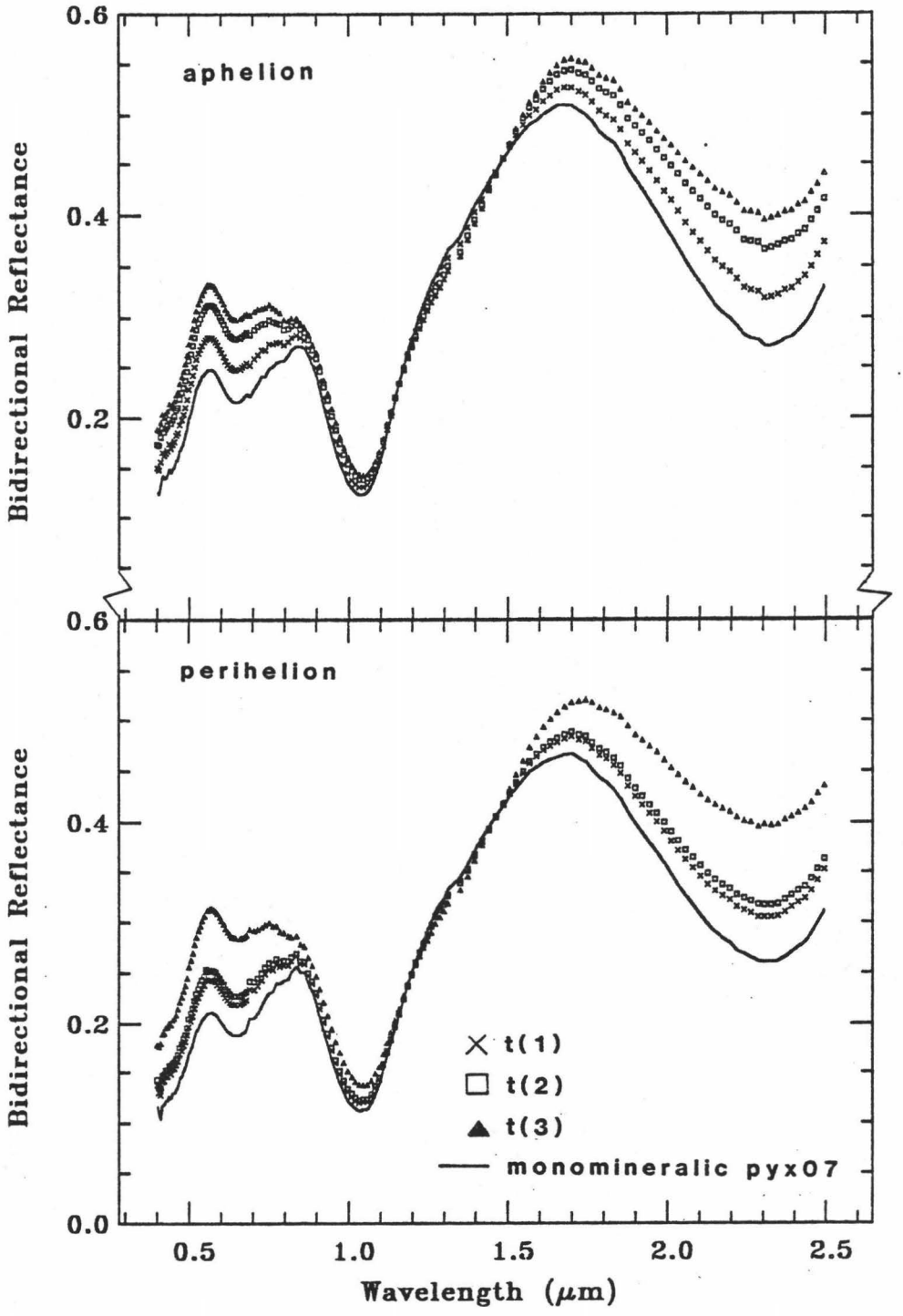

Figure 37. Calculated clinopyroxene surface with olivine spot mixture spectra of three time increments at aphelion and perihelion using the orbital and physical parameters of 433 Eros.

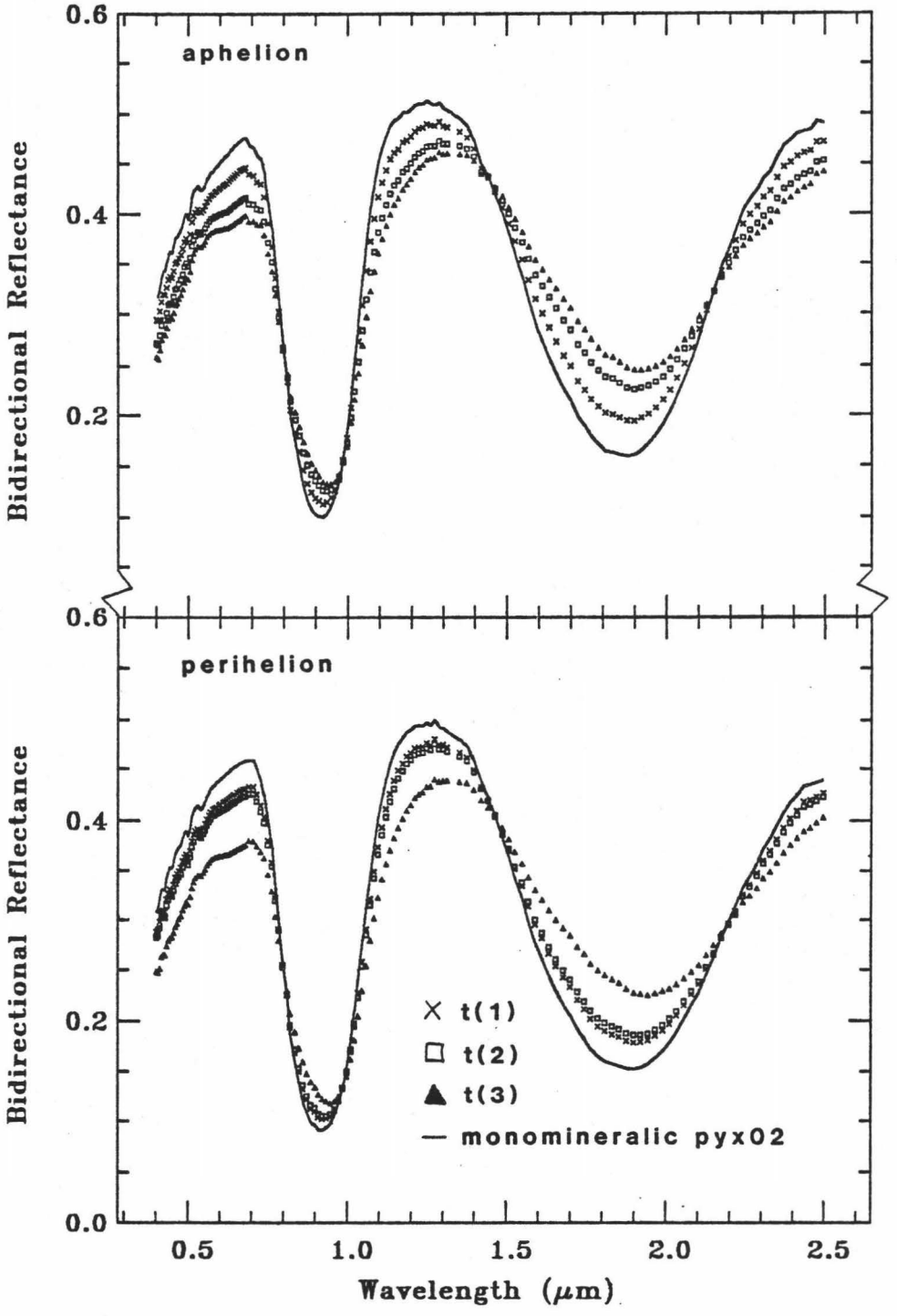

Figure 38. Calculated orthopyroxene surface with clinopyroxene spot mixture spectra of three time increments at aphelion and perihelion using the orbital and physical parameters of 433 Eros.

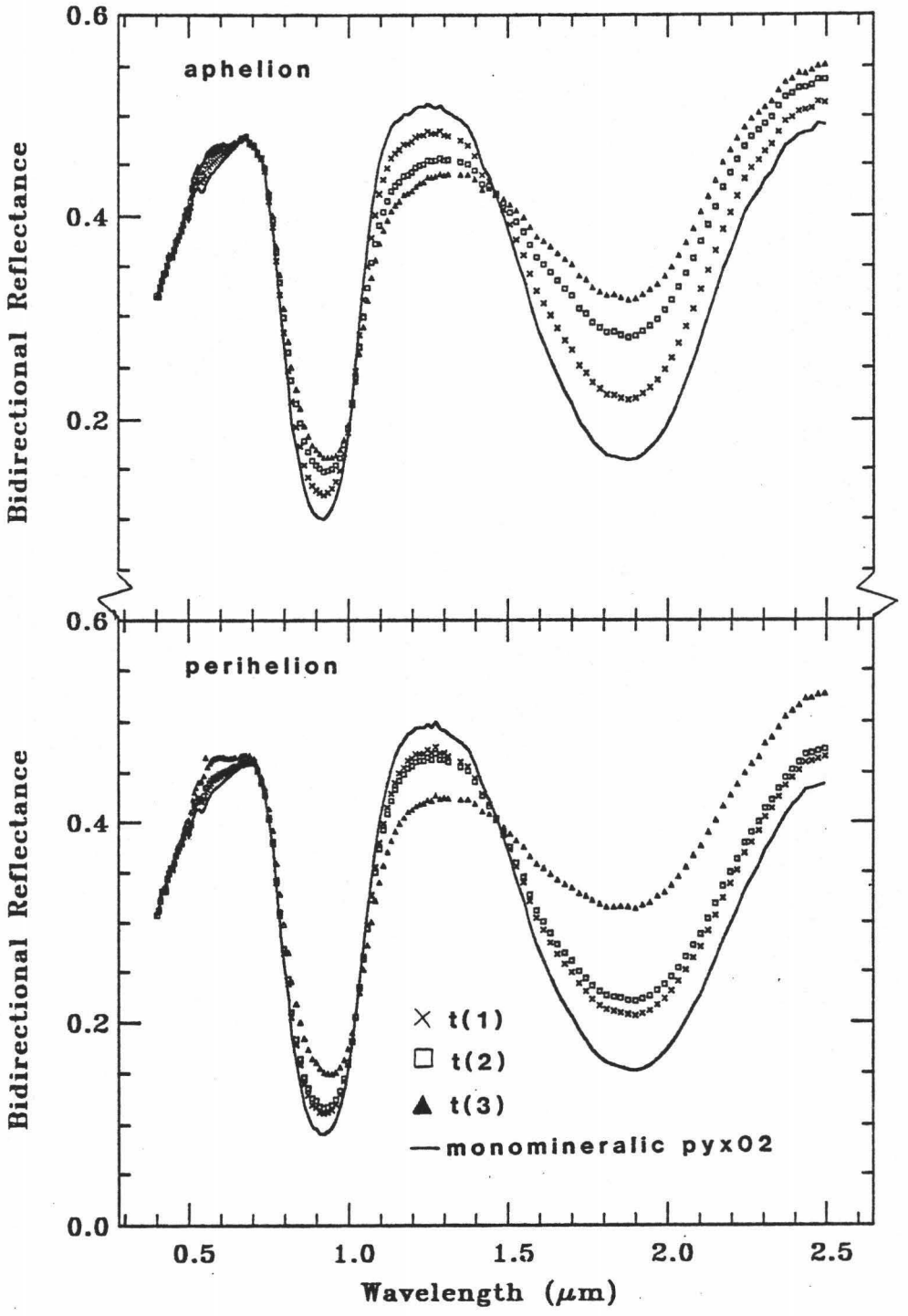

Figure 39. Calculated orthopyroxene surface with olivine spot mixture spectra of three time increments at aphelion and perihelion using the orbital and physical parameters of 433 Eros.

Figures 34 to 39. These figures illustrate that there are spectral differences between successive time intervals and orbital extremes. Both the 1 and 2μm ABM appear to shift and again the visible region is effected.

Referring to Table 8, the values of mixtures with olivine as the main component and clinopyroxene as the "spot" show the 1μm ABM is uneffected by orbital position or where the "spot" is located on the surface but the 2μm ABM shifts to shorter wavelengths at perihelion. If orthopyroxene is present as a "spot" on an olivine surface, the 1μm ABM is a function of where the spot is located on the surface at both orbital extremes while the 2μm ABM is dependent on orbital position but independent of surface location for a given orbital position. These same trends are true if orthopyroxene and olivine are reversed as components. On a surface composed of clinopyroxene with an olivine "spot", the 1μm ABM is dependent on surface location while the 2μm ABM is independent of surface location and dependent on orbital position. On surfaces composed of pyroxenes, the 1- and 2μm ABM are a function of both location of the "spot" on the surface and orbital position.

Using this more complex model, it is difficult to determine if changes in ABM are due solely to temperature effects (a mixture of two minerals at various temperatures) or areal effects (a mixture of two minerals at the same temperature, in varying amounts). However, seperation of these two processes is possible. Using the flux from each temperature interval (Table 5) and the relative contributions from each component listed in Table 6, the total contributions from each component can be calculated and is listed in the last two columns of Table 6. Thus, for a 4 Vesta-like surface the total contribution of each component at t(1) and t(2) are essentially equal at aphelion and

perihelion. This is also true for a 433 Eros-like surface at t(1) and t(3). Comparision of the calculated spectra at aphelion and perihelion for each time increment will illustrate differences due solely to temperature. The comparisons are shown in Figures 40 to 45 for 4 Vesta and 46 to 51 for 433 Eros. Obviously illustrated is the conclusion that spectral differences between successive time increments on a 4 Vesta-like surface are due to the areal increase of the "spot". However, minor temperature effects are seen for mixtures which have orthopyroxene as the main component. These differences are mainly related to broadening of the 1μm absorption band. A 433 Eros-like surface exhibits more pronounced temperature effects exemplified by band broadening, ABM shifting, and changes in overall reflectance thoughout most of the spectral range for many samples.

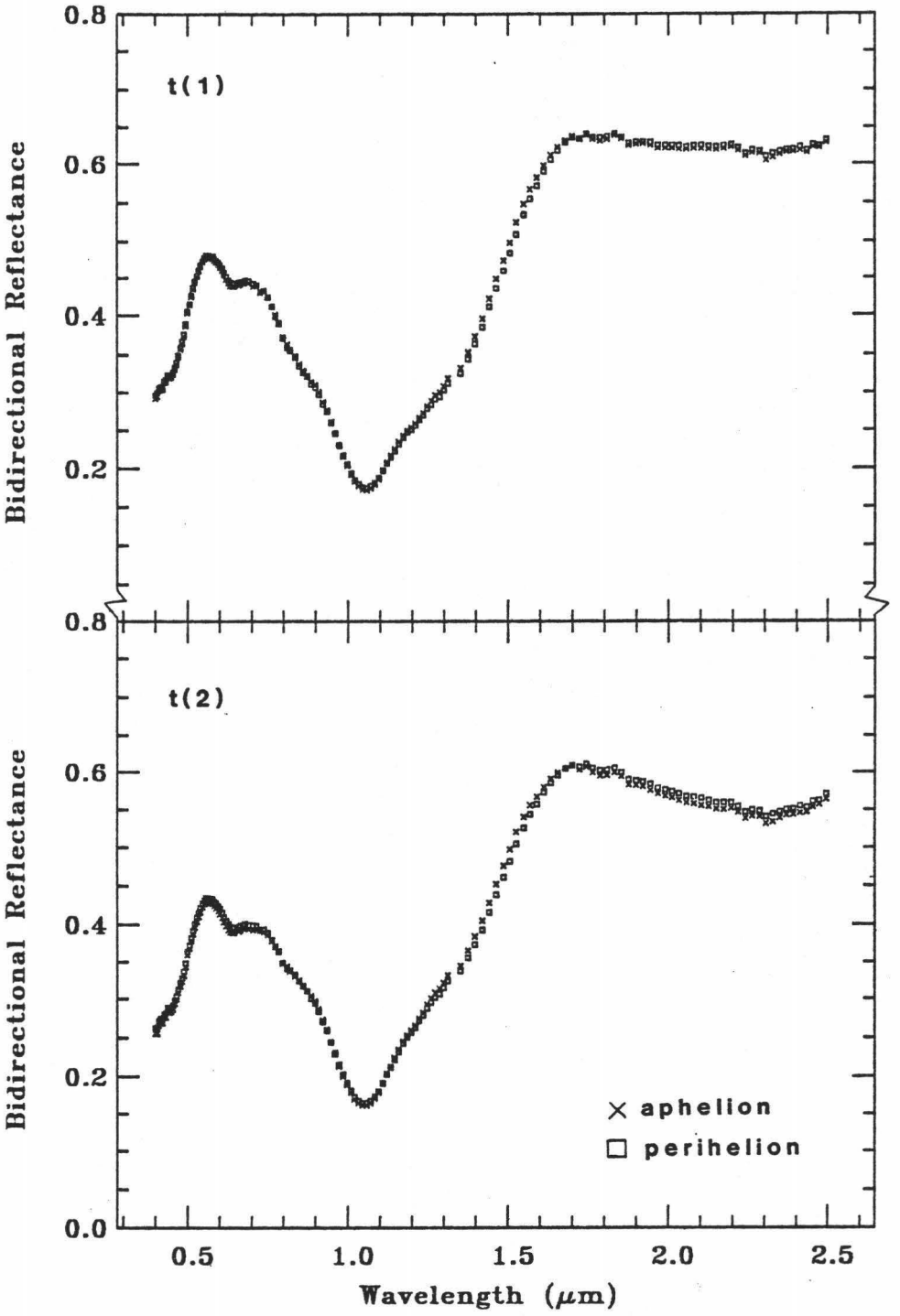

Figure 40. Spectra of the same time increments at the orbital extremes are compared for a calculated olivine surface with clinopyroxene spot using the orbital and physical parameters of 4 Vesta.

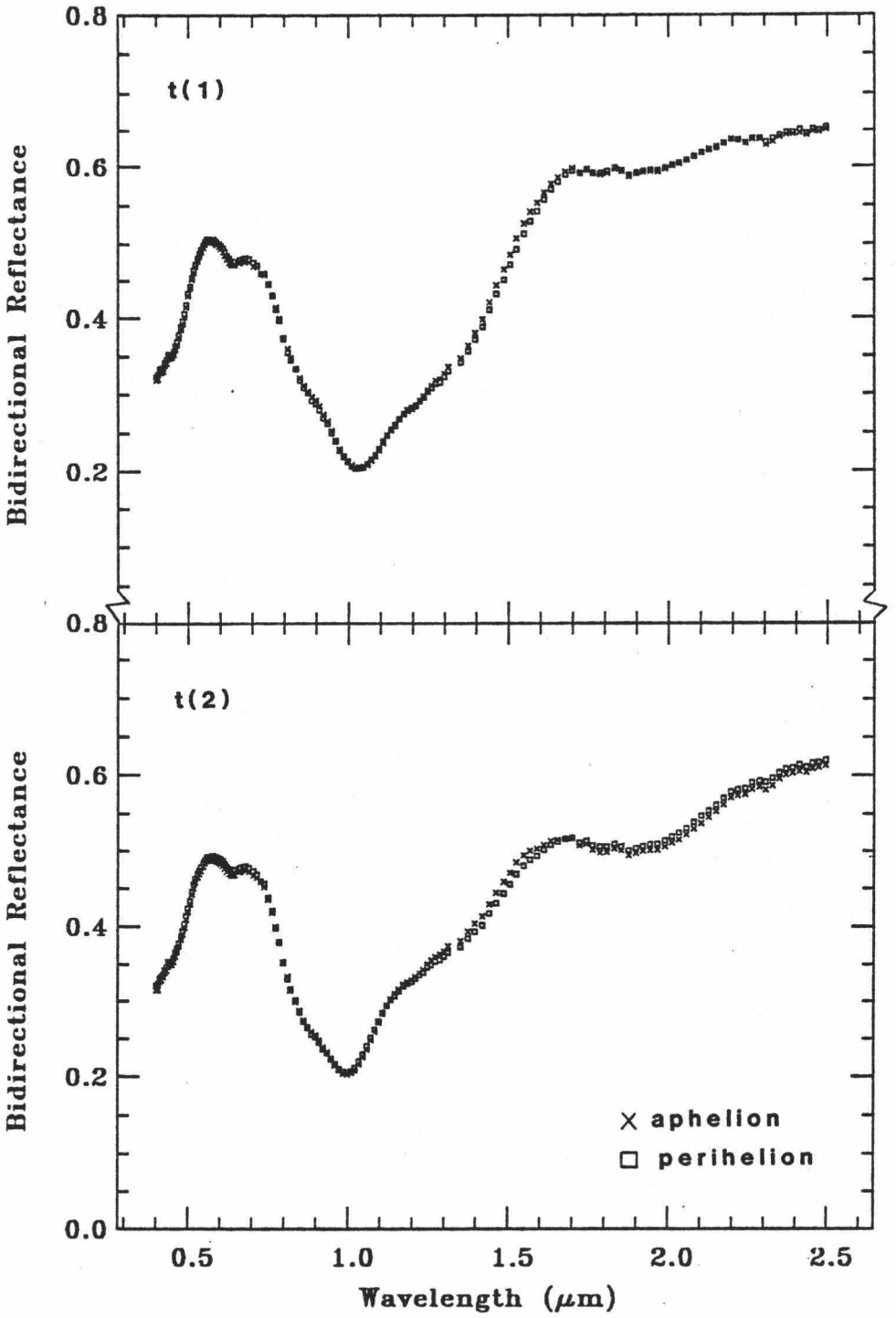

Figure 41. Spectra of the same time increments at the orbital extremes are compared for a calculated olivine surface with orthopyroxene spot using the orbital and physical parameters of 4 Vesta.

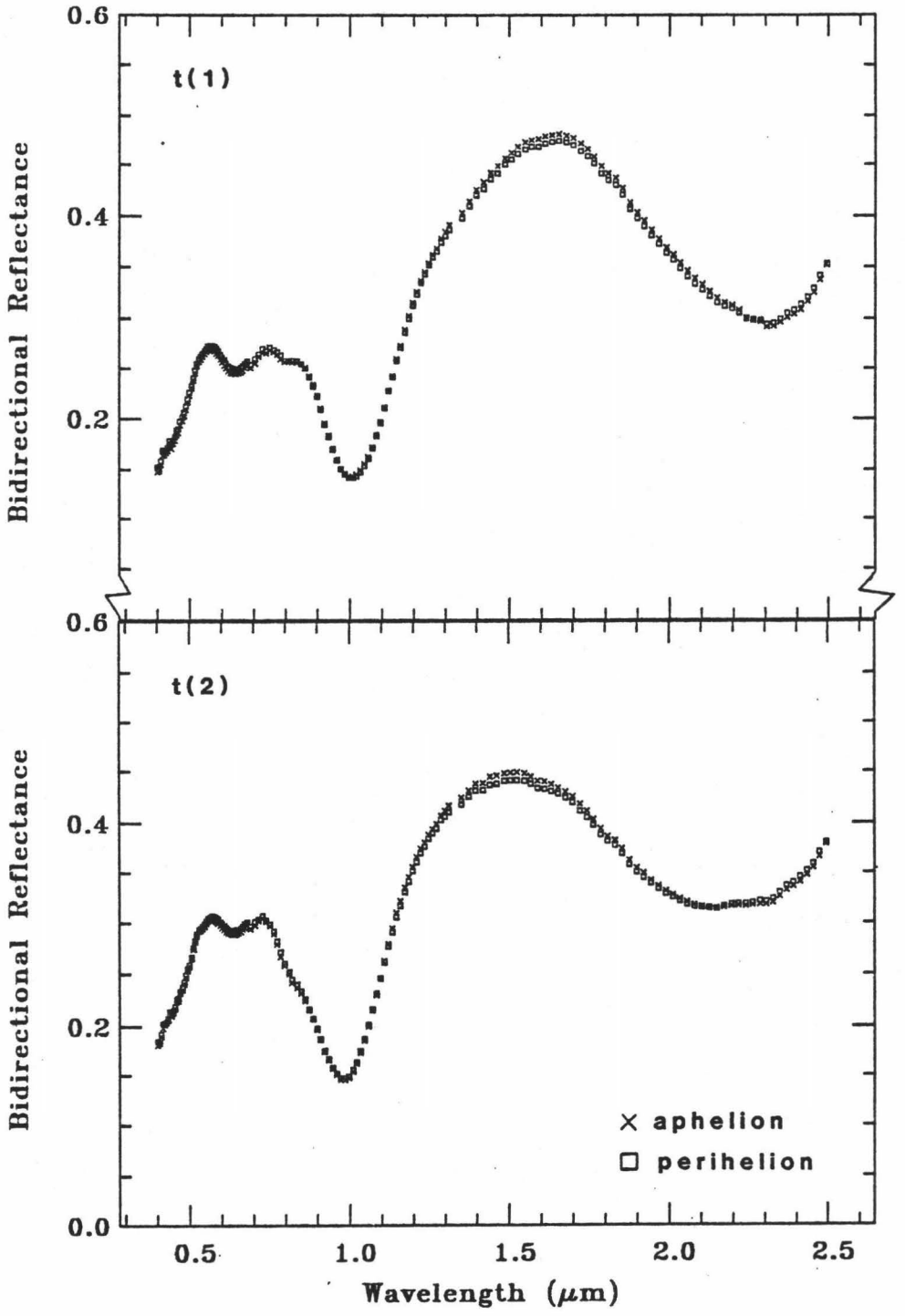

Figure 42. Spectra of the same time increments at the orbital extremes are compared for a caclulated clinopyroxene surface with orthopyroxene spot using the orbital and physical parameters of 4 Vesta.

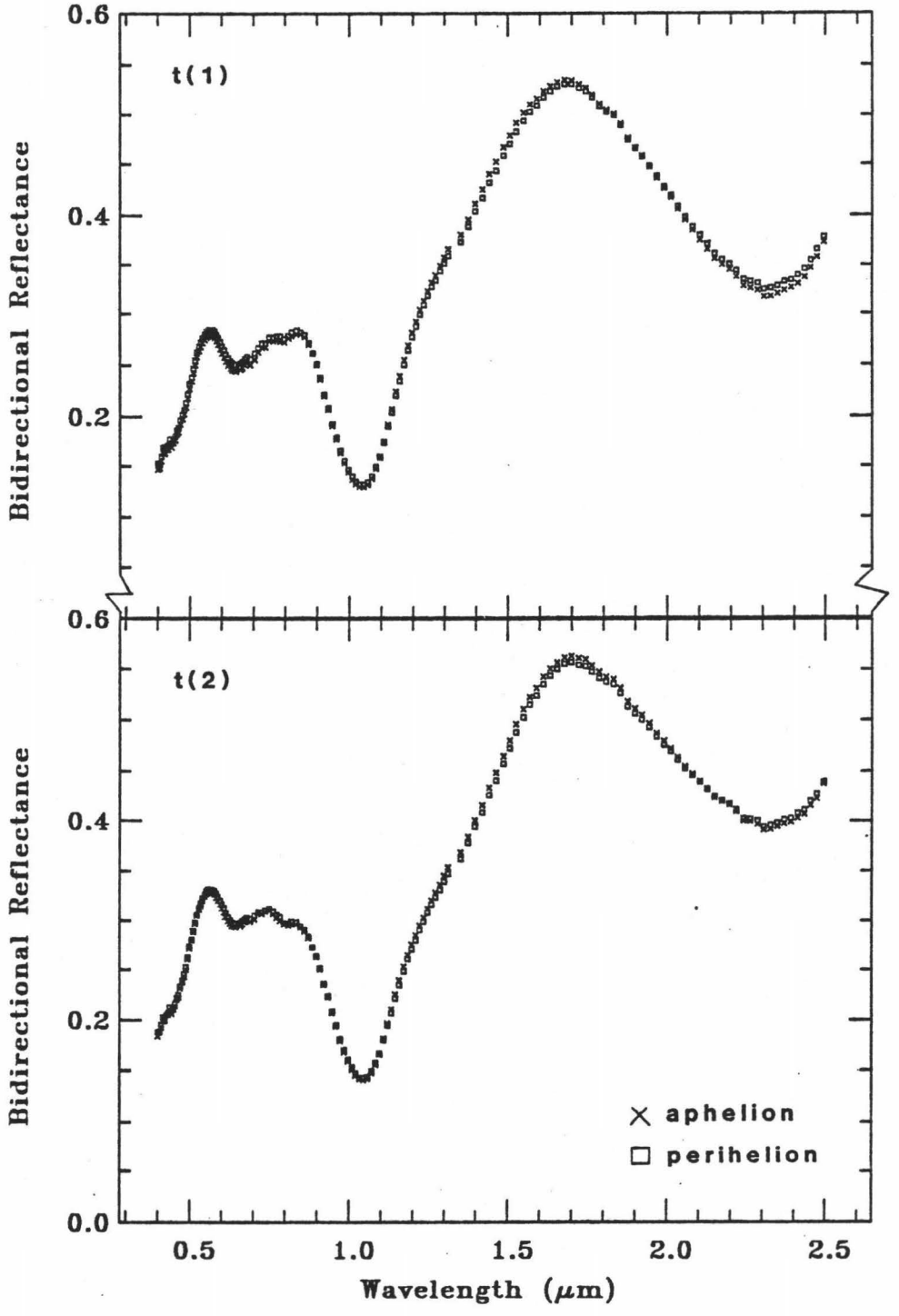

Figure 43. Spectra of the same time increments at the orbital extremes are compared for a calculated clinopyroxene surface with olivine spot using the orbital and physical parameters of 4 Vesta.

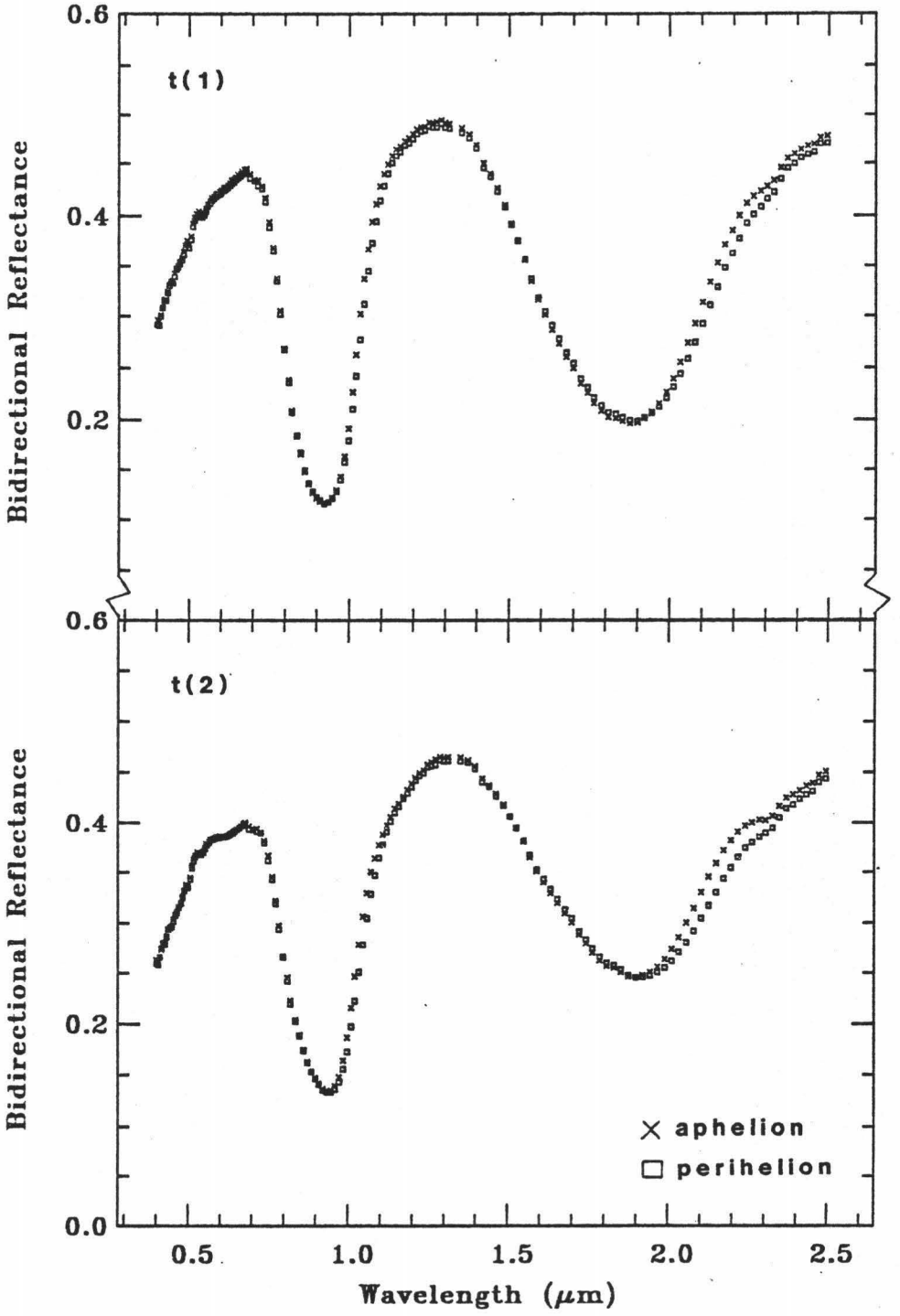

Figure 44. Spectra of the same time increments at the orbital extremes are compared for a calculated orthopyroxene surface with clinopyroxene spot using the orbital and physical parameters of 4 Vesta.

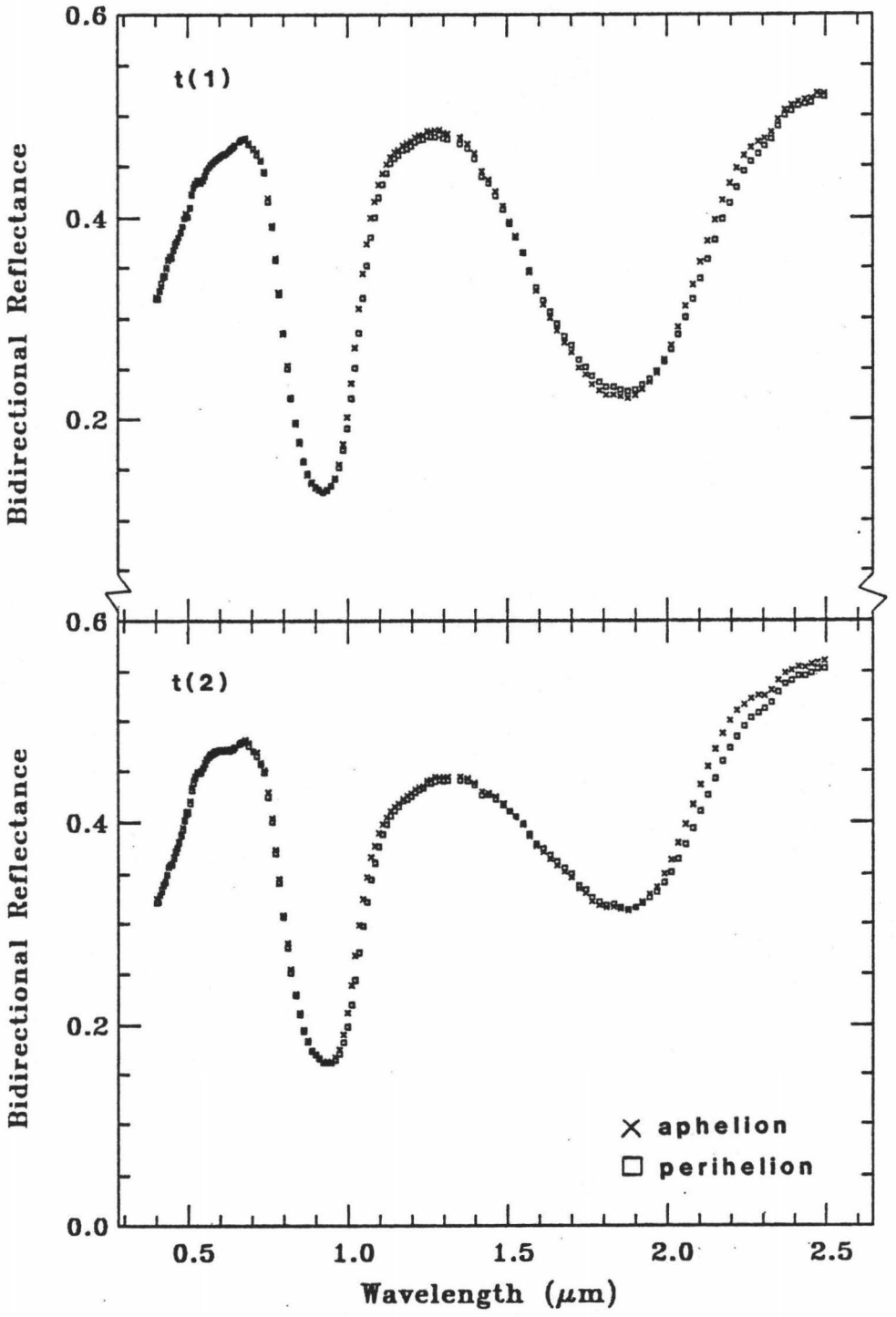

Figure 45. Spectra of the same time increments at the orbital extremes are compared for a calculated orthopyroxene surface with olivine spot using the orbital and physical parameters of 4 Vesta.

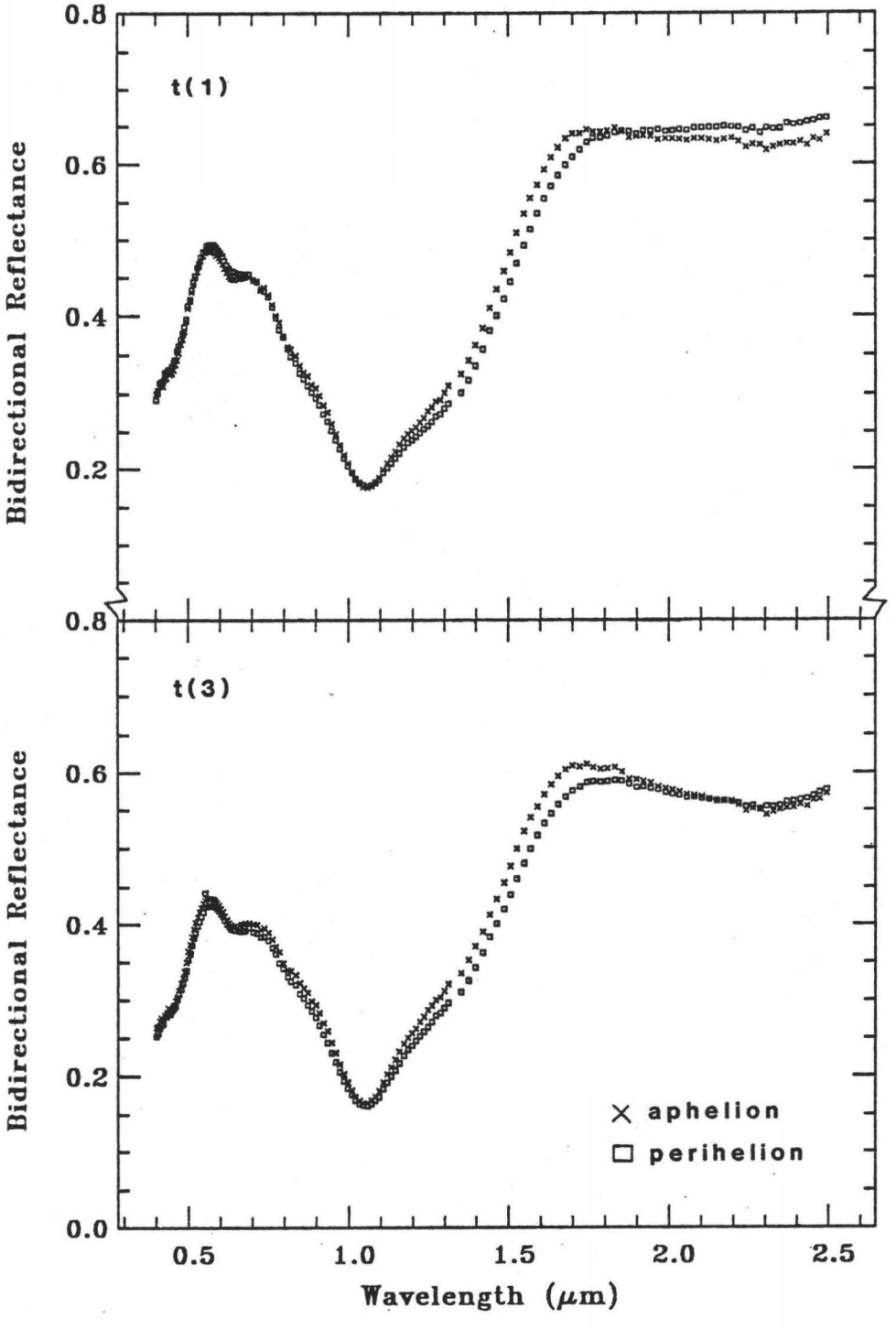

Figure 46. Spectra of the same time increments at the two orbital extremes are compared for a calculated olivine surface with clinopyroxene spot using the orbital and physical parameters of 433 Eros.

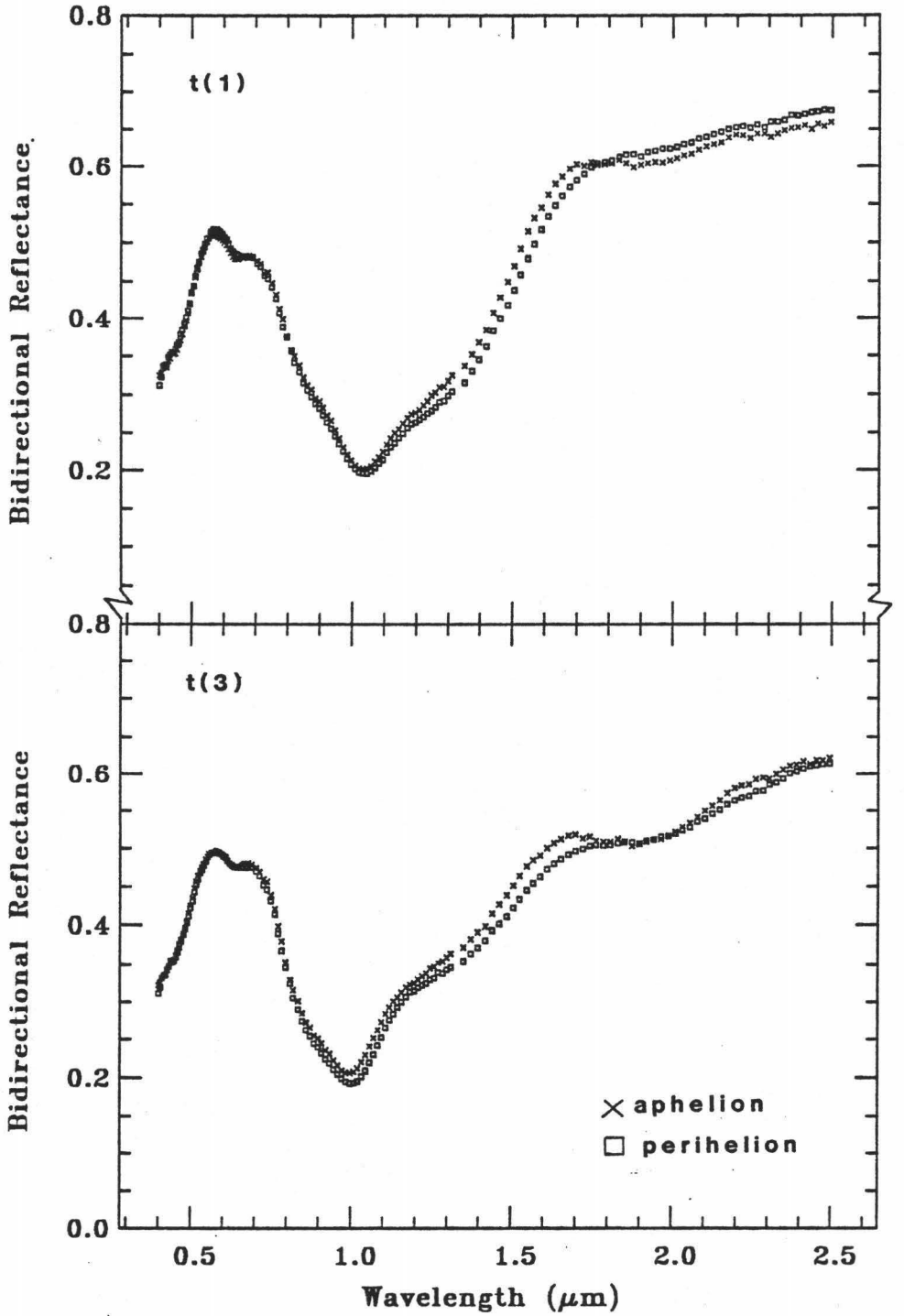

Figure 47. Spectra of the same time increments at the orbital extremes are compared for a calculated olivine surface with orthopyroxene spot using the orbital and physical parameters of 433 Eros.

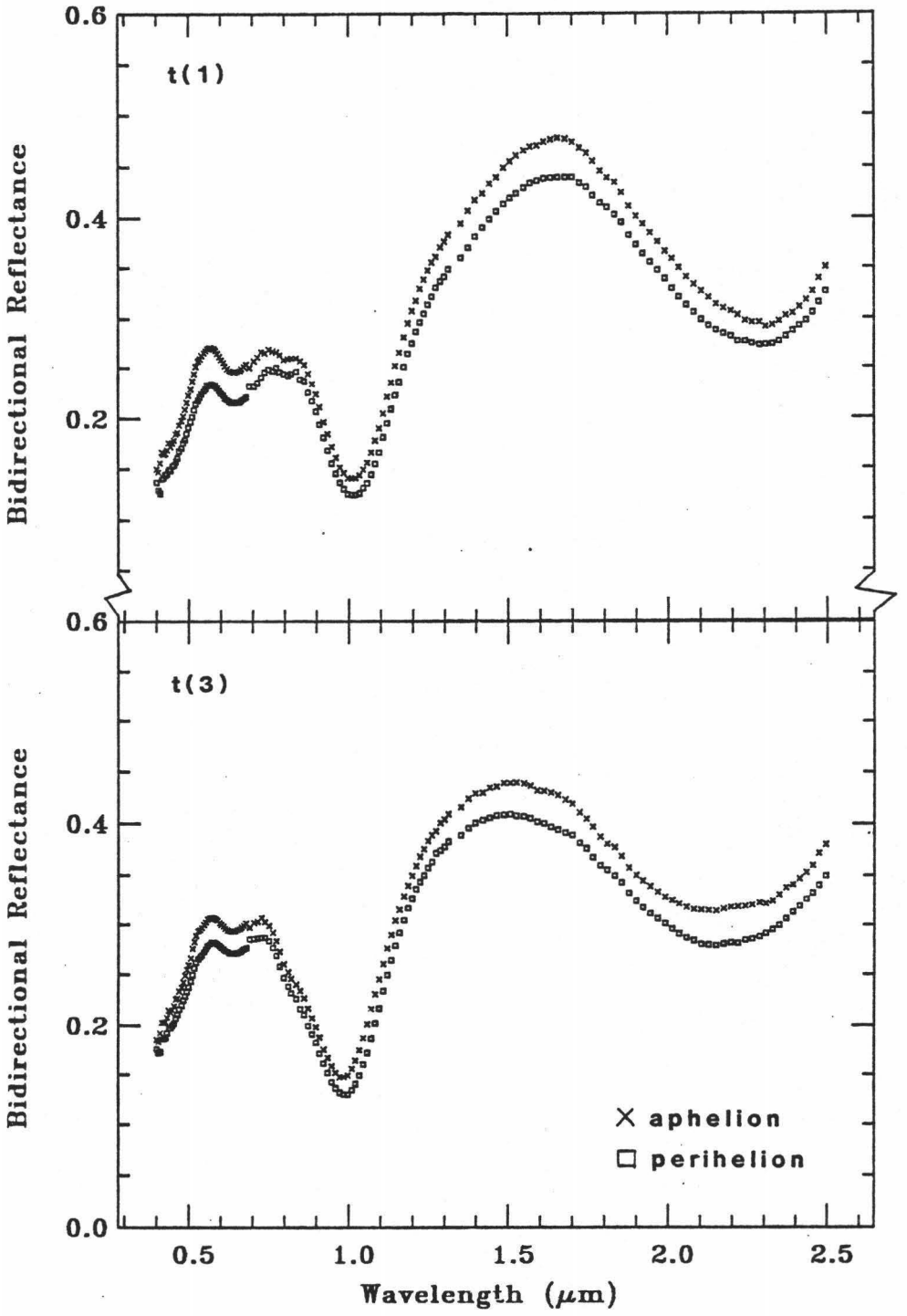

Figure 48. Spectra of the same time increments at the orbital extremes are compared for a calculated clinopyroxene surface with orthopyroxene spot using the orbital and physical parameters of 433 Eros.

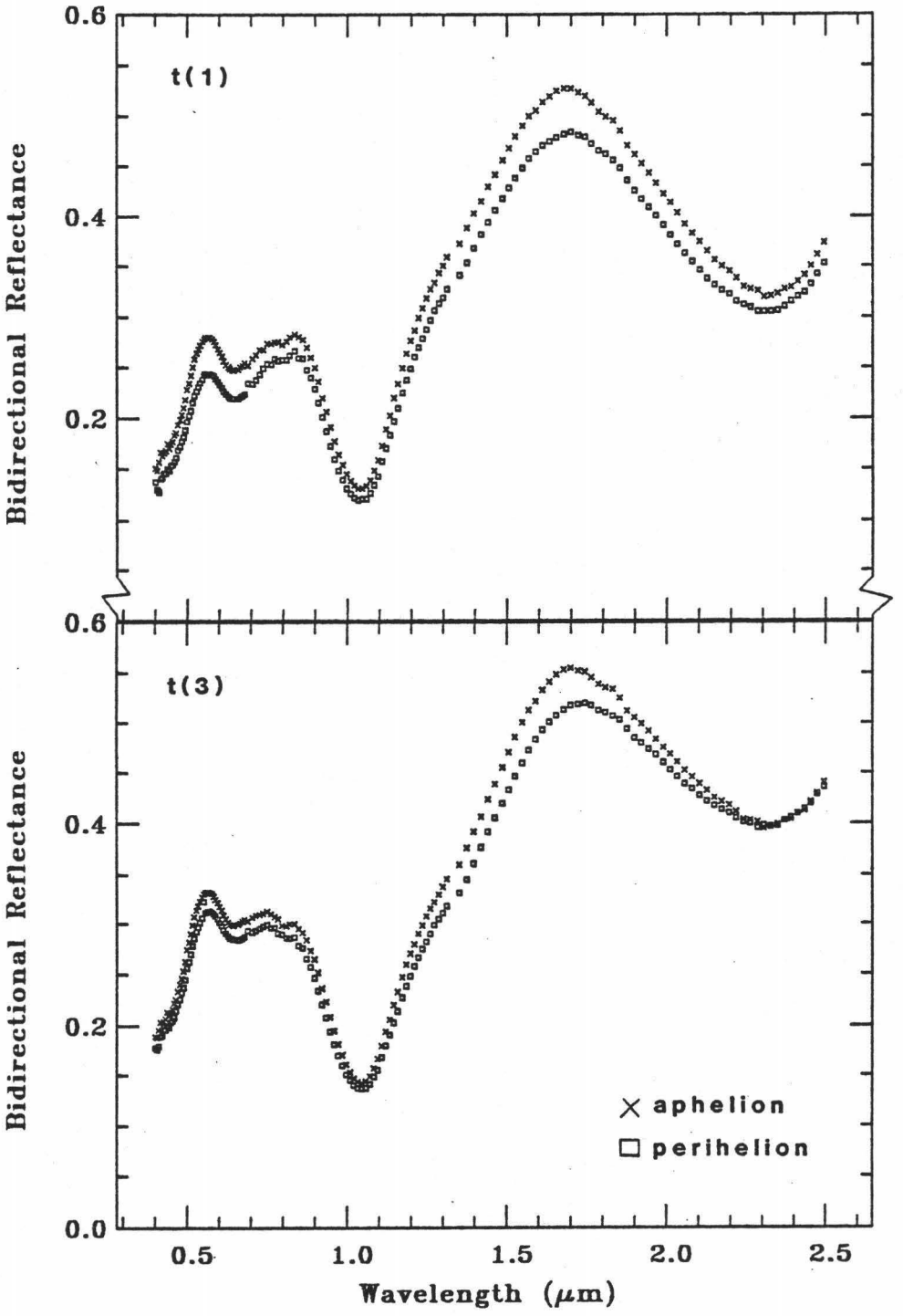

Figure 49. Spectra of the same time increments at the orbital extremes are compared for a calculated clinopyroxene surface with olivine spot using the orbital and physical parameters of 433 Eros.

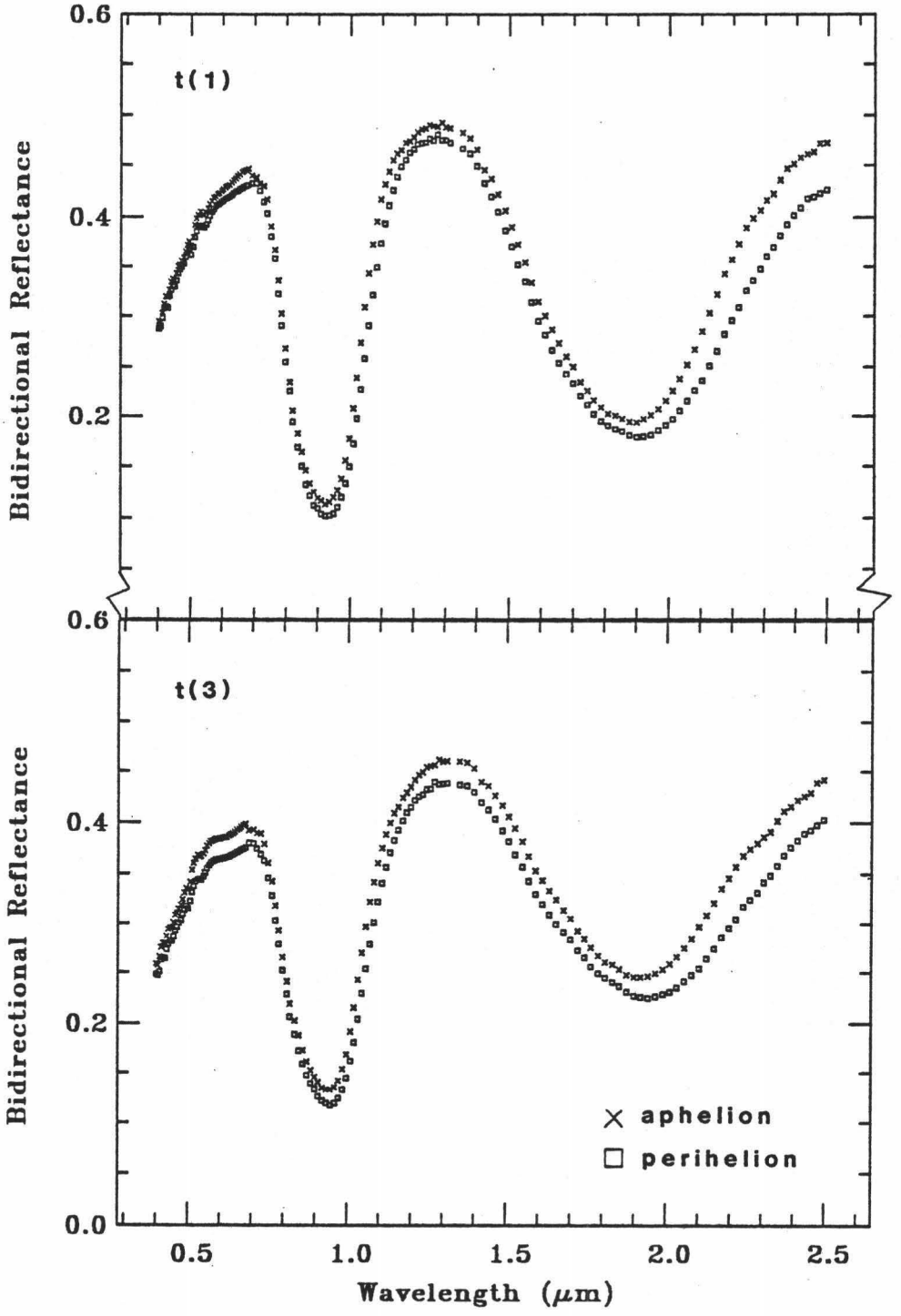

Figure 50. Spectra of the same time increments at the orbital extremes are compared for a calculated orthopyroxene surface with clinopyroxene spot using the orbital and physical parameters of 433 Eros.

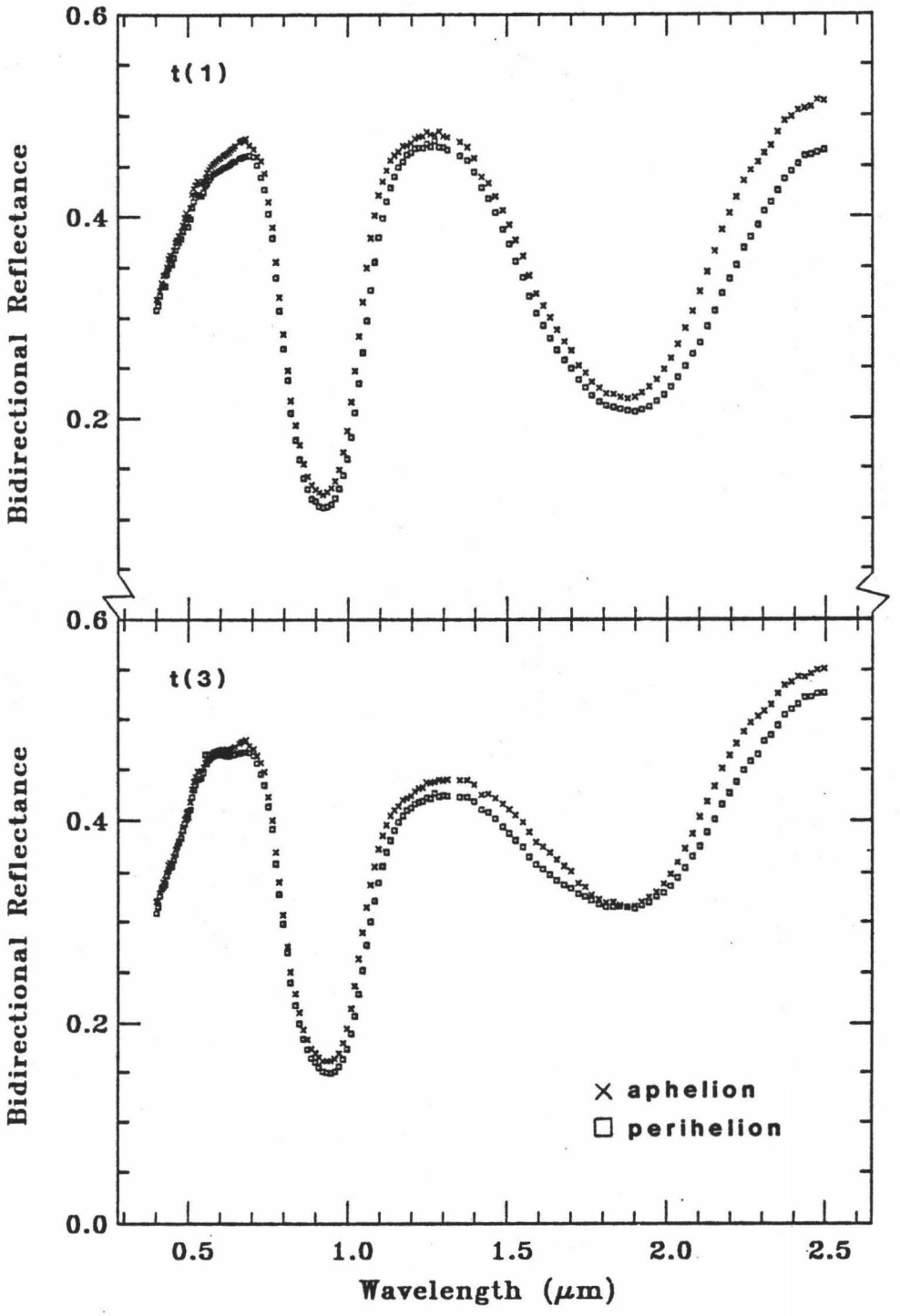

Figure 51. Spectra of the same time increments at the orbital extremes are compared for a calculated orthopyroxene surface with olivine spot using the orbital and physical parameters of 433 Eros.

REFERENCES

Adams, J.B. (1974), Visible and Near-Infrared Diffuse Reflectance Spectra of Pyroxenes as Applied to Remote Sensing of Solid Objects in the Solar System., JGR, 79, 4829-4863.

Bender, D.F. (1979), Osculating Orbital Elements of the Asteroids, in Asteroids, T. Gehrels, ed., Univ. Arizona Press, Tuscon, Arizona, 1015-1039.

Brown R.H., Morrison, D., and Telesco, C.M., (1982), Calibration of the Radiometric Asteroid Scale Using Occultation Diameters., Icarus, 52, 188-195.

Morrison, D., (1977), Asteroid sizes and albedos. Icarus, 31, 185-220.

Morrison, D., and Lebofsky, L.A., (1979) Asteroid Radiometry, in Asteroids, T. Gehrels, ed., Univ. Arizona Press, Tuscon, Arizona, 184-205.

Williams, J.G., (1979) Proper Elements and Family Memberships of the Asteroids, in Asteroids, T. Gehrels, ed., Univ. Arizona Press, Tuscon, Arizona, 1040-1063.

CHAPTER VI: SUMMARY

The results in chapter 3 show that characteristic reflectance spectra of mafic minerals are a function of surface temperature. The effects of temperature include broadening of all absorptions with increasing temperature and shifting of the 2μm absorption feature of the pyroxenes. The implication of these changes is that the optical constants, absorption coefficient and/or refractive index are also a function of temperature. Thus, the interpretation of remotely obtained data based on room temperature, laboratory measurements must be made with caution.

Chapter 4 characterizes the shifting of the pyroxenes 2-μm absorption. Spectra of the orthopyroxenes show positive wavelength shifts while the clinopyroxene exhibits negative wavelength shifts as temperature increases. The characterization of the pyroxenes 1μm absorption features by Gaussian analysis yields consistent trends of the individual Gaussian parameters which may be useful in quantitative determination of these minerals in mixtures. However, using the data presented here, the trends of the resolved Gaussians cannot be directly related to expected trends due to physical processes which could potentially result in two absorptions within the region analyzed. Several physical mechanisms are plausible to explain the Gaussian trends of the clinopyroxene but require further analysis using a larger sample population or other experimental techniques. The Gaussian analysis of the olivine does not resolve the mechanism which results in an absorption at ≈.65μm. The analysis of the Fe^{2+} crystal field absorption raises some interesting questions concerning the importance of site symmetry in relation to over all expansion of a crystal site.

In chapter 5 it was shown that in a given solar system orbital parameters are the most important factors in determining surface

temperature, and thus spectral variations on asteroid-like surfaces. Main-belt asteroid bodies are spectrally equivalent at aphelion and perihelion for both mono- and bimineralic surfaces. As such, these types of bodies will not be subject to possible misintrepretation of mineralogy at any point in their orbits. However, earth crossers, and probably main-belt bodies, with higher eccentricity exhibit spectral differences in the position of 2μm band positions for both mono- and bimineralic surfaces at aphelion and perihelion. This could lead to differences in mineralogical interpretation of Fe content of 5-10% simply due to orbital position of the body.

This study assumes that any thermal flux from a planetary surface can be accurately removed. However, in practice this is difficult to achieve and errors in thermal removal could also lead to errors in determined band positions. The thermal modelling of chapter 5 could also be carried out for "hot" planetary surfaces provided the thermal flux could be accurately removed. Also, it is important to consider that the thermal modelling was assuming an integrated disk. If instead of being an earth bound observer, as presented in chapter 5, the detector was located on a spacecraft orbiting the body, the resolution of spectra at many of the temperatures presented in this study would be possible. This could lead to the erroneous conclusion that many minerals of varying composition were present on the surface. An example of this is presented by the spectral data of PYX09 where near the limb the presence of two pyroxenes is easily discernable, whereas near the sub-solar point one may conclude only pigeonite is present even though the mineralogy remains unchanged across the surface.

APPENDIX 1: DERIVATION OF FLUX CONTRIBUTIONS FROM AN ASTEROID-LIKE SURFACE

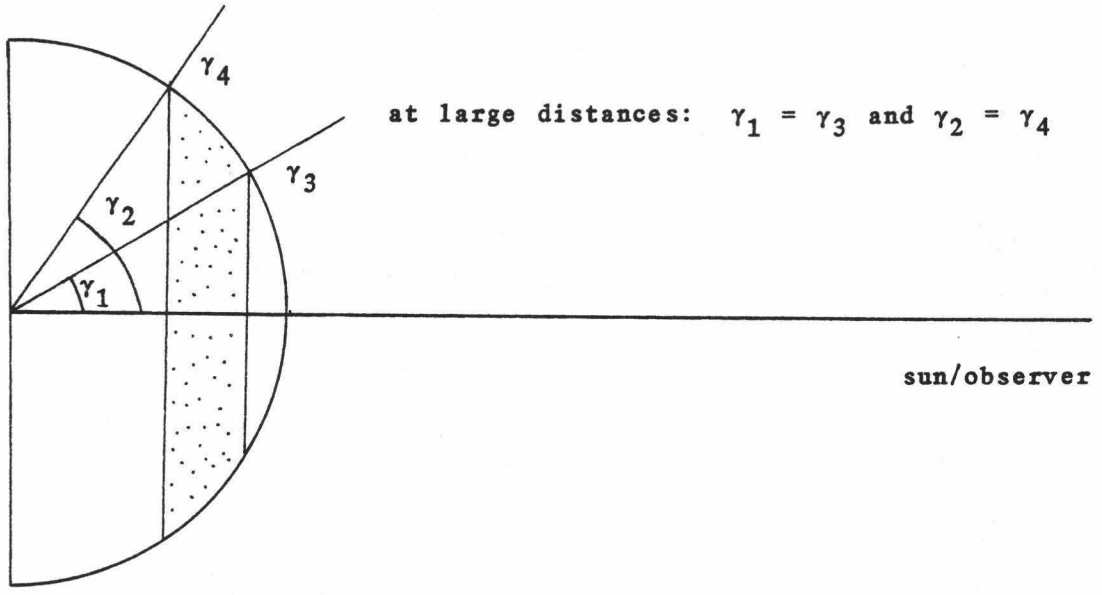

The following derivation refers to the diagram above. Its purpose is to relate the flux contribution from an annulus on a hemisphere to the total flux contribution from the entire hemisphere. The area of an annulus can be expressed as:

$$A = 1 \times w, \qquad \text{(eqn 1)}$$

where A is the area, 1 is the length of the anulus and w is the width of the annulus. If the annulus on the sphere is projected onto an equivalent disk, as seen at the sub-solar/observer point, then the area of the projected ring can be expressed as:

$$dA = 2\pi r\, dr, \qquad \text{(eqn 2)}$$

where

$$r = R \sin\gamma \quad \text{and} \quad dr = R \cos\gamma\, d\gamma, \qquad \text{(eqn 3)}$$

where R is the radius of the sphere, r is the projected radius on the disk, and γ is the angle between the sub-solar/observer point and the annulus. Thus, equation 2 becomes:

$$dA = 2\pi R^2 \sin\gamma\cos\gamma d\gamma. \qquad \text{(eqn 4)}$$

The flux reflected from the ring (F_r), assuming a lambert sphere, is given by:

$$F_r = F_i \cos\gamma dA, \qquad \text{(eqn 5)}$$

where F_i is the incident flux. Subsitituting equation 4 into equation five yields,

$$F_r = F_i \, 2\pi \sin\gamma \cos^2\gamma d\gamma. \qquad \text{(eqn 6)}$$

and F_r can be expressed as:

$$F_r = F_i \, 2\pi R^2 \int_{\gamma_1}^{\gamma_2} \sin\gamma \cos^2\gamma d\gamma. \qquad \text{(eqn 7)}$$

If $\mu = \cos\gamma$, then $d\mu = -\sin\gamma d\gamma$ and equation 7 becomes

$$F_r = -F_i 2\pi R^2 \int_{\mu_1}^{\mu_2} \mu^2 d\mu. \qquad \text{(eqn 8)}$$

After integration, and substituting back for μ, this becomes

$$F_r = -\frac{2}{3} F_i \pi R^2 \left[\cos^3\gamma_2 - \cos^3\gamma_1\right] \qquad \text{(eqn 9)}$$

or alternativly,

$$F_r = \frac{2}{3} F_i \pi R^2 \left[\cos^3\gamma_1 - \cos^3\gamma_2\right]. \qquad \text{(eqn 10)}$$

The total flux reflected from the hemisphere is

$$F_r = \frac{2}{3} F_i \pi R^2 \left[\cos^3 0 - \cos^3\frac{\pi}{2}\right] = \frac{2}{3}\pi R^2, \qquad \text{(eqn 11)}$$

and the contribution of a given annulus is

$$\frac{\frac{2}{3}\pi R^2 F_i \left[\cos^3\gamma_1 - \cos^3\gamma_2\right]}{\frac{2}{3}\pi R^2 F_i} \qquad \text{(eqn 12)}$$

which reduces to

$$\cos^3\gamma_1 - \cos^3\gamma_2.$$